Title
On the Surface of Things: Surface and Interfacial Properties of Hexagonal Boron Nitride, Graphene, Graphite Oxide, and Perfluorophenyl Azides

Author
Marsh, Kristofer Lee

Publication Date
2017

Peer reviewed|Thesis/dissertation

UNIVERSITY OF CALIFORNIA

Los Angeles

On the Surface of Things:
Surface and Interfacial Properties of Hexagonal Boron Nitride, Graphene, Graphite Oxide, and Perfluorophenyl Azides

A dissertation submitted in partial satisfaction of the
requirements for the degree Doctor of Philosophy
in Chemistry

by

Kristofer Lee Marsh

2017

ABSTRACT OF THE DISSERTATION

On the Surface of Things:

Surface and Interfacial Properties of Hexagonal Boron Nitride,

Graphene, Graphite Oxide, and Perfluorophenyl Azides

by

Kristofer Lee Marsh

Doctor of Philosophy in Chemistry

University of California, Los Angeles, 2017

Professor Richard B. Kaner, Chair

Unique to the chemistry of materials is the consideration of both a material's bulk properties as well as that material's surface properties. The alteration of the surface chemistry of a material may change its overall functionality, thereby changing its expected behavior in a given system. The importance of surface chemistry emerges in a broad range of specializations. Areas of study such as energy storage, drug delivery, catalysis, and membrane water purification all take care to consider the surface properties of the compounds and materials involved. Indeed, surface science is an influential aspect of a multitude of research topics.

Centered around the theme of surface and interfacial chemistry, this dissertation examines how modifying and playing with various materials' surface characteristics impacts their behavior within their respective applications. Specifically, the materials examined herein include hexagonal boron nitride, graphene, graphite oxide, and perfluorophenyl azides.

Chapter 1 gives a brief introduction to the importance of surface science in materials chemistry. Chapter 2 discusses how the co-solvent approach to exfoliating and suspending hexagonal boron nitride nanosheets is a simpler, safer alternative to conventional methods of suspending the particles. Chapter 3 shows how the photothermal reduction of graphite oxide can lead to high-surface area graphene. This prevents the graphene sheets from restacking and allows for the fabrication of ultra-high power supercapacitors for energy storage.

Chapter 4 discusses how the simple, scalable modification of reverse osmosis (RO) membrane surfaces with perfluorophenyl azide molecules can prevent initial bacterial adhesion, thus creating antifouling RO membranes that can last much longer than their conventional commercial counterparts. Chapter 5 looks at how anchoring graphene oxide onto polyamide RO membrane surfaces can render them more hydrophilic, smooth, and ultimately antimicrobial, with considerable resistance to protein fouling and biofouling.

This dissertation of Kristofer Lee Marsh is approved.

Xiangfeng Duan

Shaily Mahendra

Richard B. Kaner, Committee Chair

University of California, Los Angeles

2017

Table of Contents

LIST OF FIGURES vii

LIST OF TABLES AND SCHEMES x

ACKNOWLEDGMENTS xi

VITA xv

CHAPTER 1: Introduction 1
- 1.1 Chemical surface science – a brief introduction 2
- 1.2 X-ray photoelectron spectroscopy 3
- 1.3 Surface and interfacial science research specific to this dissertation 5
  - 1.3.1 Hexagonal boron nitride 6
  - 1.3.2 Graphene and graphite oxide 7
  - 1.3.3 Polymeric membranes for water filtration 9
- References 12

CHAPTER 2: Co-Solvent Exfoliation and Suspension of Hexagonal Boron Nitride 16
- 2.1 Background 17
- 2.2 Materials and methods 19
- 2.3 Characterization 20
- 2.4 Results and discussion 22
- 2.5 Conclusion 27
- 2.6 Acknowledgments 28
- References 29

CHAPTER 3: Flash Converted Graphene for Ultra-High Power Supercapacitors 31
- 3.1 Background 32
- 3.2 Experimental methods and characterization 36
  - 3.2.1 Preparation and fabrication of pre-FCG electrodes 36
  - 3.2.2 Preparation and fabrication of post-FCG electrodes 37
  - 3.2.3 Morphology, composition, and properties 38
  - 3.2.4 Assembly of FCG electrodes into coin cell supercapacitor devices 39
  - 3.2.5 Calculations 40
  - 3.2.6 Electrochemical measurements 42
- 3.3 Results and discussion 43
- 3.4 Conclusions 58
- 3.5 Acknowledgments 59
- References 60

CHAPTER 4: Scalable Antifouling Reverse Osmosis Membranes Utilizing Perfluorophenyl Azide Photochemistry 64
4.1 Background 65
4.2 Experimental methods and characterization 69
4.2.1 Materials 69
4.2.2 Instrumentation 69
4.2.3 Synthesis of PFPA-PEG_{5000} 70
4.2.4 Synthesis of PFPA-PEG_{1000} 71
4.2.5 Synthesis of PFPA-PEG_{550} 72
4.2.6 Membrane characterization 73
4.2.7 Surface modification procedure 73
4.2.8 Water permeability and rejection 74
4.2.9 Cell adhesion tests 75
4.3 Results and discussion 76
4.4 Conclusions 82
4.5 Acknowledgments 82
References 83

CHAPTER 5: Low-Fouling Antibacterial Reverse Osmosis Membranes via Surface Grafting of Graphene Oxide 86
5.1 Background 87
5.2 Results and Discussion 90
5.2.1 Synthesis of azide-functionalized GO 90
5.2.2 X-ray photoelectron spectroscopy 93
5.2.3 Atomic force microscopy 94
5.2.4 Membrane permeability and rejection 95
5.2.5 Bacterial adhesion 97
5.3 Conclusion 99
5.4 Acknowledgments 99
References 100

CHAPTER 6: Conclusions and Summary 103

LIST OF FIGURES

Figure 1.1 Illustration of the top three surface layer regimes as outlined by Vickerman and Gilmore.

Figure 1.2 Schematic of a typical XPS spectrometer.

Figure 1.3 Schematic illustration of the fabrication of laser-scribed graphene-based electrochemical capacitors. (A to D) A GO film supported on a flexible substrate is placed on top of a LightScribe-enabled DVD media disc, and a computer image is then laser-irradiated on the GO film in a computerized LightScribe DVD drive. (E) As shown in the photograph, the GO film changes from golden brown color to black as it reduced to laser-scribed graphene. The low-power infrared laser changes the stacked GO sheets immediately into well-exfoliated few-layered LSG film, as shown in the cross-sectional SEM images. (F) A symmetric EC is constructed from two identical LSG electrodes, ion-porous separator, and electrolyte.

Figure 1.4 Biological fouling of a spiral-wound RO module from a municipal desalination plant. The SEM images revealed microorganisms contained in a thick brown film that accumulated on the membrane surface.

Figure 2.1 Preparation of TEM samples. The lacey Formvar/carbon copper grid (400 mesh) is prepared on top of a piece of filter paper. This helps to quickly wick away the solvent from the exfoliated BNNS.

Figure 2.2 UV-vis data for BNNS in different co-solvent systems. Absorbance values were recorded at 400 nm; all data were averaged over five trials. From left to right, both the vials and the data points represent 100, 90, 80, 70, 60, 50, 40, 30, 20, 10, and 0 w/w% solvent in water. There are 11 vials present for both 1-prop (d) and IPA (e) to include 0 w/w% solvent (pure water), which can be seen as the rightmost vial in each photo.

Figure 2.3 Comparison of the maximum absorbance (A_{max}) and molecular weight (M.W.) with respect to surface tension for solvents with like chemistries. Each vertically aligned pair of data points represent: (a) *t*BA, (b) IPA, (c) 1-prop, (d) EtOH, and (e) MeOH.

Figure 2.4 TEM micrographs of BNNS after sonication for 3 h in 60% *t*BA. (a) A few-layered BNNS sample. A carbon support can be seen through the exfoliated sheet. (b) The magnified image of the square outline from (a). (c) Evidence for scrolling of the BNNS. The bright white ‘‘lines’’ are where the sheets have scrolled. (d) Diffraction pattern of a few-layered BNNS. Scale bars represent (a) 100 nm, (b) 10 nm, and (c) 0.5 mm.

Figure 2.5 TEM micrograph of a partially exfoliated BNNS. The two sheets share similar shapes. Scale bar is 200 nm.

Figure 3.1 Graphene electrodes: A) A smooth chemically converted graphene membrane. B) A rougher, expanded graphene membrane made by photothermal conversion of graphene oxide.

Figure 3.2 Cyclic voltammetry of FCG devices cycled at 100 mV/s from 1.0 V up to 3.0 V to determine the stable operating voltage. Based on these curves, an operating voltage of 2.0 V was selected.

Figure 3.3 GC-MS spectra of gas after flashing freeze-dried GO in a sealed vial filled with argon.

Figure 3.4 SEM images of A–C) pre-FCG, D–F) post-FCG at 0.5k, 2k, and 5k magnification showing the corrugated porous morphology.

Figure 3.5 SEM images of dried unreduced graphene oxide film at 0.1 k, 0.2 k, 5 k, 10 k magnification showing a different morphology from pre-FCG and post-FCG. Graphene oxide is a continuous film relative to FCG, and is seen to have a less porous structure.

Figure 3.6 ET nitrogen (77 K) adsorption isotherms for FCG powder used in the electrodes (top) and for graphene oxide (GO) (bottom). The FCG BET surface area is 733 $m^2 g^{-1}$, whereas the BET surface area of the freeze-dried GO is only 15 $m^2 g^{-1}$.

Figure 3.7 XPS high-resolution C 1s spectra of pre-FCG (top) and post-FCG (bottom). The spectral component at 284.6 eV (red) corresponds to sp^2 carbon. Oxygen containing groups, such as C-OH, C=O/C-O-C, and –COOH are shown at 286.7 eV (blue), 288.0 eV (green), and 289.3 eV (orange), respectively.

Figure 3.8 X-ray diffraction pattern comparing flash converted graphene used for electrodes (pre-FCG and post-FCG) to GO. A distinct peak in the GO pattern can be seen at 12° 2θ, but only small diffraction peaks are present for pre-FCG and no peaks for post-FCG. The lack of peaks indicates a disordered 3D morphology.

Figure 3.9 Electrochemical performance of A, B) pre-FCG and C, D) post-FCG supercapacitor devices. A, C) Cyclic voltammetry of pre-FCG and post-FCG at scan rates of 100, 200, 600, and 1000 mV s^{-1}. The nearly rectangular shape indicates essentially pure capacitive charging through electrochemical double layers. B, D) Constant current charge–discharge curves of pre FCG and post-FCG at 1, 10, and 50 A $g^{-1}_{FCG/electrode}$.

Figure 3.10 Electrochemical impedance spectroscopy: a Nyquist plot of A) pre-FCG and B) post FCG devices. The insets expand the high-frequency region.

Figure 3.11 Bode plot of pre-FCG (top) and post-FCG (bottom) coin cell devices measured from 1 MHz to 10 mHz at open circuit potential. The time constant is taken from the -45° frequency, where the device exhibits 50% capacitive and 50% resistive characteristics.

Figure 3.12 Constant current charge–discharge cycling at a current density of 1 A g^{-1}.

Figure 3.13 Ragone plot illustrating the high specific power of pre-FCG and post-FCG supercapacitor devices as compared to other state-of-the-art graphene-based supercapacitors devices.

Figure 4.1 Synthesis of PFPA-terminated PEG brush polymers and their attachment to an RO membrane surface.

Figure 4.2 ^{1}H NMR spectrum of PFPA-PEG_{5000} (^{19}F NMR inset).

Figure 4.3 ^{1}H NMR spectrum of PFPA-PEG_{1000} (^{19}F NMR inset).

Figure 4.4 ^{1}H NMR spectrum of PFPA-PEG_{550} (^{19}F NMR inset).

Figure 4.5 Dip-coating and modification of commercial membrane coupons with UV light.

Figure 4.6 ATR-IR spectroscopy of the commercial polyamide RO membrane and modified membranes. Apparent contact angle images are shown in the photos on the left.

Figure 4.7 Effect of UV exposure on a bare membrane and PFPA-PEG_{5000}-coated membrane (left) and contact angle versus UV exposure time for a PFPA-PEG_{5000}-coated membrane (right).

Figure 4.8 XPS survey spectra and N 1s spectra (inset) of the unmodified (left) and modified (right) RO membrane surfaces.

Figure 4.9 A) Pure water permeability (left axis) and rejection of NaCl (right axis). B) Observed adhesion of *E. coli* onto PFPA-PEG-modified membranes. Scale bar = 50 μm.

Figure 5.1 Synthesis of azide functionalized graphene oxide (AGO) and its attachment onto a polyamide RO membrane surface via UV activation of azide functional groups.

Figure 5.2 FT-IR spectra of GO and AGO show that after the azidation reaction, a new azide peak (2123 cm^{-1}) is observed in the AGO spectrum. This provides evidence for the successful bonding of azide groups onto the GO backbone.

Figure 5.3 AFM height analysis of AGO shows that AGO exhibits a planar morphology with an average thickness of 1.15 nm (inset).

Figure 5.4 After GO grafting on the polyamide RO membrane surface, (a) the water contact angle decreased from 85° to 45° and (b) the average surface roughness decreased from 44.3 nm to 29.0 nm based on a 5 μm × 5 μm analyzed area.

Figure 5.5 (a) Long-term BSA fouling test on the control and modified membranes showing the differences in flux decline; (b) Fluorescence and SEM images showing the percentages and condition of *Escherichia coli* cells on membrane surfaces after contact for 24 h; (c) Quantitative analysis of live (green) and dead (red) cell percentages on both membrane surfaces.

LIST OF TABLES AND SCHEMES

Tables

Table 1.1 Literature C1s XPS binding energies of functional groups in graphitic and graphenic systems.

Table 2.1 Surface tension values of common aqueous mixture at 25 °C as obtained from the *Handbook of Chemistry and Physics*, CRC Press, 2003, 84th edition. Data for *tert*-butanol comes from Gliński *et al.*, *J. Chem. Phys.*, 1995, 102, 1361. Note: 1 mN/m = 1 mJ/m^2.

Table 3.1 Comparison of FCG and state-of-the-art graphene supercapacitors.

Table 3.2 Comparison of FCG and commercial CR2032 supercapacitors.

Table 5.1 XPS surface atomic composition for AGO powder and RO membranes.

Schemes

Scheme 3.1 Schematic diagram of ions from the electrolyte absorbing onto the accessible surfaces of the electrode active material. A) Ion adsorption occurs only at the surface of the electrode film because of its densely-packed morphology. B) Ion adsorption occurs throughout the electrode active material because of its less dense corrugated 3D morphology.

Scheme 3.2 The two methods for making FCG electrodes: A) Pre-coated flash conversion (pre-FCG) and B) Post-coated flash conversion (post-FCG).

ACKNOWLEDGMENTS

Firstly, I would like to thank my advisor, Professor Richard Kaner, for his understanding, guidance, and wisdom. Ric allowed me to pursue my research interests without restriction, and gave me guidance when I was stuck. Over the years, I have learned from Ric that the relationships formed with others around research projects are perhaps what matter most, and that if you help someone out, the universe will likely return the favor in some unsuspecting way. Ric was most supportive to me during my third and fourth years, when I found it difficult to continue with my research. His almost paternal guidance was no doubt a key reason I was able to persevere and finish my degree.

Next, I'd like to thank the numerous friends and colleagues I worked with in the Kaner lab, the so-called "Kanerlings" (as we appropriately referred to each other sometimes in our mass group emails): Jaime Torres, Tom Farrell, Sergey Dubin, Jonathan Wassei, Maher El-Kady, Reza Mohammadi, Chris Turner, Matt Kowal, Xinwei (William) Huang, Dukwoo Jun (DJ), Lisa Wang, Jee Youn Hwang, Georgiy Akopov, Jialin Lei, Mengping Li, Haosen Wang, Cheng-Wei Lin, Daniel Maung, Wai Mak, Michael Yeung, Ploy Udomphol, Nanetta Pon, Mina Souliman, Amylynn Chen, Lindsay Chaney, Jacqueline (Jackie) Yang, Ethan Rao, Mit Muni, Lisa Pangilinan, Stephanie Aguilar, and Volker Strauss.

I'd also like to thank my friends from outside the group, both from within and outside the department, for making my experience at UCLA more enjoyable and mind-expanding: Jeff McCormick, Jonathan Brown, Robin Möller-Gulland, Mr.

Maxwell P. Salter, Nanette Jarenwattananon, Benjamin Finck, Dr. Stefan Glöggler, Orin Yue, Hemal Semwal, Henry Sillin, Michelle Oishi, Jessie Grandner, Ben Lesel, Kelly Flickinger, Ben Harounian, Dr. Matthew Altmire, the members of the UCLA Marching Band, and the UCLA EDMC.

I would not have had nearly as much curiosity about the art of XPS analysis if it were not for my mentor during my time doing research at Johns Hopkins University, Professor Howard Fairbrother. I'd also like to thank Dr. Ignacio Martini from the UCLA Molecular Instrumentation Center for fixing all the XPS equipment I likely broke, and for helping me learn the ins and outs of the machine. Many thanks too to my friends and colleagues from Hopkins who inspired me to do more with XPS and to attend graduate school: David Goodwin, Samantha Rosenberg, Julie Bitter, Jin Yang, Michael Barclay, and Kevin Wepasnik.

Special thanks go out to the staff at UCLA CAPS; namely Michal Scharlin, Colby Moss, Dr. Rachel Partiali, and Dr. Anupama Kalsi.

Thank you to my loving girlfriend, Sarah, for her constant support and for showing me true companionship. In the final year of my PhD she taught me how to pull my socks up while not throwing my toys out' the pram. Learning these phrases was well confusing, but half the time I figured she was just taking the piss out of me, so I'm sure she was proper buzzin' about that. There are probably more silly British phrases she taught me, but I can't be arsed to remember them.

Finally, I'd like to thank my parents, Jane and David, my brother and sister, Patrick and Alison, and my Mom Mom, Regina, for their love and support. Mom

always somehow sensed when I needed a pick-me-up dose of Fisher's popcorn or a crab cake sent from home, which I greatly appreciated. I'd also like to send a shout out to my dog, Roxy, and my cat, Neuvy.

During my time at UCLA I was fortunate to have collaborated on various projects with several of my friends, colleagues, and mentors. This aspect of my research has come to define my doctoral experience, and without doubt has also come to shed a personal light on aspects of myself I did not know existed prior to enrolling in the program five years ago. Indeed, much of the work herein is based on published, peer-reviewed articles I was involved with that were not wholly my own. For all content based on publications for which I was not the first author, my contributions can be summarized as having provided in-depth collection, processing, and analysis of X-ray photoelectron spectroscopy data, in addition to thoughtful conversation and help writing sections of each manuscript.

Chapters 2, 3, 4, and 5 are based on published, peer-reviewed articles in high impact journals as follows, respectively: Kristofer L. Marsh, Mina Souliman, and Richard B. Kaner, "Co-solvent exfoliation and suspension of hexagonal boron nitride," *Chemical Communications*, **2015**, 51, 187; Lisa J. Wang, Maher F. El-Kady, Sergey Dubin, Jee Youn Hwang, Yuanlong Shao, Kristofer Marsh, Brian McVerry, Matthew D. Kowal, Mir F. Mousavi, and Richard B. Kaner, "Flash converted graphene for ultra-high power supercapacitors," *Advanced Energy Materials*, **2015**, 5, 1500786; Brian T. McVerry, Mavis C. Y. Wong, Kristofer L. Marsh, James

A. T. Temple, Catalina Marambio-Jones, Eric M. V. Hoek, and Richard B. Kaner, "Scalable antifouling reverse osmosis membranes utilizing perfluorophenyl azide photochemistry," *Macromolecular Rapid Communications*, **2014**, 35, 1528-1533; and Xinwei Huang, Kristofer L. Marsh, Brian T. McVerry, Eric M. V. Hoek, and Richard B. Kaner, "Low-fouling antibacterial reverse osmosis membranes via surface grafting of graphene oxide," *ACS Applied Materials & Interfaces*, **2016**, 8, 14334-14338.

VITA

Education:

Bachelor of Science in Chemistry August 2006 – May 2011
Towson University
Towson, MD, 21252

Publications, Presentations, & Patents:

Jordan, R. S.; Wang, Y.; McCurdy, R. D.; Yeung, M. T.; Marsh, K. L.; Khan, S. I.; Kaner, R. B.; Rubin, Y. Synthesis of graphene nanoribbons via the topochemical polymerization and subsequent aromatization of a diacetylene precursor. *Chem* **2016**, 1, 78-90.

Huang, X.; Marsh, K. L.; McVerry, B. T.; Hoek, E. M. V.; Kaner, R. B. Low-fouling antibacterial reverse osmosis membranes via surface grafting of graphene oxide. *ACS Appl Mater Interfaces* **2016**, 8, 14334–14338.

Shao, Y.; El-Kady, M. F.; Lin, C.-W.; Zhu, G.; Marsh, K. L.; Hwang, J. Y.; Zhang, Q.; Li, Y.; Wang, H.; Kaner, R. B. 3D freeze-casting of cellular graphene films for ultrahigh-power-density supercapacitors. *Adv Mater* **2016**, 28, 6719-6726.

Sarparast, M.; Noori, A.; Ilkhani, H.; Bathaie, S. Z.; El-Kady, M. F.; Wang, L. J.; Pham, H.; Marsh, K. L.; Kaner, R. B.; Mousavi, M. F. Cadmium nanoclusters in a protein matrix: Synthesis, characterization, and application in targeted drug delivery and cellular imaging. *Nano Research* **2016**, 9, 3229-3246.

Marsh, K. L.; Souliman, M.; Kaner, R. B. Co-solvent exfoliation and suspension of hexagonal boron nitride. *Chem Commun* **2015**, 51 187-190.

Marsh, Kristofer L. "Process for exfoliation and dispersion of boron nitride." Patent application PCT/US15/49381, filed September **2015**.

Goodwin, D.; Marsh, K. L.; Boyer, I.; Payne, J.; Gorham, J.; Bouwer, E.; Fairbrother, D. H. Interactions of microorganisms with polymer nanocomposite surfaces containing oxidized carbon nanotubes. *Environ Sci Technol* **2015**, 49, 5484-5492.

Hwang, J. Y.; El-Kady, M. F.; Wang, Y.; Wang, L.; Shao, Y.; Marsh, K.; Ko, J. M.; Kaner, R. B. Direct preparation and processing of graphene/RuO_2 nanocomposite electrodes for high-performance capacitive energy storage. *Nano Energy* **2015**, 18, 57-70.

Wang, L. J.; El-Kady, M. F.; Dubin, S.; Hwang, J. Y.; Shao, Y.; Marsh, K.; McVerry, B.; Kowal, M. D.; Mousavi, M. F.; Kaner, R. B. Flash converted graphene for ultra-high power supercapacitors. *Adv Energy Mater* **2015**, 5, 1500786.

McVerry, B. T.; Wong, M. C. Y.; Marsh, K. L.; Temple, J. A. T.; Marambio-Jones, C.; Hoek, E. M. V.; Kaner, R. B. Scalable antifouling reverse osmosis membranes utilizing perfluorophenyl azide photochemistry. *Macromol Rapid Commun* **2014**, 35, 1528-1533.

Marsh, K. L.; Kaner, R. B.; Strong, V.; D'Arcy, J.; Wassei, J.; Wang, J. Y.; El-Kady, M. F.; Dubin, S.; Farrell, T.; Torres, J.; Wang, K.; Wang, L. Polyaniline, graphite oxide, and graphene colloids for device applications. From 87th ACS Colloid and Surface Science Symposium, Riverside, CA, Unites States, June 23-26, **2013**, COLLSYMP-76.

McVerry, B. T.; Temple, J. A. T.; Huang, X.; Marsh, K. L.; Hoek, E. M. V.; Kaner, R. B. Fabrication of low-fouling ultrafiltration membranes using a hydrophilic, self-doping polyaniline additive. *Chem Mater* **2013**, 25, 3597-3602.

Reed, R. B.; Goodwin, D. G.; Marsh, K. L.; Capracotta, S. S.; Higgins, C. P.; Fairbrother, D. H.; Ranville, J. F. Detection of single walled carbon nanotubes by monitoring embedded metals. *Env Sci Process Impact* **2013**, 15, 204-213.

Ajmani, G. S.; Goodwin, D.; Marsh, K.; Fairbrother, D. H.; Schwab, K. J.; Jacangelo, J. G.; Huang, H. Modication of low pressure membranes with carbon nanotube layers for fouling control. *Water Res* **2012**, 46, 5645-5654.

Non-Academic Positions:

Skywell, LLC – Santa Monica, CA
Senior Water Quality Engineer, January 2017 - Present

Walt Disney Imagineering – Glendale, CA
Intern – Applied Science, Summer 2016

Honors and Awards:

Hanson Dow Excellence in Teaching Award, 2016
Member, Norma Stoddart Prize Selection Committee, 2016
Honorable Mention, NSF Graduate Research Fellowship Program, 2014
Honorable Mention, NSF Graduate Research Fellowship Program, 2013
Towson University Honors Scholar

CHAPTER 1

Introduction

1.1 Chemical surface science – a brief introduction

Research in materials chemistry often revolves around various properties: capacitance, thermal and electrical conductivity, hardness, wettability; the list goes on. Unique to the chemistry of materials, as opposed to the chemistry of small molecules, for instance, is the consideration of both a given material's bulk properties as well as that material's surface properties. According to Vickerman and Gilmore, the "surface" can itself be stratified into three regimes: the top surface monolayer, the first ten (approximately) atomic layers, and the surface film (no greater than 100 nm)[1] (Figure 1.1). The surface chemistry of a given material may or may not be the same as that material's bulk, solid state chemistry.

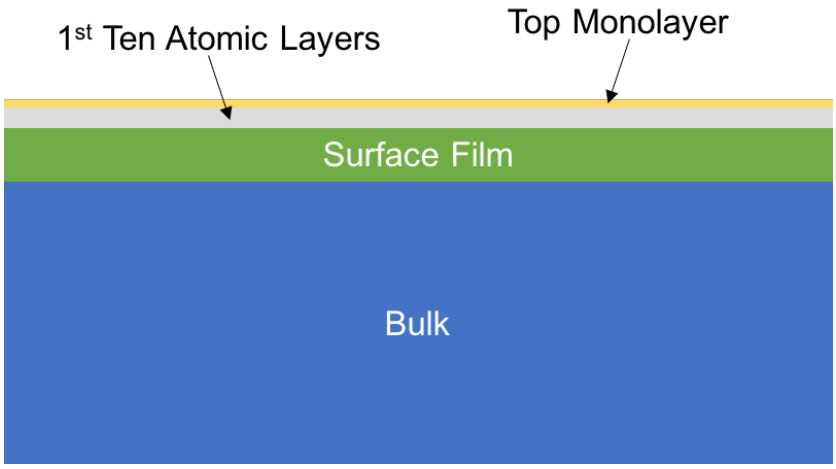

Figure 1.1. Illustration of the top three surface layer regimes as outlined by Vickerman and Gilmore.[1]

For example, iron often corrodes in harsh, oxidizing environments, thus producing a surface layer of hydrated iron oxide. This is widely known as rust. Iron oxide has distinctly different properties than its reduced, bulk counterpart,

the most obvious of which might be its color: iron oxide as rust is usually red, whereas pure iron is a grey, shiny metal. Rust is also much more brittle than iron.[2] Another example lies in the common aluminum soda can.[2] Without the existence of a highly engineered Al_2O_3 oxide layer, soft drink cans would rust easily, rendering them unacceptable and impractical for use in human consumption.

In materials chemistry, much research focuses on modifying or designing surfaces to function in a predetermined way; this is commonly known as "functionalizing" a surface. For example, Goodwin *et al.* functionalized the surfaces of carbon nanotubes with oxygen functional groups, such as carboxyl and carbonyl groups, in order to more easily disperse the tubes into a polymer matrix to determine their antimicrobial properties.[3] Many areas of research including drug delivery, energy, water filtration, catalysis, and more rely on the specific functionality and properties of surfaces.[4-7]

1.2 X-ray Photoelectron Spectroscopy

Perhaps the most widely used of the contemporary surface analytical techniques is electron spectroscopy for chemical analysis (ESCA), which is also commonly called X-ray photoelectron spectroscopy or XPS. XPS is based on the photoelectric effect, measuring the kinetic energy of electrons as they are ejected from a material after exposure to electromagnetic radiation (which in the case of XPS is of course X-rays) (Figure 1.2). XPS is popular largely because it is an

extraordinarily sensitive technique, with a detection limit in the parts-per-million to parts-per-billion range.

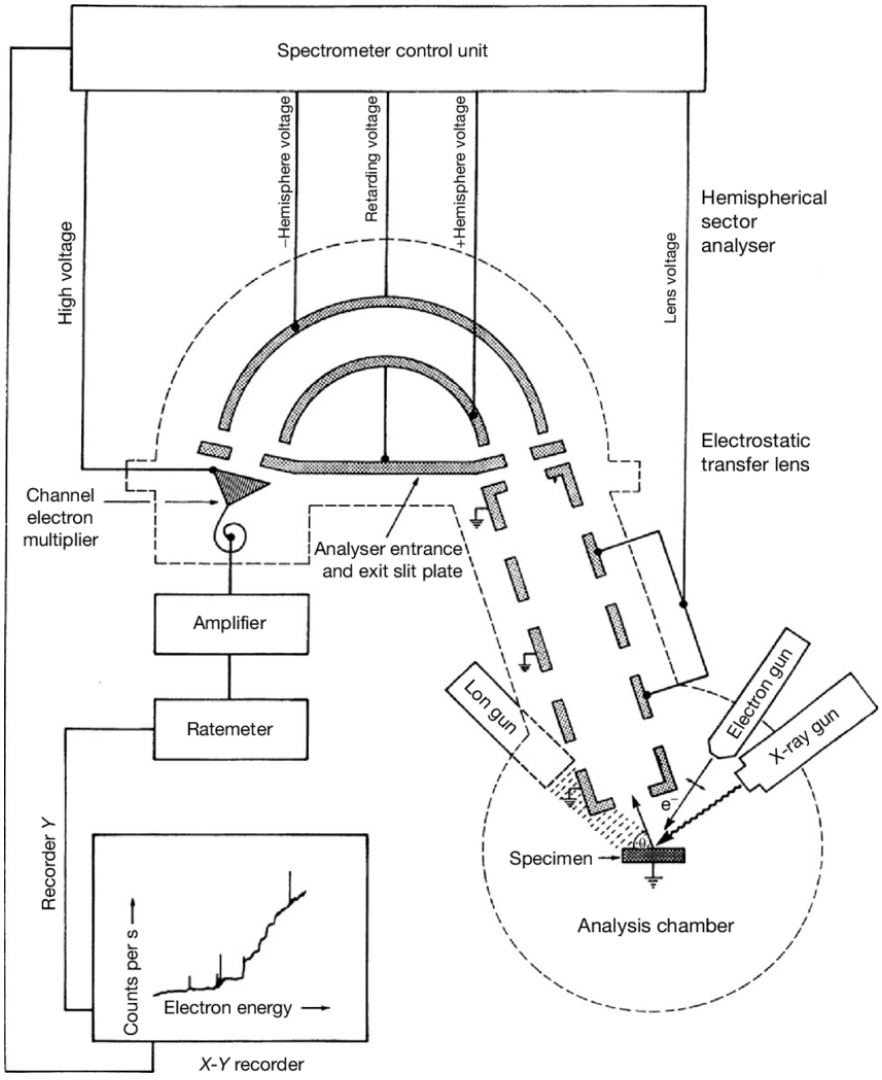

Figure 1.2. Schematic of a typical XPS spectrometer.[8]

XPS is useful for determining the different surface chemical species of a material. For example, graphite oxide is comprised of several different types of oxygen functional groups, including hydroxyl, epoxide, carbonyl, and carboxyl

species.[9] Normally these groups would be very difficult to differentiate using other techniques, such as energy dispersive spectroscopy (EDS), but XPS allows for the deconvolution of such groups by utilizing high-resolution spectral scanning and reference binding energies (Figure 1.3).[10,11] Several of the later chapters in this dissertation are based on work involving the use of XPS to determine the surface chemical structure and composition of graphene, graphite oxide, and even polymer membranes.

C-ring π^*	Hydroxyl C−O	Epoxide C−O−C	Carbonyl C=O	Carboxyl COOH	Carbonate CO_3	Ref.
	286.7	287.2		288.2		[49]
285.0	286.4	287.2		289.4		[35]
284.9 - 285.1	286.3 - 286.9	287.2 - 287.8		289.0 - 289.6		[50]
284.6 - 285.1	286.3 - 287.0		287.5 - 288.1	289.3 - 290.0		[51]
284.1	286.7	288.3			290.0	[52]
284.8	286.2		287.8	289.0		[53]
284.5	286.5				290.5	[54]
284.6	286.1		287.5	289.2		[55]
284.6	286.6		288.5			[56]
284.3	286.1		287.4	288.1		[57]

Table 1.1. Literature C1s XPS binding energies of functional groups in graphitic and graphenic systems.[11]

1.3 Surface and interfacial science research specific to this dissertation

Each chapter within this dissertation discusses a different, niche aspect of surface or interfacial science. The main materials examined are hexagonal boron nitride, graphene, graphite oxide, and water filtration membranes.

1.3.1 Hexagonal boron nitride

Hexagonal boron nitride (h-BN), often referred to as "white graphite," is isoelectronic with its carbon counterpart, with covalently bound interplanar B and N atoms replacing C atoms to form the sp^2 hybridized network. h-BN is known for its lack of electrical conductivity, high thermal conductivity, excellent mechanical strength, and chemical stability.[12,13] Boron nitride nanosheets (BNNS) have also been confirmed to outperform their bulk counterpart in the areas of composite fillers, solid lubrication, and transistors. Traditional methods used for graphite exfoliation, such as ion intercalation, mechanical delamination, or chemical reduction (e.g. reduction of graphite oxide to form graphene), do not transfer to h-BN, despite the two having almost identical interlayer spacings. The differences in electronegativity between B and N atoms cause π electrons to localize around N atomic centers, and it is this polarity that causes interlayer electrostatic interactions between the partially positive B and partially negative N atoms.[14] This results in a complex mix of multipole and dispersion interactions as well as Pauli repulsions that result in a similar interlayer distance to graphite, despite having radically different electronic properties.

The most common methods for producing BNNS are chemical vapor deposition (CVD) and liquid exfoliation.[15,16–20] CVD allows for control of the growth process, and almost guarantees a low-defect, single atomic sheet of h-BN. However, CVD is a high-temperature process that is difficult to scale up. Sinitskii *et al.* recently showed that BN nanoribbons can be obtained by the splitting of BN

nanotubes in the presence of potassium vapor;[21] however, this process deals with the handling of highly reactive potassium metal, which makes it unattractive for high throughput synthesis.

Liquid exfoliation is a simple method to produce BNNS from bulk h-BN powder. Generally, h-BN powder is mixed with a solvent, and energy, usually ultrasonic energy, is introduced into the system. However, many of these solvents, such as dimethyl sulfoxide (DMSO) or *N*-methylpyrrolidone (NMP), are harmful and/or dangerous to work with. There have also been a few studies describing the exfoliation of h-BN using water as a solvent. Connell *et al.* recently showed that water serves a critical role in h-BN exfoliation, hydrolyzing planar defects to introduce hydroxyl groups that help to stabilize the suspended BNNS.[22] In Chapter 2 a method is presented for producing BNNS from bulk h-BN powders using a simple co-solvent approach.

1.3.2 Graphene and graphite oxide

Perhaps no other material has garnered such focused research and attention thus far in the twenty-first century as has graphene. Graphene is a single sheet of sp^2 hybridized carbon atoms with extraordinary chemical, structural, and electrical properties, among others.[23] Research on graphene has been heavily invested into its electrical capabilities and its implications in emerging energy storage applications.

When used in supercapacitor electrodes, for example, graphene's planar structure gives rise to fast charging and discharging because electrolyte ions can readily access the large surface areas of the sheets.[24,25] The efficient transport of ions between the electrolyte and graphene surfaces is advantageous for high power and rate capabilities and rapid response times. However, processing graphene can be problematic. The planar aromatic sheets often restack due to favorable π–π interactions between adjacent sheets.[26,27] Upon restacking, the graphene is converted back into a graphite-like material and no longer possesses the high surface area of single layer graphene, reducing the material's high power and rate capabilities.[28] Chapter 3 discusses the use of photothermal techniques to overcome these limitations.

Graphene is commonly prepared via the reduction of graphite (or graphene) oxide (GO). Amazing is the fact that Hummers *et al.* developed a technique for the preparation of GO over back in 1958[29], but it took another forty-five years after this publication for scientists to successfully discover and research its reduced, single-sheet counterpart[23,30]. The oxygen functionalities present in GO allow for it to be easily processed and manipulated in aqueous and organic solvents, which is especially useful in the preparation of graphene electrodes and supercapacitors (Figure 1.3).[31] GO is also known to possess antimicrobial properties; this is discussed in Chapter 5.

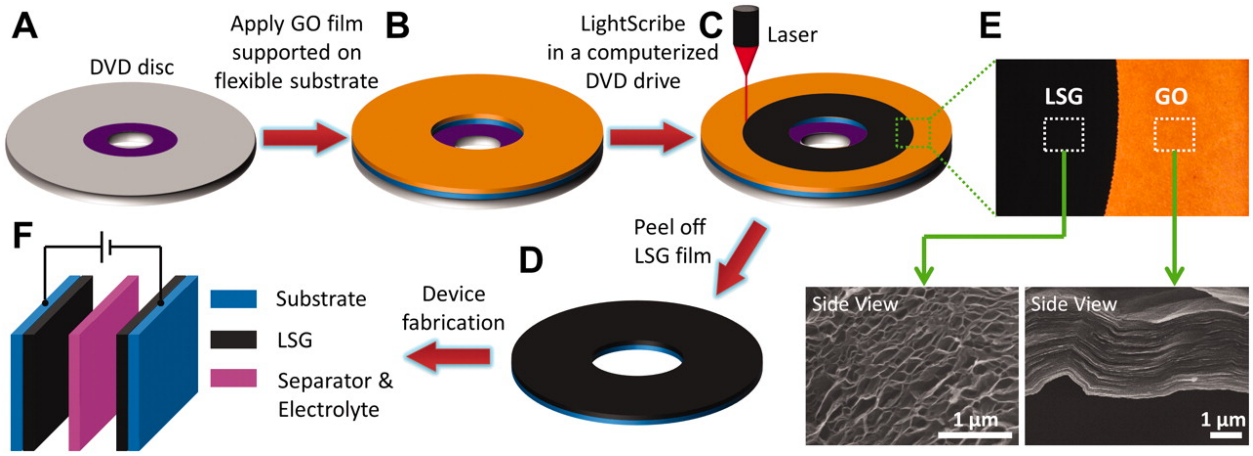

Figure 1.3. Schematic illustration of the fabrication of laser-scribed graphene-based electrochemical capacitors. (A to D) A GO film supported on a flexible substrate is placed on top of a LightScribe-enabled DVD media disc, and a computer image is then laser-irradiated on the GO film in a computerized LightScribe DVD drive. (E) As shown in the photograph, the GO film changes from golden brown color to black as it reduced to laser-scribed graphene. The low-power infrared laser changes the stacked GO sheets immediately into well-exfoliated few-layered LSG film, as shown in the cross-sectional SEM images. (F) A symmetric EC is constructed from two identical LSG electrodes, ion-porous separator, and electrolyte.[31]

1.3.3 Polymeric membranes for water filtration

Membrane filtration is a common method of purifying water to render it drinkable by humans. Products such as the LifeStraw utilize microfiltration technology to allow consumers to drink safely from virtually any water source,[32] and reverse osmosis (RO) filtration has become a popular method of further cleaning and polishing drinking water in the home kitchen. Further, RO has become established as an effective means of providing clean water on the municipal scale. RO desalination treatment plants like those located in Ashkelon, Israel[33] and Carlsbad, CA offer more options to coastal cities in need of additional sources of potable water.

The most problematic aspect of membrane filtration is the phenomenon of fouling. Fouling, colloquially referred to sometimes as “clogging,” occurs when organic or inorganic particles deposit on the surface of the membrane to such an extent that the membrane flux, or flow, is severely inhibited.[34] From a practical standpoint, this decline in flux leads to higher pressures and therefore more energy consumption, which translates into higher operational and maintenance costs.[35]

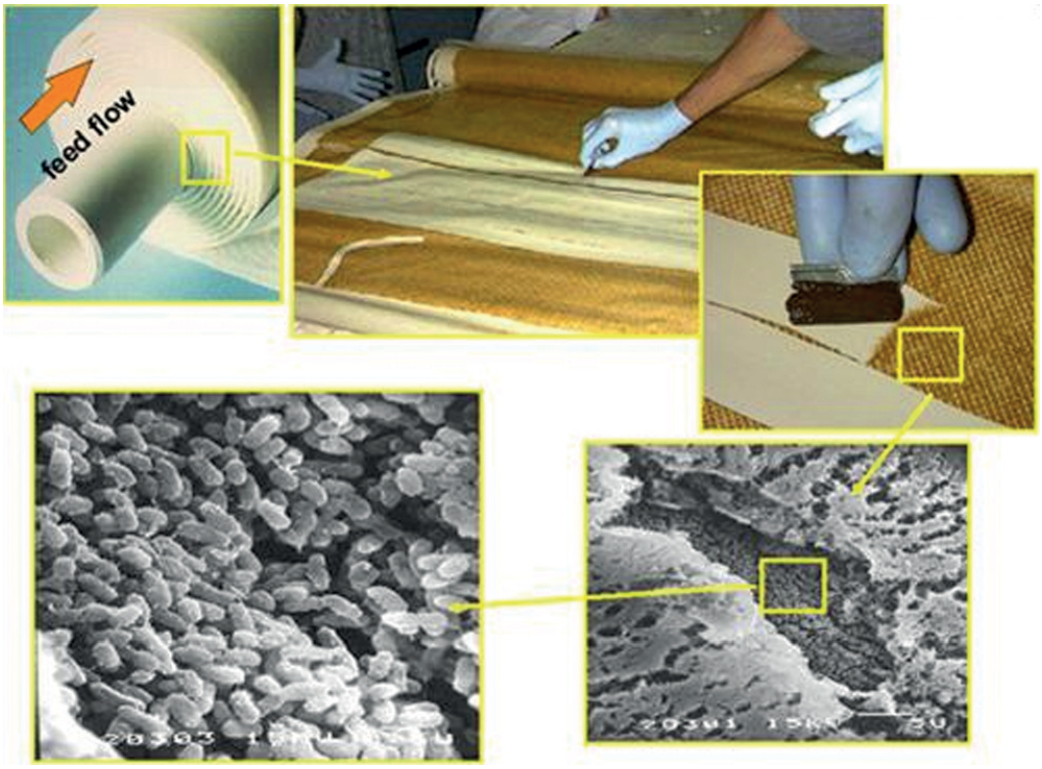

Figure 1.4. Biological fouling of a spiral-wound RO module from a municipal desalination plant. The SEM images revealed microorganisms contained in a thick brown film that accumulated on the membrane surface.[6,36]

Unfortunately, the most popular method of cleaning membranes, chlorination, is destructive to the polymer materials used in their manufacture. This has led scientists and engineers to design surface treatments and modifications for existing membranes to make them more resistant to fouling altogether.[6,37-40] Chapters 3, 4, and 5 discuss how small molecules and graphite oxide can be used to enhance the antifouling properties of water filtration membranes, specifically RO membranes.

References

(1) Vickerman, J. C.; Gilmore, I. S. *Surface Analysis: The Principal Techniques,* 2nd ed. John Wiley & Sons, Inc., West Sussex, United Kingdom, **2009**.

(2) Waldman, J. *Rust: The Longest War*. Simon & Schuster, New York, NY, **2015**.

(3) Goodwin, D.; Marsh, K. L.; Boyer, I.; Payne, J.; Gorham, J.; Bouwer, E.; Fairbrother, D. H. Interactions of microorganisms with polymer nanocomposite surfaces containing oxidized carbon nanotubes. *Environ Sci Technol* **2015**, 49, 5484-5492.

(4) Paramasivam, G.; Kayambu, N.; Rabel, A. M.; Sundramoorthy, A. K.; Sundaramurthy, A. Anisotropic noble metal nanoparticles: Synthesis, surface functionalization and applications in biosensing, bioimaging, drug delivery and theranostics. *Acta Biomater* **2017**, 49, 45-65.

(5) Marchetti, A.; Chen, J.; Pang, Z.; Li, S.; Ling, D.; Deng, F.; Kong, X. Understanding surface and interfacial chemistry in functional nanomaterials, via solid-state NMR. *Adv Mater* **2017**, 29, 1605895.

(6) Miller, D. J.; Dreyer, D. R.; Bielawski, C. W.; Paul, D. R.; Freeman, B. D. Surface modification of water purification membranes. *Angew Chem Int Ed* **2017**, 56, 4662-4711.

(7) Fu, Q.; Bao, X. Surface chemistry and catalysis confined under two-dimensional materials. *Chem Soc Rev* **2017**, 46, 1842-1874.

(8) Tougaard, S. Surface Analysis | X-ray Photoelectron Spectroscopy. In: Reedijk, J. (Ed.) *Elsevier Reference Module in Chemistry, Molecular Sciences and Chemical Engineering.* Waltham, MA: Elsevier. 11-Sep-13 DOI: 10.1016/B978-0-12-409547-2.00527-8.

(9) Dreyer, D. R.; Park, S.; Bielawski, C. W.; Ruoff, R. S. The chemistry of graphite oxide. *Chem Soc Rev* **2010**, 39, 228-240.

(10) Jordan, R. S.; Wang, Y.; McCurdy, R. D.; Yeung, M. T.; Marsh, K. L.; Khan, S. I.; Kaner, R. B.; Rubin, Y. Synthesis of graphene nanoribbons via the topochemical polymerization and subsequent aromatization of a diacetylene precursor. *Chem* **2016**, 1, 78-90.

(11) Hunt, A.; Dikin, D. A.; Kurmaev, E. Z.; Boyko, T. D.; Bazylewski, P.; Chang, G. S.; Moewes, A. Epoxide speciation and functional group distribution in graphene oxide paper-like materials. *Adv Funct Mater* **2012**, 22, 3950-3957.

(12) Zhi, C.; Bando, Y.; Tang, C.; Kuwahara, H.; Golberg, D. Large-scale fabrication of boron nitride nanosheets and their utilization in polymeric composites with improved thermal and mechanical properties. *Adv. Mater.* **2009**, 21, 2889–2893.

(13) Lian, G.; Zhang, X.; Tan, M.; Zhang, S.; Cui, D.; Wang, Q. Facile synthesis of 3D boron nitride nanoflowers composed of vertically aligned nanoflakes and fabrication of graphene-like BN by exfoliation. *J. Mater. Chem.* **2011**, 21, 9201.

(14) Hod, O. Graphite and hexagonal boron-nitride have the same interlayer distance. Why? *J. Chem. Theory Comput.* **2012**, 8, 1360–1369.

(15) Nicolosi, V.; Chhowalla, M.; Kanatzidis, M. G.; Strano, M. S.; Coleman, J. N. Liquid exfoliation of layered materials. *Science* **2013**, 340, 1226419.

(16) Kim, G.; Jang, A.-R.; Jeong, H. Y.; Lee, Z.; Kang, D.J.; Shin, H.S. Growth of high-crystalline, single-layer hexagonal boron nitride on recyclable platinum foil. *Nano Lett.* **2013**, 13, 1834–1839.

(17) Kim, K. K.; Hsu, A.; Jia, X.; Kim, S. M.; Shi, Y.; Hofmann, M.; Nezich, d.; Rodriguez-Nieva, J. F.; Dresselhaus, M.; Palacios, T.; Kong, J. Synthesis of monolayer hexagonal boron nitride on Cu foil using chemical vapor deposition. *Nano Lett.* **2012**, 12, 161–166.

(18) Seth, M.; Hatzikiriakos, S. G.; Clere, T. M. Gross melt fracture elimination: The role of surface energy of boron nitride powders. *Polym. Eng. Sci.* **2002**, 42, 743–752.

(19) Coleman, J. N.; Lotya, M.; O'Neill, A.; Bergin, S. D.; King, P. J.; Khan, U.; Young, K.; Gaucher, A.; De, S.; Smith, R. J.; Shvets, I. V.; Arora, S. K.; Stanton, G.; Kim, H.-Y.; Lee, K.; Kim, G. T.; Duesberg, G. S.; Hallam, T.; Boland, J. J.; Wang, J. J.; Donegan, J. F.; Grunlan, J. C.; Moriarty, G.; Shmeliov, A.; Nicholls, R. J.; Perkins, J. M.; Grieveson, E. M.; Theuwissen, K.; McComb, D. W.; Nellist, P. D.; Nicolosi, V. Two-dimensional nanosheets produced by liquid exfoliation of layered materials. *Science* **2011**, 331, 568–571.

(20) Shi, Y.; Hamsen, C.; Jia, X.; Kim, K. K.; Reina, A.; Hofmann, M.; Hsu, A. L.; Zhang, K.; Li, H.; Juang, Z.-Y.; Dresselhaus, M. S.; Li, L.-J.; Kong, J. Synthesis of few-layer hexagonal boron nitride thin film by chemical vapor deposition. *Nano Lett.* **2010**, 10, 4134–4139.

(21) Sinitskii, A.; Erickson, K. J.; Lu, W.; Gibb, A. L.; Zhi, C.; Bando, Y.; Goldberg, D.; Zettl, A.; Tour, J. M. High-yield synthesis of boron nitride nanoribbons via longitudinal splitting of boron nitride nanotubes by potassium vapor. *ACS Nano* **2014**, 8, 9867–9873.

(22) Lin, Y.; Williams, T. V.; Xu, T.-B.; Cao, W.; Elsayed-Ali, H. E.; Connell, J. W. Aqueous dispersions of few-layered and monolayered hexagonal boron nitride nanosheets from sonication-assisted hydrolysis: critical role of water. *J. Phys. Chem. C* **2011**, 115, 2679–2685.

(23) Novoselov, K. S.; Geim, A. K.; Morozov, S. V.; Jiang, D.; Zhang, Y.; Dubonos, S. V.; Grigorieva, I. V.; Firsov, A. A. Electric field effect in atomically thin carbon films. *Science* **2004**, 306, 666-669.

(24) Lee, J.-S.; Kim, S.-I.; Yoon, J.-C.; Jang, J.-H. Chemical vapor deposition of mesoporous graphene nanoballs for supercapacitor. *ACS Nano* **2013**, 7, 6047.

(25) Lee, J. H.; Park, N.; Kim, B. G.; Jung, D. S.; Im, K.; Hur, J.; Choi, J. W. Restacking-inhibited 3D reduced graphene oxide for high performance supercapacitor electrodes. *ACS Nano* **2013**, 7, 9366.

(26) Xu, Y.; Bai, H.; Lu, G.; Li, C.; Shi, G. Flexible graphene films via the filtration of water-soluble noncovalent functionalized graphene sheets. *J. Am. Chem. Soc.* **2008**, 130, 5856.

(27) Luo, J.; Jang, H. D.; Huang, J. Effect of sheet morphology on the scalability of graphene-based ultracapacitors. *ACS Nano* **2013**, 7, 1464.

(28) Kim, T.; Jung, G.; Yoo, S.; Suh, K. S.; Ruoff, R. S. Activated graphene-based carbons as supercapacitor electrodes with macro- and mesopores. *ACS Nano* **2013**, 7, 6899.

(29) Hummers Jr., W. S.; Offeman, R. E. Preparation of graphite oxide. *J Am Chem Soc* **1958**, 80, 1339-1339.

(30) Viculis, L. M.; Mack, J. J.; Kaner, R. B. A chemical route to carbon nanoscrolls. *Science* **2003**, 299, 1361-1361.

(31) El-Kady, M. F.; Strong, V.; Dubin, S.; Kaner, R. B. Laser scribing of high-performance and flexible graphene-based electrochemical capacitors. *Science* **2012**, 335, 1326-1330.

(32) Elsanousi, S.; Abdelrahman, S.; Elshiekh, I.; Elhadi, M.; Mohamadani, A.; Habour, A.; ElAmin, S. E.; Elnoury, A.; Ahmed, E. A.; Hunter, P. R. A study of the use and impacts of LifeStraw ™ in a settlement camp in southern Gezira, Sudan. *J Water Health* **2009**, 7, 478-483.

(33) Molina, V. G.; Taub, M.; Yohay, L.; Busch, M. Long term membrane process and performance in Ashkelon seawater reverse osmosis desalination plant. *Desalin Water Treat* **2011**, 31, 115-120.

(34) Howe, K. J.; Clark, M. M. Fouling of microfiltration and ultrafiltration membranes by natural waters. *Environ Sci Technol* **2002**, 36, 3571–3576.

(35) Pandey, S. R.; Jegatheesan, V.; Baskaran, K.; Shu, L. Fouling in reverse osmosis (RO) membrane in water recovery from secondary effluent: A review. *Rev Environ Sci Bio/Technology* **2012**, 11, 125–145.

(36) Hoek, E. M. V.; Allred, J.; Knoell, T.; Jeong, B.-H. Modeling the effects of fouling on full-scale reverse osmosis processes. *J Membr Sci* **2008**, 314, 33-49.

(37) Belfer, S.; Purinson, Y.; Fainshtein, R.; Radchenko, Y.; Kedem, O. Surface modification of commercial composite polyamide reverse osmosis membranes. *J Membr Sci* **1998**, 139, 175–181.

(38) Van Wagner, E. M.; Sagle, A. C.; Sharma, M. M.; La, Y.-H.; Freeman, B. D. Surface modification of commercial polyamide desalination membranes using

poly(ethyleneglycol) diglycidyl ether to enhance membrane fouling resistance. *J Membr Sci* **2011**, 367, 273–287.

(39) Kang, G.; Yu, H.; Liu, Z.; Cao, Y. Surface modification of a commercial thin film composite polyamide reverse osmosis membrane by carbodiimide-induced grafting with poly(ethylene glycol) derivatives. *Desalination* **2011**, 275, 252–259.

(40) Zou, L.; Vidalis, I.; Steele, D.; Michelmore, A.; Low, S. P.; Verberk, J. Q. J. C. Surface hydrophilic modification of RO membranes by plasma polymerization for low organic fouling. *J Membr Sci* **2011**, 369, 420–428.

CHAPTER 2

Co-Solvent Exfoliation and

Suspension of Hexagonal Boron Nitride

2.1 Background

Two-dimensional materials have exploded in popularity following the advent of graphene. These materials include hexagonal boron nitride (h-BN), transition metal chalcogenides, and metal halides, among many others.[1] Particular interest has been focused toward the exfoliation of these materials into single- or few-layered (<20) atomic sheets. The nanosheet form of these materials allows access to exaggerated versions of their characteristics, such as high surface area and structural, electronic, and thermal properties.[1–3]

Often referred to as ‘‘white graphite,’’ h-BN is isoelectronic with its carbon counterpart, with covalently bound interplanar B and N atoms replacing C atoms to form the sp^2 ‘‘honeycomb’’ network. Hexagonal boron nitride is known for its lack of electrical conductivity, high thermal conductivity, excellent mechanical strength, and chemical stability.[3,4] Boron nitride nanosheets (BNNS) have also been confirmed to outperform their bulk counterpart in the areas of composite fillers, solid lubrication, and transistors. Traditional methods used for graphite exfoliation, such as ion intercalation, mechanical delamination, or chemical reduction (e.g. reduction of graphite oxide to form graphene), do not transfer to h-BN, despite the two having almost identical interlayer spacing (3.33–3.35 Å for graphite, vs. 3.30–3.33 Å for h-BN). The electronegativity differences between B and N atoms cause π electrons to localize around N atomic centers, and it is this polarity that causes interlayer electrostatic interactions between the partially positive B and partially negative N atoms.[5] This results in a complex mix of

multipole and dispersion interactions as well as Pauli repulsions that result in a similar interlayer distance to graphite, despite having radically different electronic properties.

Currently, the most popular routes for producing BNNS are through chemical vapor deposition (CVD) and liquid exfoliation.[1,6–10] CVD allows for control of the growth process, and almost guarantees a low-defect, single atomic sheet of h-BN. However, CVD is a high-temperature process that is difficult to scale up. Sinitskii *et al.* recently showed that BN nanoribbons can be obtained by the splitting of BN nanotubes in the presence of potassium vapor;[11] however, this process deals with the handling of highly reactive potassium metal, which makes it unattractive for high throughput synthesis.

Liquid exfoliation is a simple method to produce BNNS from bulk h-BN powder. Generally, h-BN powder is mixed with a solvent, and energy, usually ultrasonic energy, is introduced into the system. Studies have shown that h-BN disperses reasonably well in isopropyl alcohol (IPA),[12] *N,N*-dimethylformamide (DMF),[3,4] dimethyl sulfoxide (DMSO),[4,9] and *N*-methylpyrrolidone (NMP).[1,13–15] However, many of these solvents are harmful and/or dangerous to work with. There have also been a few studies describing the exfoliation of h-BN using water as a solvent. Connell *et al.* recently showed that water serves a critical role in h-BN exfoliation, hydrolyzing planar defects to introduce hydroxyl groups that help to stabilize the suspended BNNS.[16]

Here we describe a refined method of producing BNNS from bulk h-BN powders using a simple co-solvent approach. This system combines common organic solvents with water to create a mixture that exfoliates and suspends h-BN much more efficiently than the individual components. In this way, we reap the benefits of two solvent types that have each been shown to successfully exfoliate h-BN on their own. This co-solvent system is inexpensive, safe to work with, and completely scalable. Although a single co-solvent system (IPA in water) has been reported,[12] by studying the trends associated with different co-solvent combinations we have developed a much more comprehensive understanding of their effects on h-BN suspension and exfoliation. This understanding has led us to discover an optimized co-solvent system for producing and suspending BNNS. Recent literature reports have suggested that there exists a small window of surface tension values for which co-solvent exfoliation is optimal.[2,9,17,18] Here we discuss the roles of solvent surface tension and molecular weight (M.W.) in the exfoliation of h-BN, and propose a mechanism for co-solvent exfoliation.

2.2 Materials and methods

Hexagonal boron nitride (h-BN) was supplied by Momentive Performance Materials, Inc. Two grades were used: NX1, with an average particle size of 1 μm, and PT100, with an average particle size of 13 μm. NX1 was used initially for the UV-vis studies as a model material, and TEM images were taken using exfoliated

PT100. Acetone, methanol, ethanol, 1-propanol, 2-propanol, and *tert*-butanol were obtained from Sigma-Aldrich, and all were of ≥ 99.5% purity (as purchased).

All co-solvent mixtures were prepared prior to the addition of h-BN. All calculations and preparations were done volumetrically with deionized water, and solvents were stored in bottles sealed with parafilm to minimize changes in concentration. A B2500A-DTH bath sonicator (VWR) operating at 42 kHz was used for all exfoliations. 10 mg of h-BN and 5 mL of co-solvent mixture, at the desired concentration, were added to a 3 dram vial. The vial was tightly capped and parafilmed to maintain the integrity of the solution during the sonication process. The vials were sonicated for 3 hours and rotated randomly around the space of the sonicator every 30 minutes to correct for any variations within the apparatus. This procedure was carried out for each solvent, 0 to 100% concentrations at 10% intervals. The mixtures reached temperatures of 45 °C during the course of sonication. The resulting mixture was allowed to cool and was subsequently centrifuged using an Allegra X-15R centrifuge (Beckman Coulter) for 20 minutes at 3200 rpm, and the resulting supernatant was carefully extracted for further characterization.

2.3 Characterization

UV-vis absorbance measurements were made using a UV-3101PC UV- VIS-NIR scanning spectrophotometer (Shimadzu). The supernatant samples were pipetted into a quartz cuvette (path length 1 cm, Starna Cells, Inc.) and quickly

capped. The samples were analyzed within 2 days of the initial sonication. All samples were analyzed from 700-300 nm, but the absorbance at 400 nm was used for measuring the relative amount of exfoliation for each co-solvent.

Transmission electron microscopy (TEM) micrographs and diffraction patterns were recorded using a Titan S/TEM (FEI) operating at 300 keV. TEM samples were prepared by placing a 400-mesh lacey formvar/carbon copper grid (Ted Pella, Inc.) onto a piece of qualitative filter paper (Whatman "4", seen in **Figure 2.1**). The supernatant sample of interest was then diluted ~1:10 in water, shaken, and a few drops were added via a Pasteur pipet. The filter paper is necessary to help wick away the solvent as fast as possible. This helps to avoid restacking of the BNNS, ensuring an accurate representation of BNNS found in the co-solvent system.

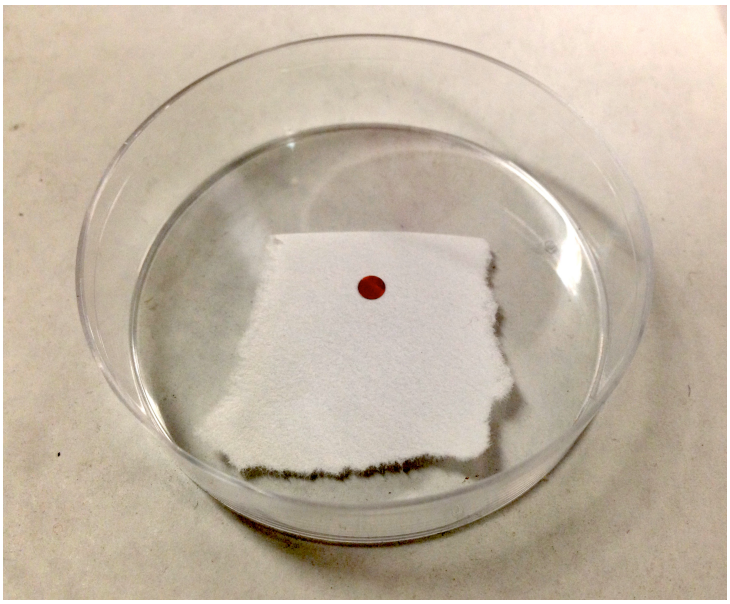

Figure 2.1. Preparation of TEM samples. The lacey formvar/carbon copper grid (400 mesh) is prepared on top of a piece of filter paper. This helps to quickly wick away the solvent from the exfoliated BNNS.

2.4 Results and discussion

Figure 2.2 shows the UV-vis data collected for the different co-solvent mixtures. Because h-BN does not exhibit any prominent absorption peaks, a wavelength of 400 nm was used to compare the relative absorbance between samples.[12] All data are the averaged results of five trials for each co-solvent system. The surface tension of pure water (0 w/w% solvent) at standard conditions is 72.0 mJ m^{-2}; this value decreases relative to which solvent is mixed in and at what concentration.[19,20]

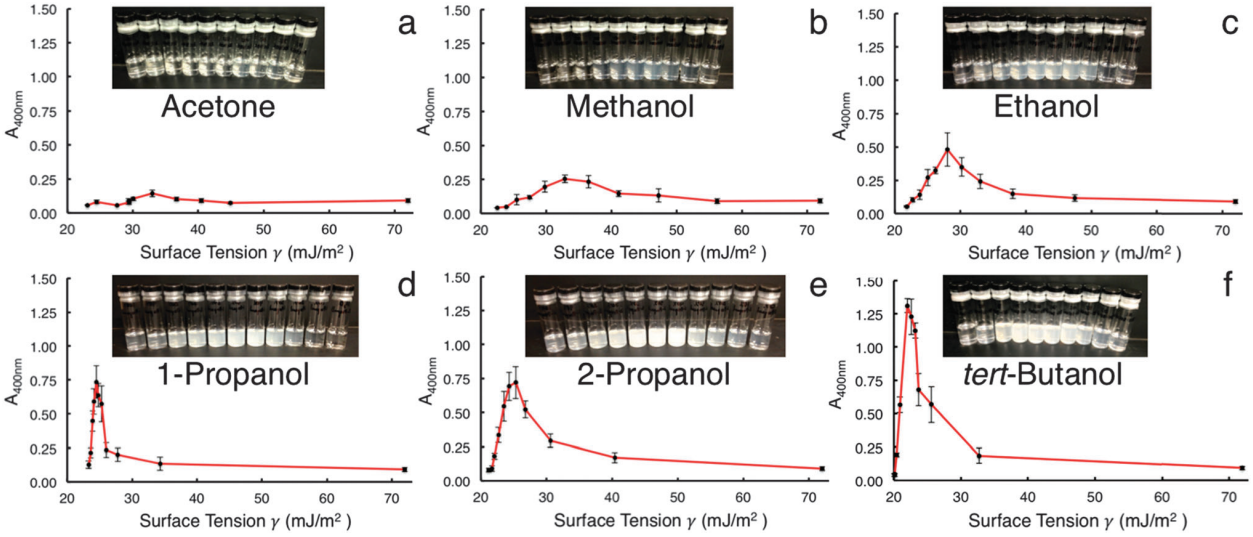

Figure 2.2. UV-vis data for BNNS in different co-solvent systems. Absorbance values were recorded at 400 nm; all data were averaged over five trials. From left to right, both the vials and the data points represent 100, 90, 80, 70, 60, 50, 40, 30, 20, 10, and 0 w/w% solvent in water. There are 11 vials present for both 1-prop (d) and IPA (e) to include 0 w/w% solvent (pure water), which can be seen as the rightmost vial in each photo.

This is represented on the x-axis in Figure 2.2a–f: the surface tension increases from left to right corresponding to an increase in solvent w/w%. While other studies have shown evidence for both pure water[16] and pure solvent[9] successfully

exfoliating h-BN, it is clear that a mixture of solvent and water trumps the results of the two liquids by themselves. The UV-vis data indicate that 60 w/w% *t*BA is superior at dispersing and retaining h-BN, with IPA and 1-prop being second best (Figure 2.2f, e, and d, respectively). Co-solvent mixtures were stable after 2 months of sitting on the lab bench. Maximum absorbance (A_{max}) values for each solvent occur around 40–60 w/w% and increase in the following order: acetone < MeOH < EtOH < 1-prop < IPA < *t*BA. These data parallel results from other studies involving other inorganic graphene analogues.[2,12]

It is interesting to note that the increase in absorbance is directly proportional to increasing M.W. Figure 2.3 illustrates this relationship for the solvents with similar chemical structure, *t*BA having the highest M.W. (74.12 g mol^{-1}) and MeOH having the lowest (32.04 g mol^{-1}). These data also agree with previous studies involving other inorganic layered materials.[2,12] Perhaps more revealing is the relationship between M.W. and surface tension at the A_{max} for each solvent. As M.W. increases linearly with absorbance, the matching surface tension decreases. Thus, the relationship of surface tension is inversely proportional to both increasing M.W. and increasing A_{max}. Moreover, the range of surface tensions involved in A_{max} for each solvent is much wider than what the literature values suggest,[2,9,17,18] with the maximums for *t*BA, IPA, 1-prop, EtOH, and MeOH corresponding to 21.3, 24.5, 25.3, 28, and 32.9 mJ m^{-2}, respectively (Table 2.1). These values represent a difference of approximately 11.5 mJ m^{-2}.

Surface tension in mN/m for various aqueous mixtures of common solvents at 25°C

Mass %	Acetone	Methanol	Ethanol	1-propanol	2-propanol	*tert*-butanol
0%	72.0	72.0	72.0	72.0	72.0	72.0
10%	44.9	56.2	47.5	34.3	40.4	32.7
20%	40.5	47.2	38.0	27.8	30.6	25.6
30%	36.7	41.1	33.0	26.0	26.8	23.7
40%	33.0	36.5	30.2	25.3	25.3	23.2
50%	30.1	32.9	28.0	24.8	24.3	22.6
60%	29.4	29.8	26.2	24.5	23.5	22.0
70%	29.4	27.5	25.0	24.1	22.7	20.9
80%	27.6	25.5	23.8	23.9	22.1	20.4
90%	24.5	23.9	22.7	23.6	21.7	20.1
100%	23.1	22.5	21.8	23.3	21.2	20.1

Table 2.1. Surface tension values of common aqueous mixture at 25 °C as obtained from the *Handbook of Chemistry and Physics*, CRC Press, 2003, 84th edition. Data for *tert*-butanol comes from Gliński *et al.*, *J. Chem. Phys.*, 1995, 102, 1361. Note: 1 mN/m = 1 mJ/m^2.

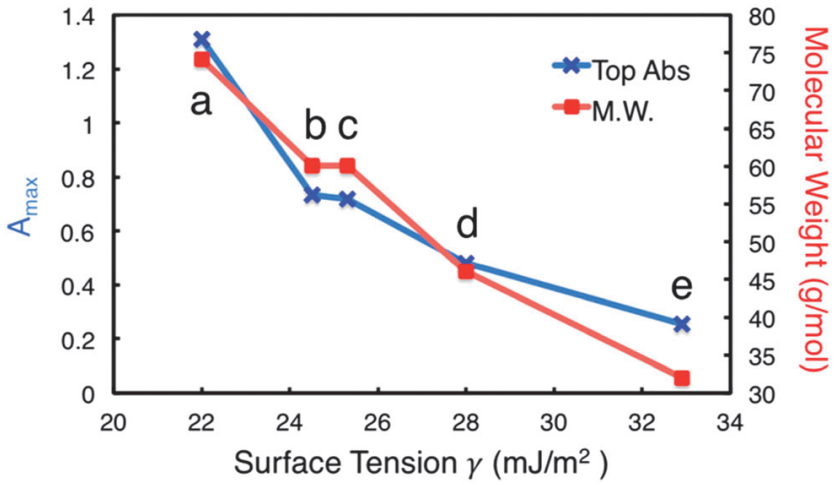

Figure 2.3. Comparison of the maximum absorbance (A_{max}) and molecular weight (M.W.) with respect to surface tension for solvents with like chemistries. Each vertically aligned pair of data points represent: (a) *t*BA, (b) IPA, (c) 1-prop, (d) EtOH, and (e) MeOH.

Obviously surface tension is not the only factor at play in the exfoliation of h-BN, as M.W. appears to have a great impact, even if the surface tension changes drastically. This may support the importance of considering the Lennard-Jones potential between the surface of h-BN and the co-solvent system, suggesting that larger solvent molecules serve to stabilize the individually dispersed sheets more effectively than smaller solvent molecules.[2] This is likely due to the larger molecules' ability to sterically separate the nanosheets, preventing their recombination in suspension.

Also notable is the effect chemical structure plays on liquid exfoliation. 1-prop and IPA result in essentially identical BNNS dispersions, despite being isomers of each other. This raises questions on the potential effect other less common solvents could have on h-BN exfoliation, specifically isomers.

Furthermore, acetone performed the worst of all the solvents, despite having a higher M.W. (58.08 g mol^{-1}) than both MeOH and EtOH, likely due to the absence of a hydroxyl group to stabilize the BNNS in the presence of water. Future studies will further probe the relationship between surface tension, M.W., and structural dependencies in the exfoliation of h-BN.

Figure 2.4 shows TEM images of BNNS after sonication. TEM is ideal for successful analysis of BNNS, as the nature of sample preparation allows for the resolution of atomically thin layers of material while avoiding restacking of the sheets (Figure 2.1). Figure 2.4b (inset of Figure 2.4a) reveals the thickness of a few-layered BNNS to be approximately 7–9 nm, which corresponds to roughly 14–

19 atomic layers. This agrees with a semi-quantitative assessment of BNNS thickness through TEM analyses, which suggests an average thickness range of 6–10 nm for exfoliated BNNS. Figure 2.4c illustrates the scrolling effect seen in BNNS, a result of sonication and the presence of extremely thin sheets.[15] The authors have experienced this same phenomenon before with few-layer graphene.[21] Figure 2.4c also shows the plethora of single- and few-layered sheets present on the TEM sample. Figure 2.4d shows a diffraction pattern for a few-layered BNNS.[10,14,22,23] Figure 2.5 also shows partial exfoliation of h-BN, an intermediate step to successful exfoliation.

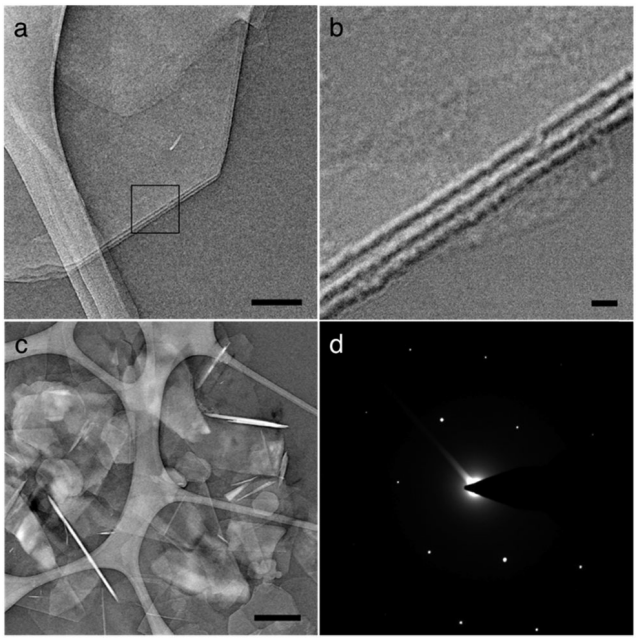

Figure 2.4. TEM micrographs of BNNS after sonication for 3 h in 60% *t*BA. (a) A few-layered BNNS sample. A carbon support can be seen through the exfoliated sheet. (b) The magnified image of the square outline from (a). (c) Evidence for scrolling of the BNNS. The bright white ''lines'' are where the sheets have scrolled. (d) Diffraction pattern of a few-layered BNNS. Scale bars represent (a) 100 nm, (b) 10 nm, and (c) 0.5 mm.

Figure 2.5. TEM micrograph of a partially exfoliated BNNS. The two sheets share similar shapes. Scale bar is 200 nm.

2.5 Conclusion

In conclusion, we have implemented a co-solvent approach to exfoliate and suspend h-BN into BNNS. This method is completely scalable, inexpensive, and extremely safe to handle. We have found that a 60 w/w% mixture of *t*BA in water is most effective at creating a stable suspension of BNNS, with TEM confirming exfoliation into few-layered sheets. This is in` contrast to studies that suggest pure water or pure solvent is effective at exfoliating h-BN. We have shown that A_{max} and M.W. are inversely proportional to co-solvent surface tension, and that the range of surface tension values corresponding to A_{max} is approximately 11.5 mJ m^{-2}, a much broader spread than what is suggested in the literature. The critical factor for choosing a solvent system to exfoliate h-BN is not solely surface

tension; rather, it should be a combinatory consideration of surface tension, M.W., and chemical structure. This lends itself to the importance of phenomena such as the Lennard-Jones potential in the exfoliation of layered materials. The authors are currently pursuing the use of more exotic solvents in the exfoliation and suspension of h-BN in order to further clarify the roles of M.W. and chemical structure.

2.6 Acknowledgments

The authors would like to thank Momentive Performance Materials, Inc. for providing the boron nitride powders and Dr. Anand Muragaiah and Dr. Hao Qu for many helpful discussions.

References

(1) Nicolosi, V.; Chhowalla, M.; Kanatzidis, M. G.; Strano, M. S.; Coleman, J. N. Liquid exfoliation of layered materials. *Science* **2013**, 340, 1226419.

(2) Halim, U.; Zheng, C. R.; Chen, Y.; Lin, Z.; Jiang, S.; Cheng, R.; Huang, Y.; Duan, X. A rational design of cosolvent exfoliation of layered materials by directly probing liquid-solid interaction. *Nat. Commun.* **2013**, 4, 2213.

(3) Zhi, C.; Bando, Y.; Tang, C.; Kuwahara, H.; Golberg, D. Large-scale fabrication of boron nitride nanosheets and their utilization in polymeric composites with improved thermal and mechanical properties. *Adv. Mater.* **2009**, 21, 2889–2893.

(4) Lian, G.; Zhang, X.; Tan, M.; Zhang, S.; Cui, D.; Wang, Q. Facile synthesis of 3D boron nitride nanoflowers composed of vertically aligned nanoflakes and fabrication of graphene-like BN by exfoliation. *J. Mater. Chem.* **2011**, 21, 9201.

(5) Hod, O. Graphite and hexagonal boron-nitride have the same interlayer distance. Why? *J. Chem. Theory Comput.* **2012**, 8, 1360–1369.

(6) Kim, G.; Jang, A.-R.; Jeong, H. Y.; Lee, Z.; Kang, D.J.; Shin, H.S. Growth of high-crystalline, single-layer hexagonal boron nitride on recyclable platinum foil. *Nano Lett.* **2013**, 13, 1834–1839.

(7) Kim, K. K.; Hsu, A.; Jia, X.; Kim, S. M.; Shi, Y.; Hofmann, M.; Nezich, d.; Rodriguez-Nieva, J. F.; Dresselhaus, M.; Palacios, T.; Kong, J. Synthesis of monolayer hexagonal boron nitride on Cu foil using chemical vapor deposition. *Nano Lett.* **2012**, 12, 161–166.

(8) Seth, M.; Hatzikiriakos, S. G.; Clere, T. M. Gross melt fracture elimination: The role of surface energy of boron nitride powders. *Polym. Eng. Sci.* **2002**, 42, 743–752.

(9) Coleman, J. N.; Lotya, M.; O'Neill, A.; Bergin, S. D.; King, P. J.; Khan, U.; Young, K.; Gaucher, A.; De, S.; Smith, R. J.; Shvets, I. V.; Arora, S. K.; Stanton, G.; Kim, H.-Y.; Lee, K.; Kim, G. T.; Duesberg, G. S.; Hallam, T.; Boland, J. J.; Wang, J. J.; Donegan, J. F.; Grunlan, J. C.; Moriarty, G.; Shmeliov, A.; Nicholls, R. J.; Perkins, J. M.; Grieveson, E. M.; Theuwissen, K.; McComb, D. W.; Nellist, P. D.; Nicolosi, V. Two-dimensional nanosheets produced by liquid exfoliation of layered materials. *Science* **2011**, 331, 568–571.

(10) Shi, Y.; Hamsen, C.; Jia, X.; Kim, K. K.; Reina, A.; Hofmann, M.; Hsu, A. L.; Zhang, K.; Li, H.; Juang, Z.-Y.; Dresselhaus, M. S.; Li, L.-J.; Kong, J. Synthesis of few-layer hexagonal boron nitride thin film by chemical vapor deposition. *Nano Lett.* **2010**, 10, 4134–4139.

(11) Sinitskii, A.; Erickson, K. J.; Lu, W.; Gibb, A. L.; Zhi, C.; Bando, Y.; Goldberg, D.; Zettl, A.; Tour, J. M. High-yield synthesis of boron nitride nanoribbons via longitudinal splitting of boron nitride nanotubes by potassium vapor. *ACS Nano* **2014**, 8, 9867–9873.

(12) Zhou, K.-G.; Mao, N.-N.; Wang, H.-X.; Peng, Y.; Zhang, H.-L. A mixed-solvent strategy for efficient exfoliation of inorganic graphene analogues. *Angew. Chem., Int. Ed.* **2011**, 50, 10839–10842.

(13) Hughes, J. M.; Aherne, D.; Coleman, J. N. Generalizing solubility parameter theory to apply to one- and two-dimensional solutes and to incorporate dipolar interactions. *J. Appl. Polym. Sci.* **2013**, 127, 4483–4491.

(14) Chen, X.; Dobson, J. F.; Raston, C. L. Vortex fluidic exfoliation of graphite and boron nitride. *Chem. Commun.* **2012**, 48, 3703–3705.

(15) Chen, X.; Boulos, R. A.; Dobson, J. F.; Raston, C. L. Shear induced formation of carbon and boron nitride nano-scrolls. *Nanoscale* **2013**, 5, 498–502.

(16) Lin, Y.; Williams, T. V.; Xu, T.-B.; Cao, W.; Elsayed-Ali, H. E.; Connell, J. W. Aqueous dispersions of few-layered and monolayered hexagonal boron nitride nanosheets from sonication-assisted hydrolysis: critical role of water. *J. Phys. Chem. C* **2011**, 115, 2679–2685.

(17) Hernandez, Y.; Nicolosi, V.; Lotya, M.; Blighe, F. M.; Sun, Z.; De, S.; McGovern, I. T.; Holland, B.; Byrne, M.; Gun'Ko, Y. K.; Boland, J. J.; Niraj, P.; Duesberg, G.; Krishnamurthy, S.; Goodhue, R.; Hutchison, J.; Scardaci, V.; Ferrari, A. C.; Coleman, J. N. High-yield production of graphene by liquid-phase exfoliation of graphite. *Nat. Nanotechnol.* **2008**, 3, 563–568.

(18) Cao, L.; Emami, S.; Lafdi, K. Large-scale exfoliation of hexagonal boron nitride nanosheets in liquid phase. *Mater. Express* **2014**, 4, 165–171.

(19) Handbook of Chemistry and Physics, CRC Press, 84th edn, **2003**, pp. 6–186.

(20) Glin´ski, J.; Chavepeyer, G.; Platten, J.-K. Surface properties of diluted aqueous solutions of 1,2-pentanediol. *J. Chem. Phys.* **1995**, 102, 2113.

(21) Viculis, L. M.; Mack, J. J.; Kaner, R. B. A chemical route to carbon nanoscrolls. *Science* **2003**, 299, 1361.

(22) Du, M.; Li, X.; Wang, A.; Wu, Y.; Hao, X.; Zhao, M. One-step exfoliation and fluorination of boron nitride nanosheets and a study of their magnetic properties. *Angew. Chem., Int. Ed.* **2014**, 53, 3645–3649.

(23) Odlyzko, M. L.; Mkhoyan, K. A. Identifying hexagonal boron nitride monolayers by transmission electron microscopy. *Microsc. Microanal.* **2012**, 18, 558–567.

CHAPTER 3

Flash Converted Graphene for

Ultra-High Power Supercapacitors

3.1 Background

Electric double-layer capacitors (EDLCs), a type of supercapacitor, are energy storage devices that can be charged and/or discharged within seconds, provide high power, and operate under much higher currents than can be withstood by batteries. Carbon-based supercapacitors are currently a $1 billion industry which is projected to grow to more than $3 billion within five years because of the demands for advanced consumer products[1–3] that require fast storing and retrieval of energy. These technologies include vehicle ignition, pitch control in wind turbines, cold starting of trucks, load leveling from renewable energy sources, and space exploration applications.[4–7] Regarding the latter, high specific power (by mass) is required for satellites and space station operations.[8–12] Thus, EDLCs have favorable charge–discharge properties, providing high power and the ability to operate at high rates suitable for these advanced applications.

Traditional methods used to produce supercapacitor electrodes involve mixing a carbon source, such as activated carbon, with an insulating binder that is cast onto a current collector.[4,13,14] The carbon materials used in these traditional methods generally exhibit low conductivity, especially when compared to graphene. The conductivity of chemically converted graphene (CCG) is ≈7200 S m^{-1} (close to that of pristine graphite),[15,16] while the conductivity of activated carbon is only 10–100 S m^{-1}.[17] Graphene is composed of planar sheets of sp^2 hybridized carbon atoms containing large networks of delocalized π-electrons resulting in very high conductivity.[18] When used in supercapacitor electrodes,

graphene's planar structure gives rise to fast charging and discharging because the electrolyte ions can readily access the large surface areas of the sheets.[7,19] The efficient transport of ions between the electrolyte and graphene surfaces is advantageous for high power and rate capabilities and rapid response times. However, processing graphene can be problematic. The planar aromatic sheets often restack due to favorable π–π interactions between adjacent sheets.[20,21] Upon restacking, the graphene is converted back into a graphite-like material and no longer possesses the high surface area of single layer graphene, reducing the material's high power and rate capabilities.[22]

Well-known methods for producing graphene include chemical conversion from graphene oxide,[15,23,24] intercalation and exfoliation of graphite,[14,25,26] thermal conversion of graphene oxide,[27] and electrochemical reduction of graphene oxide.[28] These methods yield robust graphene, but as mentioned above, the sheets readily restack leading to dense packing and loss of surface area.[22] Our group has recently developed a method for the preparation of a graphene-based material via the photo-thermal reduction of graphene oxide using the flash from a camera. The result of the reduction is a low density, 3D graphene architecture that is ideal as an electrode material.[29] Figure 3.1 shows images of chemically converted graphene and flash converted graphene (FCG) for comparison.

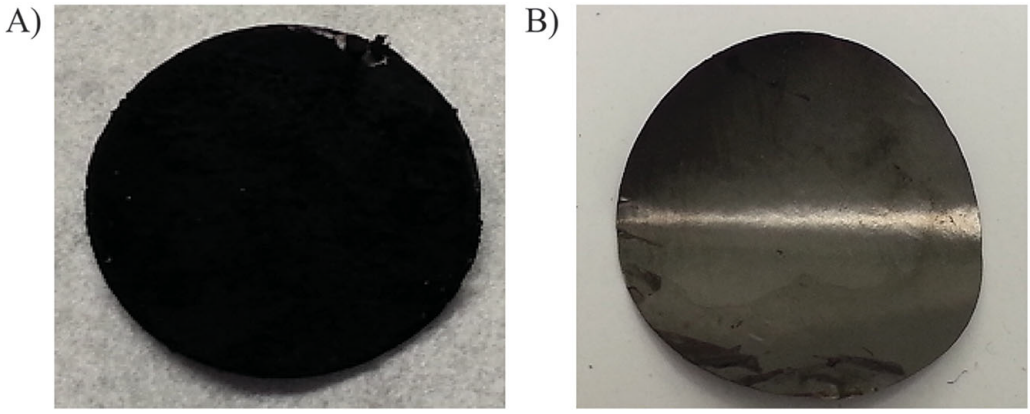

Figure 3.1. Graphene electrodes: A) A smooth chemically converted graphene membrane. B) A rougher, expanded graphene membrane made by photothermal conversion of graphene oxide.

Photo-thermal conversion creates a disordered corrugated graphene structure in which adjacent sheets are no longer oriented parallel to each other. The photo-thermal conversion can be accomplished with different light sources, e.g., using a LightScribe with a 780 nm laser[30] or using a flash lamp.[29] The latter method, known as flash converted graphene is comparable to other forms of reduced graphene oxide due to residual oxygen. FCG offers a method to produce graphene from graphene oxide that minimizes restacking of sheets.

In electric double-layer capacitors, the electrode must soak in the electrolyte solution to allow diffusion of ions to the available surfaces of the electrode. When applying a charging or discharging current, the ions travel atomic distances to/from the electrode surfaces thereby creating/dispensing capacitance.[31,32] A 3D corrugated foam structure is advantageous because it maximizes the exposed surfaces.[33–36] Therefore, FCG can be an ideal material for EDLCs (Scheme 3.1).

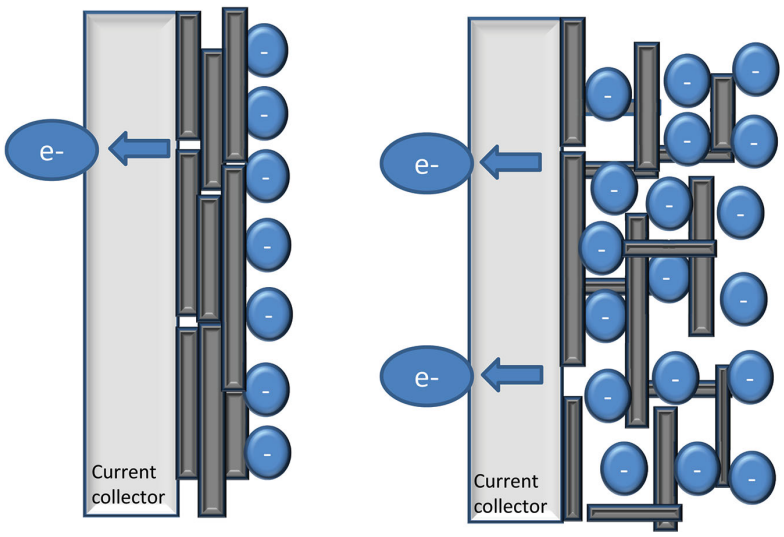

Scheme 3.1. Schematic diagram of ions from the electrolyte absorbing onto the accessible surfaces of the electrode active material. A) Ion adsorption occurs only at the surface of the electrode film because of its densely-packed morphology. B) Ion adsorption occurs throughout the electrode active material because of its less dense corrugated 3D morphology.

Here, we demonstrate the use of FCG as an electrode material in graphene-based supercapacitors. A commercially available flash lamp is used to produce FCG, which is processed into binder-free coin cell supercapacitors. Two protocols for fabricating the FCG electrodes are reported. In the first method, bulk graphene oxide (GO) is first converted to FCG (pre-FCG), then cast onto a current collector. For the second method, the graphene oxide solution is first cast onto the current collector, then converted to FCG (post-FCG) (Scheme 3.2).

Both methods produce supercapacitors that exhibit exceptional specific power, response time, and rate capability. The FCG supercapacitors possess many properties superior to other EDLCs. The specific power and rate capabilities of pre-FCG and post-FCG are among the highest reported for graphene-based supercapacitors. Furthermore, the specific power of the FCG

devices is ten times higher than that of carbon-based commercial supercapacitors.

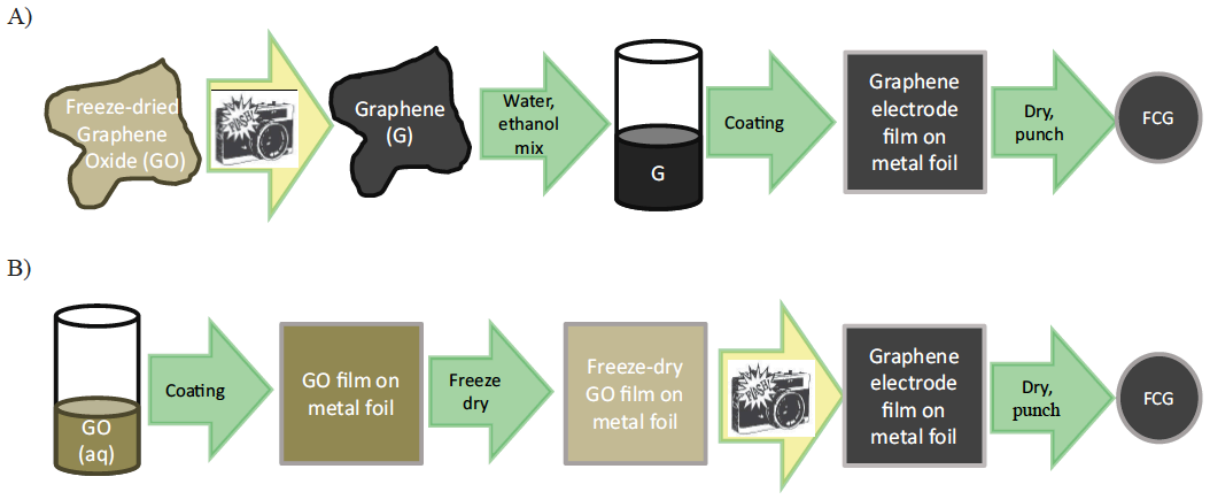

Scheme 3.2. The two methods for making FCG electrodes: A) Pre-coated flash conversion (pre-FCG) and B) Post-coated flash conversion (post-FCG).

3.2 Experimental methods and characterization

3.2.1 Preparation and fabrication of pre-FCG electrodes

The precursor to FCG, graphene oxide, was prepared from natural flake graphite using a modified Hummer's method.[15,45,46] Graphene oxide in an aqueous dispersion (2.6% wt) was freeze-dried using a Labconco Freezone 1L freeze-dry system with the lyophilizer vacuum set at 0.020 torr at a temperature of –51°C. The freeze-dried graphene oxide was transferred to 20 mL scintillation vials (15 mg in each vial) with caps slightly loose. A flash lamp (Alien Bees B1600) was used at full power (640 J) to reduce the graphene oxide and convert it into flash reduced graphene. Each vial was flashed ten times to ensure that all GO was

converted to graphene. 100 mg of FCG was transferred into a new vial. 5 mL of deionized water and 5 mL of ethanol were added to the FCG. The contents were stirred for 30 min on a stir plate and bath sonicated for 99 min at room temperature. Each vial was placed in a vacuum oven at 60 °C for 20 min to remove some solvent and increase the viscosity of the dispersion. The dispersion was then sonicated for 1 min just before casting. A sheet of carbon-coated aluminum current collector was placed onto the Gardco automatic drawdown machine II with vacuum to keep the fi lm as flat as possible. 2 mL of the dispersion was transferred to the current collector and was cast at a blade height of 254 μm. The cast film was then transferred to an oven and dried at 40 °C overnight.

3.2.2 Preparation and fabrication of post-FCG electrodes

The starting material, graphene oxide, was prepared in the same way as that used in pre-FCG[15,45,46] and cast onto carbon-coated aluminum foil current collectors using a Gardco automatic drawdown machine II at 610 μm. The cast GO film was immediately placed into a liquid nitrogen bath and frozen before being loaded into the lyophilizer (Labconco Freezone 1L Freeze dry systems). After the film was freeze-dried overnight (0.018 torr and –51 °C), it was exposed to a flash lamp (Alien Bees B1600) at a flash power of 160 J. The light brown colored GO foam turned darker incrementally, becoming completely black after three flashes.

3.2.3 Morphology, composition, and properties

Conductivity of FCG was determined after pressing FCG powder into a pellet with a Carver Press set at 1000 lbs for 10 min, by making a two-point probe measurement using a voltmeter. Several equidistant squares were painted onto the surface of the pellet using silver paint to provide improved contact with lower resistance to the voltmeter probes. The length, width, and height (thickness) between the two squares were measured and conductivity was determined using Equation (3.1)

$$\sigma = \frac{length}{R\ x\ width\ x\ height} \tag{3.1}$$

where R = measured sheet resistance in Ω and σ = conductivity (S m^{-1} or Ω^{-1} m^{-1}).

Nitrogen BET surface area measurements were taken on a Micromeritics Instrument Corporation TriStar II 3020 V1.03 (V1.03) at 77.3 K. X-ray diffraction (XRD) patterns were collected on a Bruker D8 Discover Powder X-ray Diffractometer using CuKα radiation (λ = 1.5406 Å). The 3D morphology of pre-FCG and post-FCG shown from the SEM images was taken on an FEI Nova 230 Nano SEM. X-ray photoelectron spectroscopy (XPS) studies were carried out on a Kratos AXIS Ultra DLD with a monochromatic Al Kα X-ray source operating at 10 mA and 15 kV. Survey spectra and individual high-resolution spectra were collected using pass energies of 160 and 20 eV, respectively. Data processing was

performed using CasaXPS 2.3 software, and spectral binding energies were calibrated by assigning the hydrocarbon peak in the C 1s high-resolution spectra to 284.6 eV. GC-MS experiments were carried out on an Agilent 6890-5975 GC-MS using helium as a carrier gas and argon as the control. Freeze-dried GO was sealed in a vial with a septum cap under an argon atmosphere in a glove box. The freeze-dried GO was then converted to FCG via flashing and 1 mL of the air surrounding the FCG in the vial was extracted with a syringe and injected into the GC-MS (G3174A) for analysis.

3.2.4 Assembly of FCG electrodes into coin cell supercapacitor devices

For both methods, the process to assemble FCG electrodes into CR2032 coin cell devices was the same. 15 mm diameter discs were punched from the electrodes using a 15 mm diameter round hole arch punch (McMaster-Carr). These discs serve as the electrodes in the coin cell supercapacitor. Each electrode was weighed using a microbalance, and the thicknesses were measured using a micrometer. The assembly of the coin cell (CR2032) device was made by starting with the bottom cap and gasket, then adding the electrodes, the polypropylene separator (17 mm diameter), the electrolyte (1.0 M tetraethylammonium tetrafluoroborate ($TEABF_4$) in acetonitrile), then adding the spacer, spring, and the top cap. Finally, the stack was crimped shut. Devices were made in both air and in a nitrogen filled glove bag. There was no noticeable difference in the results of the cells made in air versus those made under nitrogen. The time it

takes to build a device, from inserting electrolyte to sealing the cell is only about 20 s. The mass loadings of pre-FCG and post-FCG electrodes are 0.35 and 0.49 mg cm^{-2}.

3.2.5 Calculations

The capacitances were calculated from data from cyclic voltammetry and constant current measurements using a potentiostat (Biologic VMP3) with a 10 Amp booster (VMP3b-10). The equation for capacitance calculations is

$$C = \frac{i\Delta t}{\Delta V} \tag{3.2}$$

where C = capacitance (F); i = current (A); Δt = discharge time; ΔV = discharge voltage; and $\frac{\Delta V}{\Delta t}$ = scan rate in cyclic voltammetry.

The resulting capacitance value can then be divided by weight to give gravimetric capacitance. The capacitance based on FCG for an electrode (F $g^{-1}_{FCG/electrode}$ or F $cm^{-3}_{FCG/electrode}$) is calculated by multiplying the capacitance from Equation (3.2) by a factor of four. The factor of four compensates for the 50% decrease in mass or volume going from a single device to per electrode, and the circuit translation from a device (two electrodes in series) to per electrode (not in series) is

$$C_s = \frac{c}{m} \tag{3.3}$$

where C_s = specific capacitance (F g^{-1}) and m = mass of active material (g).

The specific energy is then calculated as

$$E = \left(\frac{1}{2}\right) C_s \Delta V^2 \tag{3.4}$$

where ΔV = voltage window.

The specific power can also be calculated from constant current data, by using the IR drop value

$$Specific\ power = \frac{(\Delta V)^2}{4mESR} \tag{3.5}$$

where ΔV = operating voltage; m = mass of active material (g); and ESR = equivalence series resistance (Ω).

For the rate capability, the current values were calculated by multiplying the weight by the desired current density (A g^{-1}), i.e. 5, 10, and 20 A g^{-1}. After

collecting the data, and calculating the capacitances, the relative capacitance was obtained by dividing each capacitance by the capacitance measured at 1 A g^{-1}. A plot was then made to illustrate the trend. The current density at which the device can retain 50% of capacitance and where the device reaches <1% of capacitance can be readily obtained from these results.

3.2.6 Electrochemical measurements

Electrochemical properties and results were determined using a Biologic VMP3 potentiostat and a VMP3b-10 10 Amp booster. The devices were measured with a four-point holder for coin cells. CV and CC were obtained from 0 to 2 V. The stable voltage window (2 V) was determined through CV at 100 mV s^{-1} at different voltages (Figure 3.2). EIS was also taken on the Biologic VMP3 over a frequency range from 1 MHz to 10 mHz at open circuit potential. The cycle life stability was investigated by using constant current charge–discharge from 0 to 2 V at 1 A g^{-1} for 5000 cycles.

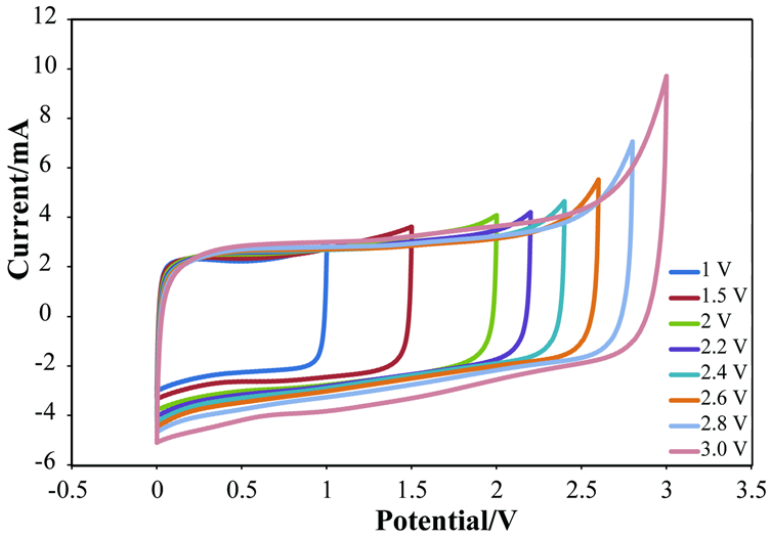

Figure 3.2. Cyclic voltammetry of FCG devices cycled at 100 mV/s from 1.0 V up to 3.0 V to determine the stable operating voltage. Based on these curves, an operating voltage of 2.0 V was selected.

3.3 Results and discussion

Based on the mechanism of electric double-layer capacitors, surface area is a crucial factor in determining the energy storage capabilities. Since EDLC supercapacitors store charge through the electric double layer of ions formed on the exposed surfaces of the electrode active material, a larger active material surface will, therefore, store more charge.[13,31] Graphene converted from a flash lamp (FCG) has a desirable increased surface area relative to many other forms of graphene materials. The combined effects of freeze-drying and flashing graphene oxide produce a low-density, high surface area material with a porous network of graphene sheets. Freeze-drying the aqueous dispersion of graphene oxide acts to preset the density of the cast material, essentially immobilizing the graphene oxide molecular configuration as it exists as a dispersion. As an

aqueous colloid, the graphene oxide interacts with water molecules forming hydrogen bonds and aggregates to create a low-density morphology.

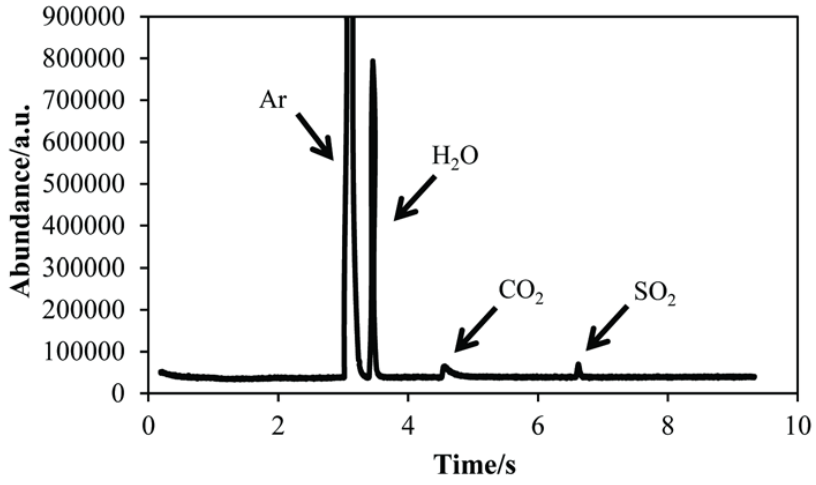

Figure 3.3. GC-MS spectra of gas after flashing freeze-dried GO in a sealed vial filled with argon.

Upon flashing, the reduced, freeze-dried graphene oxide decreases in mass by 55% and is slightly expanded in morphology. This expansion can be attributed to the conversion of the oxygen functional groups on graphene oxide from C–OH, C=O, C–O–C, and –COOH into gaseous CO_2, and H_2O, along with some residual SO_2 from the synthesis. The presence of CO_2, H_2O, and residual SO_2 gases was confirmed by gas chromatography– mass spectrometry (GC-MS) with H_2O at 18.1 *m/z* the most abundant, followed by CO_2 at 44 *m/z*, and SO_2 at 63.9 *m/z* (Figure 3.3). Thus, the expansion of FCG and creation of a 3D porous network is related to the emission of CO_2, H_2O, and SO_2 gases from the graphene oxide sheets.

Scanning electron microscope (SEM) images of the FCG electrode films from each coating method show a highly porous 3D morphology (Figure 3.4). A

comparison to dried unreduced nonporous GO film (Figure 3.5) further supports the porous structure of the FCG material. The post-FCG electrode exhibits a corrugated cardboard-like structure with interconnected structures in fractal-like geometry. The post-FCG electrode has an even greater degree of 3D corrugated morphology because the graphene is converted on the current collector after casting, whereas pre-FCG is converted before casting and dispersed in a solvent prior to casting. The dispersion in solvent may facilitate some restacking of the sheets. The 3D morphology of FCG enables a small diffusion barrier allowing electrolyte ions to readily access the surfaces of FCG.

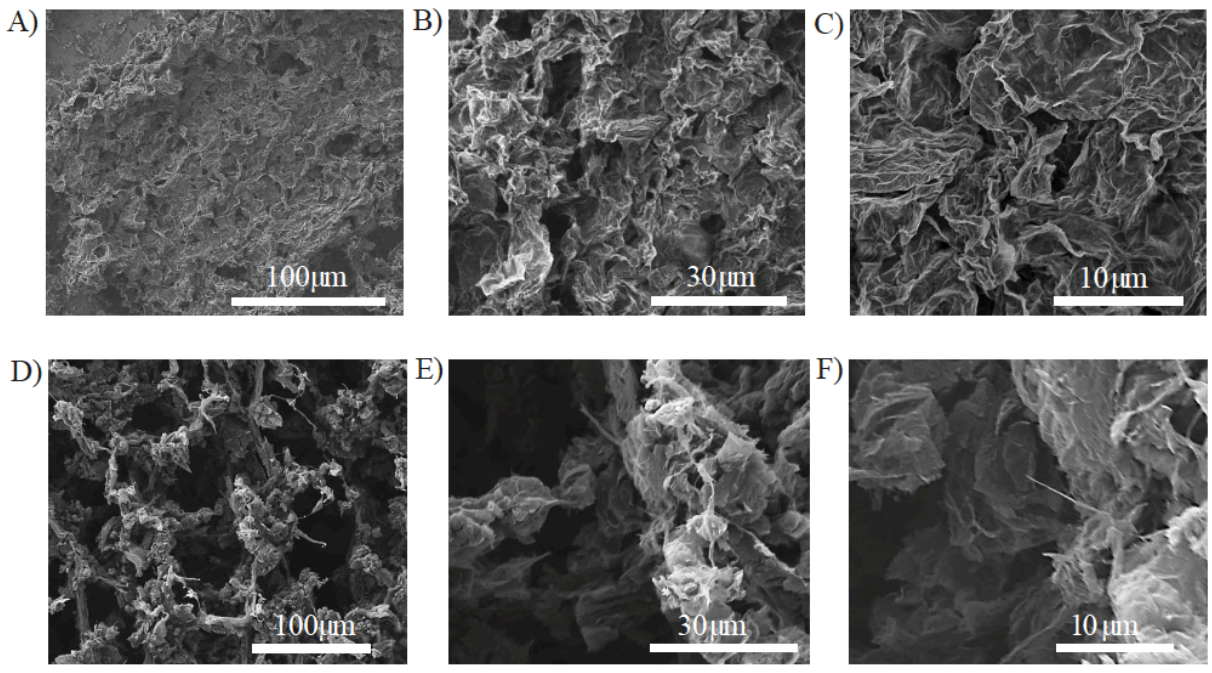

Figure 3.4. SEM images of A–C) pre-FCG, D–F) post-FCG at 0.5k, 2k, and 5k magnification showing the corrugated porous morphology.

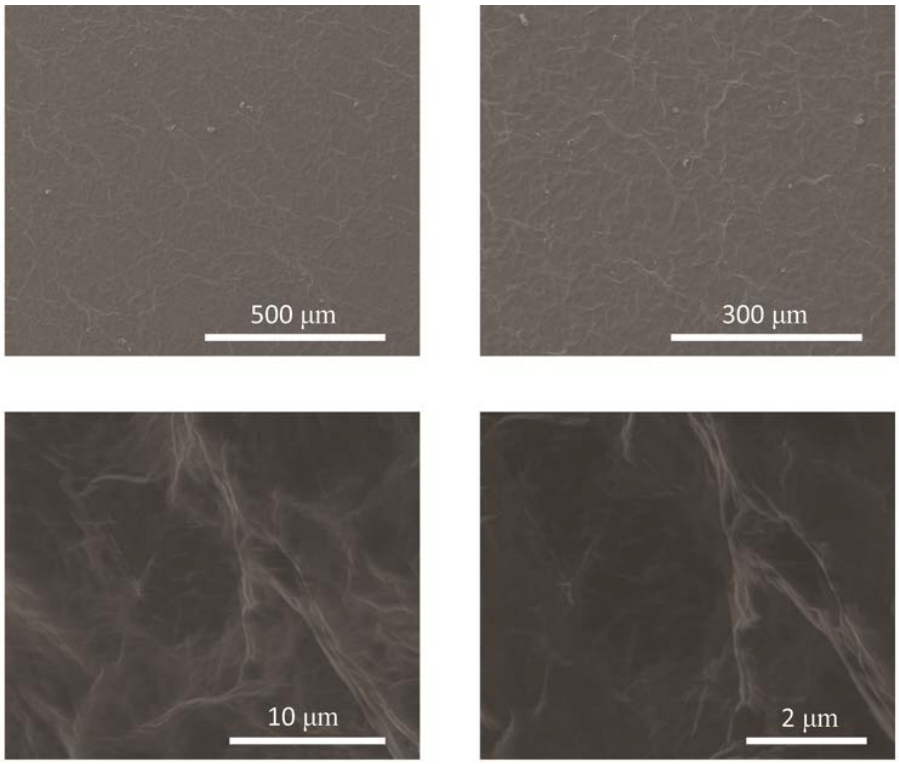

Figure 3.5. SEM images of dried unreduced graphene oxide film at 0.1 k, 0.2 k, 5 k, 10 k magnification showing a different morphology from pre-FCG and post-FCG. Graphene oxide is a continuous film relative to FCG, and is seen to have a less porous structure.

The BET surface area of FCG (733 m^2 g^{-1}) is higher than that of the starting material, graphene oxide (15 m^2 g^{-1}) (Figure 3.6), but does not reach the theoretical specific surface area of graphene (2630 m^2 g^{-1}).[18] The lower surface area of FCG may be due to incomplete reduction of graphene oxide or some restacking of graphene sheets.

XPS and XRD were carried out on the FCG to shed light on the extent of the π conjugation by investigating the amount of remaining unreduced oxygen. The percentages of carbon and oxygen in pre-FCG are 79% and 21%, respectively, while post-FCG electrodes contain 85.6% carbon and 14.4% oxygen (Figure 3.7).

Comparing the XRD pattern of FCG to that of GO indicates that the majority of GO was reduced to graphene

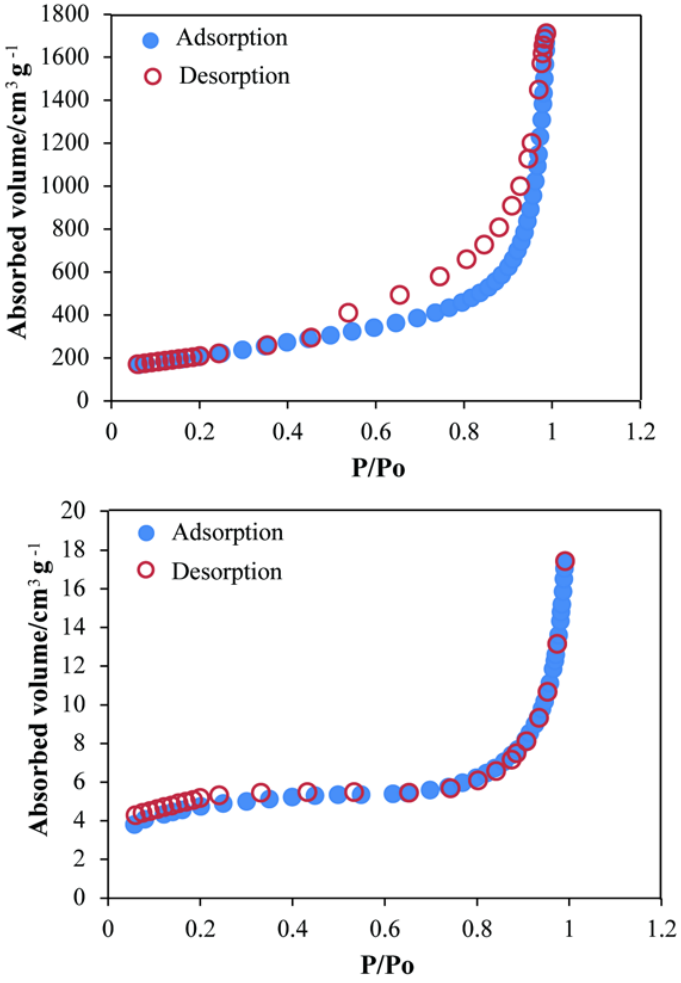

Figure 3.6. ET nitrogen (77 K) adsorption isotherms for FCG powder used in the electrodes (top) and for graphene oxide (GO) (bottom). The FCG BET surface area is 733 m^2 g^{-1}, whereas the BET surface area of the freeze-dried GO is only 15 m^2 $g^{-}1$.

during the flashing process (Figure 3.8). The post-FCG shows no diffraction peaks, whereas the pre-FCG shows two small intensity peaks that indicate the presence of some graphene oxide. Since the flash lamp emits a high-power pulse of light energy the graphene oxide is heated locally. The heat penetrates deeper

below the surfaces of the electrode material with more flash treatments. Because post-FCG is first cast into a GO film on the current collector before the flashing process, the photothermal energy can penetrate the thin film of graphene oxide, resulting in more complete reduction. In contrast, pre-FCG is flashed as bulk GO powder before casting. The bulk freeze-dried GO is thicker than its cast post-FCG counterpart, which can prevent the penetration of light and thus heat from the flash to reach all of the underlying material. Any unreduced oxygen will act as a barrier for the delocalized π-system in the graphene sheets, thereby limiting the electrical conductivity.[15]

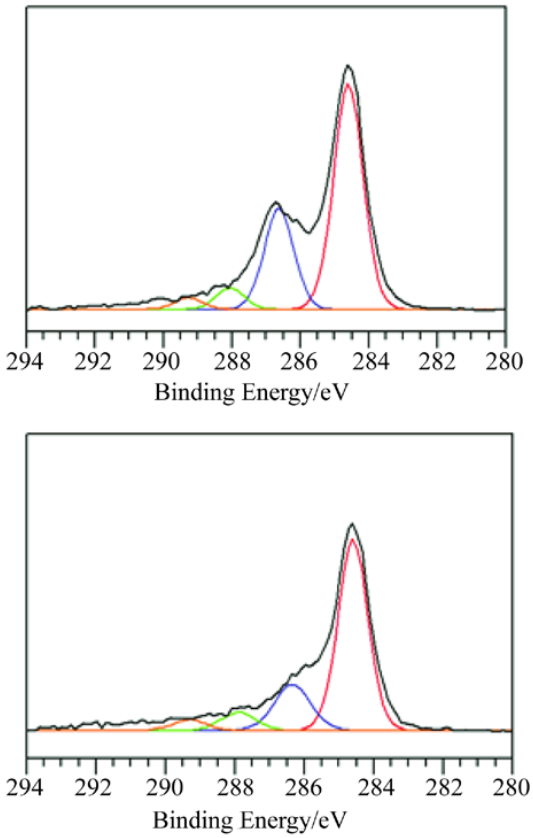

Figure 3.7. XPS high-resolution C 1s spectra of pre-FCG (top) and post-FCG (bottom). The spectral component at 284.6 eV (red) corresponds to sp^2 carbon. Oxygen containing groups, such as C-OH, C=O/C-O-C, and –COOH are shown at 286.7 eV (blue), 288.0 eV (green), and 289.3 eV (orange), respectively.

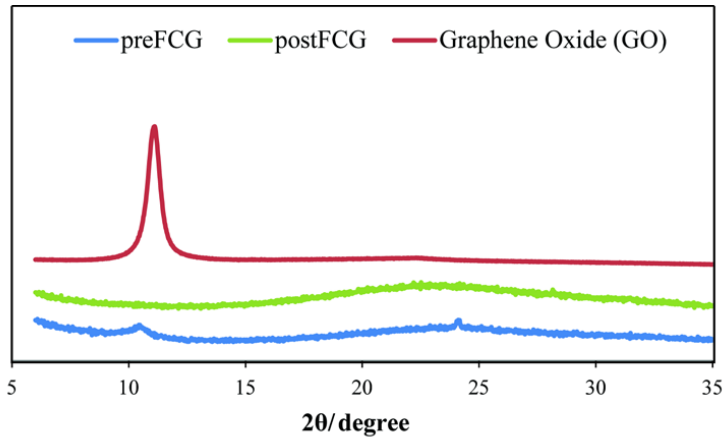

Figure 3.8. X-ray diffraction pattern comparing flash converted graphene used for electrodes (pre-FCG and post-FCG) to GO. A distinct peak in the GO pattern can be seen at 12° 2θ, but only small diffraction peaks are present for pre-FCG and no peaks for post-FCG. The lack of peaks indicates a disordered 3D morphology.

Along with electrode morphology, the electrical conductivity plays a key role in the performance of a supercapacitor. The conductivity of a carbon material depends on the delocalization of π-electrons throughout the system. Pristine graphite has high conductivity because of its large delocalized π-system. Graphene oxide, in contrast, possesses a low conductivity because the π-system is disrupted by sp^3 carbons bound to oxygen atoms or oxygen containing carbonyl or epoxide groups. When converted with a flash, the resulting FCG material exhibits relatively good conductivity of 60.7 S m^{-1} (Equation 3.1) compared to the resistive GO starting material (<0.01 S m^{-1}). The conductivity of FCG is comparable to activated carbon electrodes (10–100 S m^{-1}), but lower than chemically converted graphene (≈7200 S m^{-1}),[15–17] probably due to incomplete reduction to graphene during the flash process.

To test the performance of the FCG electrodes in supercapacitors, devices were fabricated from both methods. The pre-FCG and post-FCG electrodes both demonstrate electric double-layer behavior with good capacitance, and extremely high specific power and rate capabilities. The specific power and rate capabilities are significantly higher than many state-of-the-art supercapacitors as determined from both cyclic voltammetry (CV) and constant current (CC) electrochemical measurements (Figure 3.9).

The gravimetric capacitance of the pre-FCG supercapacitor is 48 F $g^{-1}_{FCG/electrode}$ and that of the post-FCG supercapacitor device is 64 F $g^{-1}_{FCG/electrode}$ using a 0–2 V window at a current density of 1 A g^{-1}_{FCG}. At 10 A g^{-1}_{FCG} from 0 to 2 V, the gravimetric capacitance of pre-FCG and post-FCG is 40 and 60 F $g^{-1}_{FCG/electrode}$, respectively. When increased to a 2.6 V window, the capacitance of post-FCG doubled to 88 F $g^{-1}_{FCG/electrode}$. The corresponding specific energy of pre-FCG and post-FCG supercapacitor devices (based on the total FCG active material) at 1 A g^{-1}_{FCG} are 7 and 9 Wh kg^{-1}, respectively.

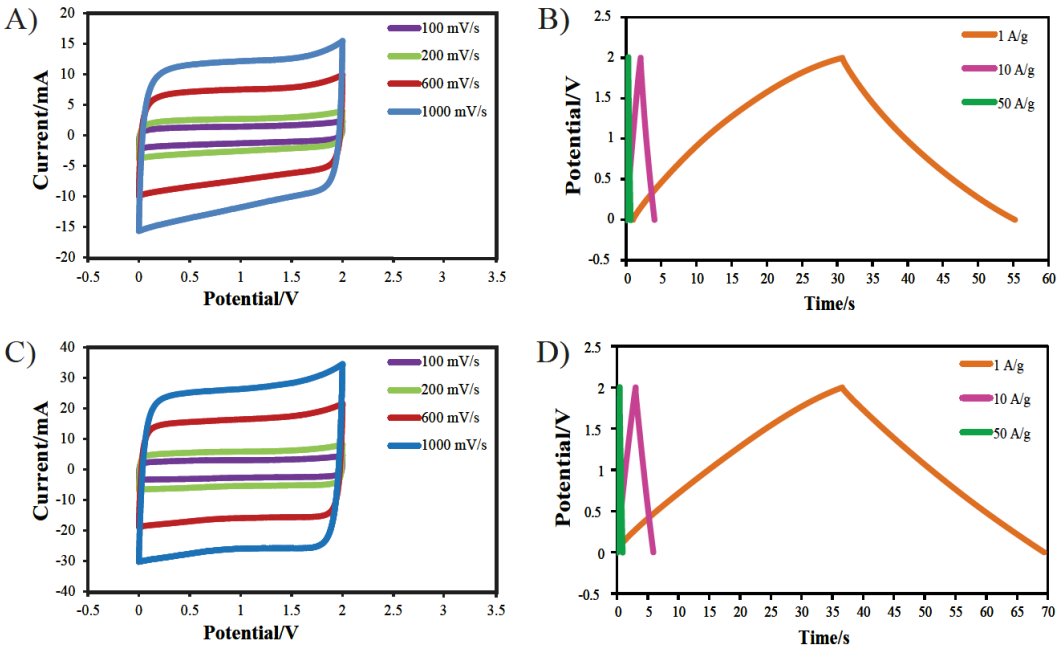

Figure 3.9. Electrochemical performance of A, B) pre-FCG and C, D) post-FCG supercapacitor devices. A, C) Cyclic voltammetry of pre-FCG and post-FCG at scan rates of 100, 200, 600, and 1000 mV s^{-1}. The nearly rectangular shape indicates essentially pure capacitive charging through electrochemical double layers. B, D) Constant current charge–discharge curves of pre FCG and post-FCG at 1, 10, and 50 A $g^{-1}_{FCG/electrode}$.

Compared with other recently reported electric double-layer capacitors such as 3D sponge-like graphene (SPG) and graphene hydrogels,[37,38] the FCG CR2032 coin cell supercapacitor devices show improved electric double-layer behavior, with higher rate capabilities by greater than a factor of two, while possessing comparable specific energy (Table 3.1).

Additionally, the FCG CR2032 devices exhibit significantly higher power than the majority of graphene EDLCs currently reported. The specific power for pre-FCG and post-FCG at 1 A g^{-1}_{FCG} from 0 to 2 V is 5×10^5 and 7×10^5 W kg^{-1}, respectively. FCG devices possess specific power over two times that of

microwave exfoliated GO (a-MEGO),[39] one order of magnitude higher than 3D SPG[37] and pillared graphene paper (GP),[40] and two to three orders of magnitude higher than a thermally reduced melamine resin functionalized GO ($cMRrGO_{th}$), a hydrazine reduced GO (rGO_H), a carbon nanotube GO composite ($CNT\text{-}rGO_{th}$),[41] and graphene hydrogels.[38] Furthermore, the specific power of FCG CR2032 coin cell supercapacitor devices is one order of magnitude higher than that of several common commercial devices (Table 3.2).[42]

Sample	Reference	Synthesis method	Wh kg^{-1}	W kg^{-1}	IR drop [V]	Rate capability (70%) [A g^{-1}]
Pre-FCG	Present work	Flash	7	5×10^5	2.9×10^{-3}	4.5×10
Post-FCG	Present work	Flash	9	7×10^5	3.2×10^{-3}	9×10
3D SPG	37	Microwave	7	5×10^4	–	–
Graphene hydrogel	38	Hydrothermal	4.5–6.5	$<5 \times 10^3$	–	2×10
a-MEGO	39	Exfoliation-activation	70	3×10^5	3.4×10^{-2}	–
Pillared GP	40	Exfoliation-chemical	26	5×10^4	–	–
$cMR\text{-}rGO_{th}$	41	Functionalized-thermal	6–25	$<4 \times 10^3$	–	–
rGO_H	41	Chemical	3–14	$<3 \times 10^3$	–	–
$CNT\text{-}rGO_{th}$	41	Microwave-thermal	4–5	$<1 \times 10^3$	–	–

Table 3.1. Comparison of FCG and state-of-the-art graphene supercapacitors.

Sample	g/cm^3	$F/g_{electrode}$ (1 A/g)	Wh/kg	W/kg	IR Drop (V)	Rate Capability (50%) (A/g)
pre-FCG	0.039	48	7	$5x10^5$	$2.9x10^{-3}$	$2.2x10^2$
post-FCG	0.008	64	9	$7x10^5$	$3.2x10^{-3}$	$2.2x10^2$
Commercial EC1	0.540	44	6	$7x10^4$	$2.9x10^{-2}$	$4.0x10^1$
Commercial EC2	0.480	80	11	$6x10^4$	$3.3x10^{-2}$	$2.0x10^1$
Commercial EC3	0.036	80	11	$6x10^4$	$2.9x10^{-2}$	$5.0x10^0$

Table 3.2. Comparison of FCG and commercial CR2032 supercapacitors.

Density plays an important role in the gravimetric and volumetric performance of supercapacitor devices. The post-FCG electrode has a very low density (0.0080 g cm^{-3}) and exhibits higher specific energy and power, but lower volumetric capacitance (1.2×10^{-1} F $cm^{-3}_{/device}$). The pre-FCG electrode density is 0.039 g cm^{-3} and shows a lower specific energy and power, but a higher volumetric capacitance (2.5×10^{-1} F $cm^{-3}_{/device}$). The density of the electrode material is important because a lower density means it has more void space, not only allowing more surface area for ion adsorption, but also for faster ion transport. However, the low density FCG electrode is not as robust, with less adhesion between the material and the current collector than denser electrodes. Thus, the rate capability of pre-FCG is greater than that of post-FCG. However, both pre-FCG and post-FCG are made from purely carbon materials, with no binders or other inactive additives. This has the advantage of easy production with the potential for lower cost and toxicity.[13]

The high power of the FCG devices can also be deduced from the rectangular CV shape, even at high scan rates of 1000 mV s^{-1}. The sharp vertical transitions at 0 and 2 V in the CV indicate very low active material resistance resulting in low ESR and high power.

On a mechanistic level, the precise rectangular shape of the CV indicates ideal electrochemical double-layer formation during charging and discharging of current. The storage of electrons is mainly due to adsorption of ions on the surfaces of the graphene sheets. Thus, the pure EDL behavior enables the fast

response and speed of ion adsorption on the FCG active material, thereby giving rise to an enhanced power density. Additionally, post-FCG can be run at an even higher potential window. A preliminary test of the device at 2.6 V gave a capacitance of 88 F $g^{-1}_{FCG/electrode}$, a 36% increase in capacitance when compared to that obtained with a 2 V window.

Electrochemical impedance spectroscopy was employed on the FCG supercapacitor devices at open circuit potential from 1 MHz to 10 mHz to further characterize their electrochemical behavior (Figure 3.10).

Both pre-FCG and post-FCG devices show capacitance behavior at high frequencies of 360.6 and 178.9 Hz, respectively, translating to fast time responses. The time response from the Bode plot at –45° for pre-FCG is 4.6×10^{-1} s and for post-FCG is 2.3×10^{-1} s (Figure 3.11). The ESR of pre-FCG is estimated to be 5.1 Ω and that of post-FCG is estimated to be 0.9 Ω. The ESR of the FCG electrodes is exceedingly low. The post-FCG electrode has an ESR even lower than other reputed electrode materials including a-MEGO (4.6 Ω)[39] and graphene hydrogel (3.5 Ω).[38] The low ESR values of FCG are consistent with EDL formation and fast ion transport. Both pre-FCG and post-FCG CR2032 coin cell devices retained 50% relative capacitance at a fast rate of 220 A g^{-1}_{FCG}, but even more impressive is that pre-FCG and post-FCG devices retained >1% relative capacitance at 900 and 500 A g^{-1}_{FCG}. One of the leading graphene-based supercapacitors, graphene hydrogels, was reported to retain 70% relative capacitance at 20 A g^{-1}.[38] Here, the FCG electrodes retain 77% and 86% relative

capacitance at 20 A g^{-1}. Furthermore, as a comparison, three commercial supercapacitors retained 50% relative capacitance at only 5–40 A $g^{-1}_{\text{total active material}}$, and retained >1% relative capacitance only up to 12–80 A $g^{-1}_{\text{total active material}}$. The superior rate capability of FCG supercapacitors make them potentially attractive for applications such as load leveling and space exploration.

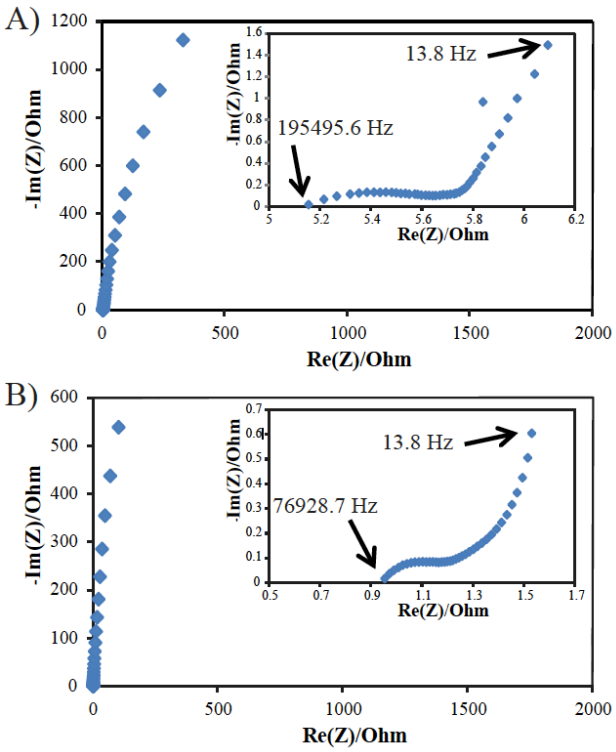

Figure 3.10. Electrochemical impedance spectroscopy: a Nyquist plot of A) pre-FCG and B) post FCG devices. The insets expand the high-frequency region.

Finally, the cycle stability of FCG devices was tested. A device of post-FCG was charged and discharged over 5000 times at 1 A g^{-1}_{FCG}. The device retained 78.5% capacitance after 1000 cycles and after that remained nearly constant up to 5000 cycles (Figure 3.12). The loss in capacitance may be due to the presence

of residual oxygen impurities from the flash conversion process of graphene oxide to FCG. As previously stated, the amount of residual oxygen, found in the form of OH, C=O/C–O–C, and –COOH, in the FCG material is 14.4%–21% (Figure 3.7). These functional groups could increase the specific capacitance of FCG slightly by introducing pseudo- capacitance through redox reactions. However, these redox reactions suffer from poor cycling stability and can lead to the rapid

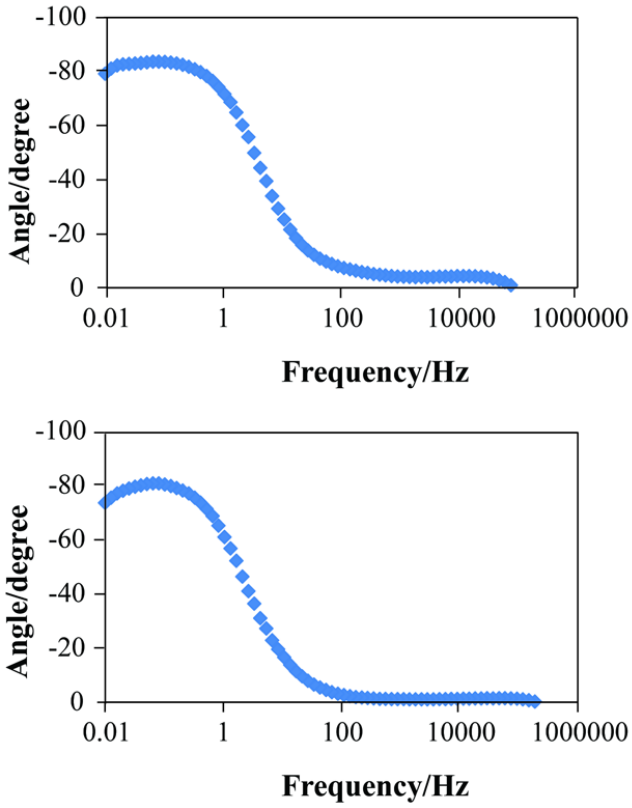

Figure 3.11. Bode plot of pre-FCG (top) and post-FCG (bottom) coin cell devices measured from 1 MHz to 10 mHz at open circuit potential. The time constant is taken from the -45° frequency, where the device exhibits 50% capacitive and 50% resistive characteristics.

degradation of the material observed in the initial scans (Figure 3.12, first 1000 cycles).[43,44] This is because the chemical nature of these functional groups

changes with cycling. Experiments show that the FCG exhibits very stable electrochemical response beyond 1000 cycles as it stores charge mainly via an EDLC mechanism in which only ion adsorption in the double layer is responsible for charge storage. Therefore, while the material shows a 20% reduction in capacity in the initial charge/discharge cycles, it then exhibits a very stable response in subsequent cycles.

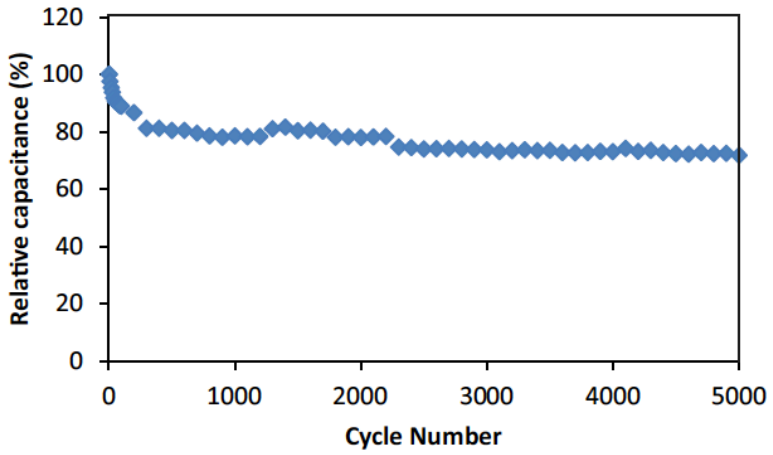

Figure 3.12. Constant current charge–discharge cycling at a current density of 1 A g^{-1}.

The coulombic efficiency (CE) of the first cycle is 93% whereas the coulombic efficiency after cycle 500 is 98%. The slightly lower CE in the first cycle suggests that some of the charge may be used in reactions involving the residual oxygen. Furthermore, the electrolyte decomposition or the decomposition of the material can also contribute to a low CE. Another possible cause is the poor wetting of the material at the first cycle which improves in the subsequent cycles due to electrochemical activation of the material. Nevertheless, the FCG devices

still show good cycle stability in terms of capacitance as well as power. The IR drop increased only 16.6% after 1000 cycles, with retention of 85.7% of its power.

3.4 Conclusions

The photo-thermal conversion of GO to graphene via a camera flash lamp yields FCG with a 3D framework, causing a 3D structure that effectively prevents restacking of sheets. Two new methods for fabricating FCG into devices known as pre-FCG and post FCG are demonstrated with specific energies of 7 and 9 Wh kg^{-1}, and extremely high power (5×10^5 and 7×10^5 W kg^{-1}) and rate capabilities (900 and 500 A g^{-1}).

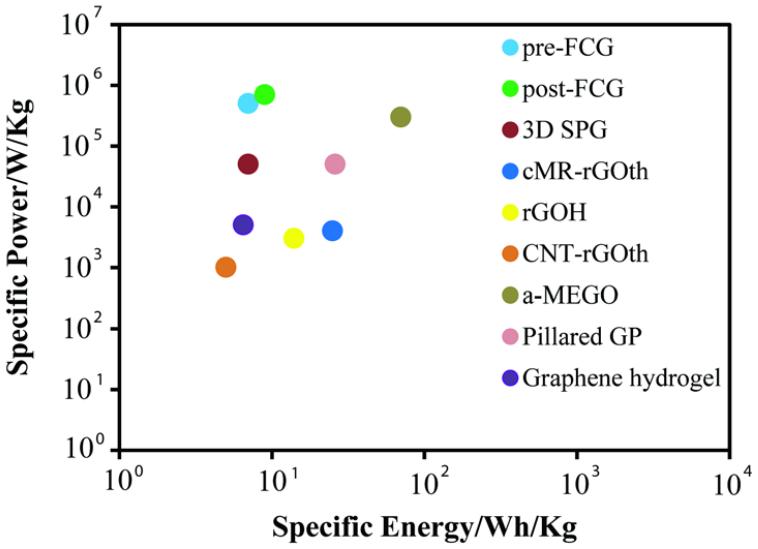

Figure 3.13. Ragone plot illustrating the high specific power of pre-FCG and post-FCG supercapacitor devices as compared to other state-of-the-art graphene-based supercapacitors devices.

The power and rate capability of the FCG CR2032 coin cell devices are higher than that of many state-of-the-art graphene-based CR2032 coin cell supercapacitors (Figure 3.13) and higher than that of several commercial supercapacitors (Table 3.2). The flash method is also straightforward and versatile. FCG supercapacitors are readily made into commercially viable form factors such as coin cells that could be used in a wide range of applications.

3.5 Acknowledgments

This work was supported through funding by Maxwell Technologies (RBK). The authors thank Michael Yeung and Chris Turner for valuable discussions and Dr. Gregory Khitrov for his help with GC-MS.

References

(1) BCC Research, Supercapacitors: Technology Developments and Global Markets, http://www.bccresearch.com/market-research/energy-and-resources/supercapacitors-technology-developmentmarkets-report-egy068b.html (accessed: July **2015**).

(2) Kiamahalleh, M. V.; Zein, S. H. S. in *Nanostructured Ceramic Oxides for Supercapacitor Applications* (Eds: Balakrishnan, A.; Subramanian, K. R. V.), CRC Press, Boca Raton, FL **2014**, Ch. 6.

(3) Transparency Market Research, Ultracapacitors Market – Global Industry Analysis, Size, Share, Growth, Trends, and Forecast, 2013–2019, http://www.transparencymarketresearch.com/capacitors-market.html (accessed: July **2015**).

(4) Chu, A.; Braatz, P. Comparison of commercial supercapacitors and high-power lithium-ion batteries for power-assist applications in hybrid electric vehicles I. Initial characterization. *J. Power Sources* **2002**, 112, 236.

(5) Harrop, P. (IDTechEx), Why ultracapacitors maintain 30% market growth, http://www.electricvehiclesresearch.com/articles/4825/whyultracapacitors-maintain-30-market-growth (accessed: July 2015).

(6) Pandolfo, A. G.; Hollenkamp, A. F. Carbon properties and their role in supercapacitors. *J. Power Sources* **2006**, 157, 11.

(7) Lee, J.-S.; Kim, S.-I.; Yoon, J.-C.; Jang, J.-H. Chemical vapor deposition of mesoporous graphene nanoballs for supercapacitor. *ACS Nano* **2013**, 7, 6047.

(8) Izadi-Najafabadi, A.; Yamada, T.; Futaba, D. N.; Yudasaka, M.; Takagi, H.; Hatori, H.; Iijima, S.; Hata, K. High-power supercapacitor electrodes from single-walled carbon nanohorn/nanotube composite. *ACS Nano* **2011**, 5, 811.

(9) Potter, S.; Bayer, M.; Davis, D.; Born, A.; McCormick, D.; Dorazio, L.; Patel, P. *47th AIAA Aerospace Sciences Meeting and The New Horizons Forum and Aerospace Exhibit 2009*, American Institute for Aeronautics and Astronautics (AIAA), **2009**.

(10) Cabrera, C. R.; Miranda, F. *Advanced Nanomaterials for Aerospace Applications*, CRC Press, **2014**.

(11) Lanning, B.; Martin, D.; *Survey of Current and Next Generation Space Power Technologies*, American Institute of Aeronautics and Astronautics, Inc., Reston, VA **2006**.

(12) Krishen, K. High-power supercapacitor electrodes from single-walled carbon nanohorn/nanotube composite. *Acta Astronaut.* **2008**, 63, 324.

(13) Stoller, M. D.; Park, S.; Zhu, Y.; An, J.; Ruoff, R. S. Graphene-based ultracapacitors. *Nano Lett.* **2008**, 8, 3498.

(14) Yan, J.; Wang, Q.; Wei, T.; Fan, Z. Recent advances in design and fabrication of electrochemical supercapacitors with high energy densities. *Adv. Energy Mater.* **2014**, 4, 1300816.

(15) Li, D.; Muller, M. B.; Gilje, S.; Kaner, R. B.; Wallace, G. G. Processable aqueous dispersions of graphene nanosheets. *Nat. Nanotechnol.* **2008**, 3, 101.

(16) Moon, I. K.; Lee, J.; Ruoff, R. S.; Lee, H. Reduced graphene oxide by chemical graphitization. *Nat. Commun.* **2010**, 1, 73.

(17) Chandrasekaran, R.; Soneda, Y.; Yamashita, J.; Kodama, M.; Hatori, H. Preparation and electrochemical performance of activated carbon thin films with polyethylene oxide-salt addition for electrochemical capacitor applications. *J. Solid State Electrochem.* **2008**, 12, 1349.

(18) Zhu, Y.; Murali, S.; Cai, W.; Li, X.; Suk, J. W.; Potts, J. R.; Ruoff, R. S. Graphene and graphene oxide: synthesis, properties, and applications. *Adv. Mater.* **2010**, 22, 3906.

(19) Lee, J. H.; Park, N.; Kim, B. G.; Jung, D. S.; Im, K.; Hur, J.; Choi, J. W. Restacking-inhibited 3D reduced graphene oxide for high performance supercapacitor electrodes. *ACS Nano* **2013**, 7, 9366.

(20) Xu, Y.; Bai, H.; Lu, G.; Li, C.; Shi, G. Flexible graphene films via the filtration of water-soluble noncovalent functionalized graphene sheets. *J. Am. Chem. Soc.* **2008**, 130, 5856.

(21) Luo, J.; Jang, H. D.; Huang, J. Effect of sheet morphology on the scalability of graphene-based ultracapacitors. *ACS Nano* **2013**, 7, 1464.

(22) Kim, T.; Jung, G.; Yoo, S.; Suh, K. S.; Ruoff, R. S. Activated graphene-based carbons as supercapacitor electrodes with macro- and mesopores. *ACS Nano* **2013**, 7, 6899.

(23) Tung, V. C.; Allen, M. J.; Yang, Y.; Kaner, R. B. High-throughput solution processing of large-scale graphene. *Nat. Nanotechnol.* **2009**, 4, 25.

(24) Shin, H.-J.; Kim, K. K.; Benayad, A.; Yoon, S.-M.; Park, H. K.; Jung, L.-S.; Jin, M. H.; Jeong, H.-K.; Kim, J. M.; Choi, J.-Y.; Lee, Y. H. Efficient reduction of graphite oxide by sodium borohydride and its effect on electrical conductance. *Adv. Funct. Mater.* **2009**, 19, 1987.

(25) Stankovich, S.; Dikin, D. A.; Piner, R. D.; Kohlhaas, K. A.; Kleinhammes, A.; Jia, Y.; Wu, Y.; Nguyen, S. T.; Ruoff, R. S. Efficient reduction of graphite oxide by sodium borohydride and its effect on electrical conductance. *Carbon* **2007**, 45, 1558.

(26) Jin, Z.; Lomeda, J. R.; Price, B. K.; Lu, W.; Zhu, Y.; Tour, J. M. Mechanically assisted exfoliation and functionalization of thermally converted graphene sheets. *Chem. Mater.* **2009**, 21, 3045.

(27) Jung, I.; Field, D. A.; Clark, N. J.; Zhu, Y.; Yang, D.; Piner, R. D.; Stankovich, S.; Dikin, D. A.; Geisler, H.; Ventrice, C. A.; Ruoff, R. S. Reduction kinetics of graphene oxide determined by electrical transport measurements and temperature programmed desorption. *J. Phys. Chem. C* **2009**, 113, 18480.

(28) Shao, Y.; Wang, J.; Engelhard, M.; Wang, C.; Lin, Y. Facile and controllable electrochemical reduction of graphene oxide and its applications. *J. Mater. Chem.* **2010**, 20, 743.

(29) Gilje, S.; Dubin, S.; Badakhshan, A.; Farrar, J.; Danczyk, S. A.; Kaner, R. B. Photothermal deoxygenation of graphene oxide for patterning and distributed ignition applications. *Adv. Mater.* **2010**, 22, 419.

(30) El-Kady, M. F.; Strong, V.; Dubin, S.; Kaner, R. B. Laser scribing of high performance and flexible graphene-based electrochemical capacitors. *Science* **2012**, 335, 1326.

(31) Bard, A. J.; Faulkner, L. R. *Electrochemical Methods: Fundamentals and Applications*, Wiley, New York **2001**.

(32) Péan, C.; Merlet, C.; Rotenberg, B.; Madden, P. A.; Taberna, P.-L.; Daffos, B.; Salanne, M.; Simon, P. On the dynamics of charging in nanoporous carbon-based supercapacitors. *ACS Nano* **2014**, 8, 1576.

(33) Zhang, L. L.; Zhao, X. S. Carbon-based materials as supercapacitor electrodes. *Chem. Soc. Rev.* **2009**, 38, 2520.

(34) Zhi, M.; Xiang, C.; Li, J.; Li, M.; Wu, N. Nanostructured carbon–metal oxide composite electrodes for supercapacitors: a review. *Nanoscale* **2013**, 5, 72.

(35) Frackowiak, E.; Béguin, F. Nanostructured carbon–metal oxide composite electrodes for supercapacitors: a review. *Carbon* **2001**, 39, 937.

(36) Schneuwly, A.; Gallay, R. *Properties and Applications of Supercapacitors From the State-of-the-art to Future Trends*, Adams/Intertec International, Cathedral City, CA **2000**.

(37) Xu, Z.; Li, Z.; Holt, C. M. B.; Tan, X.; Wang, H.; Amirkhiz, B. S.; Stephenson, T.; Mitlin, D. Electrochemical supercapacitor electrodes from sponge-like graphene nanoarchitectures with ultrahigh power density. *J. Phys. Chem. Lett.* **2012**, 3, 2928.

(38) Xu, Y.; Lin, Z.; Huang, X.; Liu, Y.; Huang, Y.; Duan, X. Flexible solid-state supercapacitors based on three-dimensional graphene hydrogel films. *ACS Nano* **2013**, 7, 4042.

(39) Zhu, Y.; Murali, S.; Stoller, M. D.; Ganesh, K. J.; Cai, W.; Ferreira, P. J.; Pirkle, A.; Wallace, R. M.; Cychosz, K. A.; Thommes, M.; Su, D.; Stach, E. A.; Ruoff, R. S. Carbon-based supercapacitors produced by activation of graphene. *Science* **2011**, 332, 1537.

(40) Wang, G.; Sun, X.; Lu, F.; Sun, H.; Yu, M.; Jiang, W.; Liu, C.; Lian, J. Flexible pillared graphene-paper electrodes for high-performance electrochemical supercapacitors. *Small* **2012**, 8, 452.

(41) Lee, J. H.; Park, N.; Kim, B. G.; Jung, D. S.; Im, K.; Hur, J.; Choi, J. W. Restacking-inhibited 3D reduced graphene oxide for high performance supercapacitor electrodes. *ACS Nano* **2013**, 7, 9366.

(42) Burke, A. R&D considerations for the performance and application of electrochemical capacitors. *Electrochim. Acta* **2007**, 53, 1083.

(43) Li, Z.; Zhang, L.; Amirkhiz, B. S.; Tan, X.; Xu, Z.; Wang, H.; Olsen, B. C.; Holt, C. M. B.; Mitlin, D. Carbonized chicken eggshell membranes with 3D architectures as high-performance electrode materials for supercapacitors. *Adv. Energy Mater.* **2012**, 2, 431.

(44) Hammar, A.; Venet, P.; Lallemand, R.; Coquery, G.; Rojat, G. Study of accelerated aging of supercapacitors for transport applications. *IEEE Ind. Electron. Mag.* **2010**, 57, 3972.

(45) Dreyer, D. R.; Park, S.; Bielawski, C. W.; Ruoff, R. S. The chemistry of graphene oxide. *Chem. Soc. Rev.* **2010**, 39, 228.

(46) Li, D.; Muller, M. B.; Gilje, S.; Kaner, R. B.; Wallace, G. G. Processable aqueous dispersions of graphene nanosheets. *Nat. Nanotechnol.* **2008**, 3, 101.

CHAPTER 4

Scalable Antifouling Reverse Osmosis Membranes Utilizing Perfluorophenyl Azide Photochemistry

4.1 Background

The World Health Organization provided a plan this past year to ensure that the world's population has access to a basic clean water supply by 2030.[1] Presently, over one billion people do not have access to clean water and dwindling freshwater supplies are leading to new health, environmental, and geopolitical implications in the 21st century.[2,3] Unfortunately, natural purification of water, i.e. through sedimentation and aquifers, cannot sustain these future demands.[4] New technologies must be developed to treat water effectively from traditional and nontraditional sources to adequately supply global needs.

Reverse osmosis (RO) has emerged as a leading technology in water treatment for its ability to efficiently convert seawater and brackish water into high purity water for potable and high tech applications. The polymeric thin-film membranes used for RO exhibit high flux, high selectivity, low cost, and relatively low energy expenditure compared with alternative desalination technologies.[3,5] Acting as a physical barrier, RO membranes allow water molecules to permeate through a dense, microporous film and reject small dissolved solutes. Among numerous polymeric materials used to fabricate RO membranes, aromatic polyamide membranes are the most widely used because of their superior transport and separation properties. Thin-film composite membranes are produced on an industrial scale using roll-to-roll processing and are packaged into spiral wound elements to achieve optimal performance.

Although polyamide membranes have approached theoretical limits on performance, they are highly susceptible to biological surface fouling that significantly reduces intrinsic operational and economic advantages.[2,3,6] Microorganisms in the feed water adsorb onto the surface via hydrophobic interactions and block the flow of water

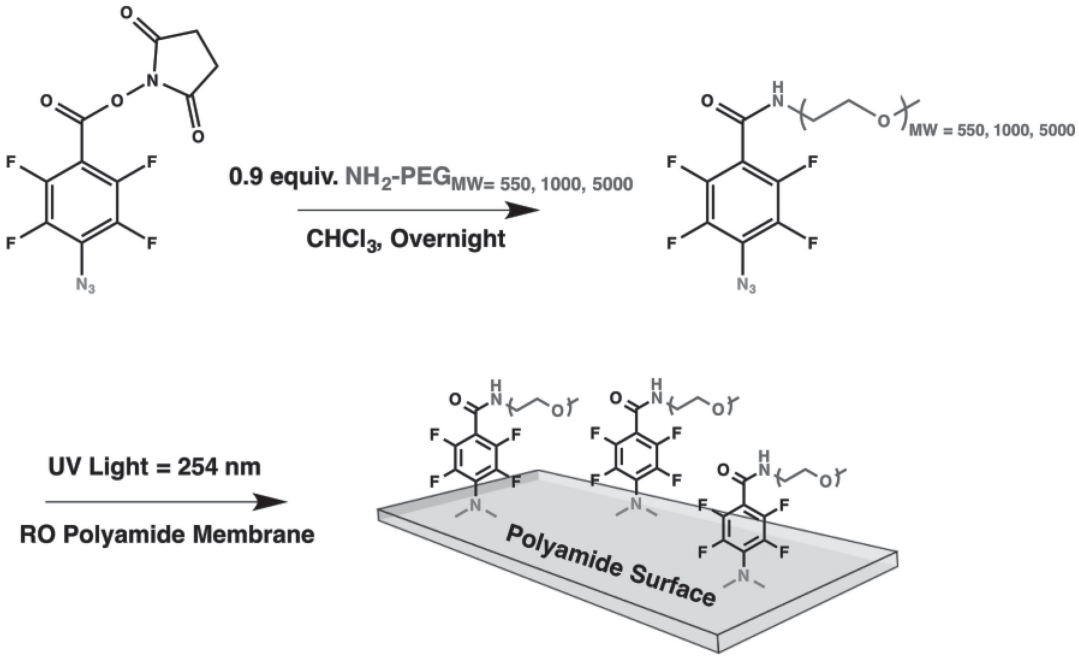

Figure 4.1. Synthesis of PFPA-terminated PEG brush polymers and their attachment to an RO membrane surface.

through the membrane. Harsh chemical disinfectants used to prevent the growth of biofilms on the surface, such as chlorine and base treatments, prevent and remove biofilms from the surface, but also attack the chemical bonds within the polyamide layer and degrade the high selectivity of the membranes.[7,8] Thus, biogrowth inhibition and cleaning agents that are commonly used in water

treatment cannot be used with RO membranes, increasing the pretreatment, operating and maintenance costs of desalination plants.[9–11]

Recently, researchers have attempted to reduce or prevent RO membrane biofouling by developing antifouling membrane surface treatments.[12,13] By covalently modifying the surface with hydrophilic brush polymers,[14–19] hydrophobic interactions between the foulant and the membrane surface are obstructed. In addition, initial attachment of biological cells and dissolved organics, a key step in biofilm formation, is impeded. A hydrophilic surface forms a layer of hydration[20] that prevents foulants from adsorbing onto the surface of the membrane film and allows water to pass freely through the membrane.

Unfortunately, the designed chemical stability of polyamide membranes makes surface manipulations a difficult task. Previous studies have utilized reactive epoxide terminal groups,[15] carbodiimide activation,[16] or radical-initiated graft polymerizations that chemically attach the hydrophilic polymers to the polyamide surface.[13,16–19] However, these modifications require long reaction times, exotic reaction conditions, and are performed *in situ*, preventing them from being easily translated into commercial roll-to-roll manufacturing processes for thin-film composite membranes.

The need for a scalable method to produce antifouling RO membranes has led us to investigate the use of perfluorophenyl azide (PFPA) as a chemical modifier. PFPAs are known for their highly reactive azide group that allows PFPA

derivatives[21,22] to make chemical bonds with rather unreactive targets, such as graphene,[23,24] carbon nanotubes,[25] fullerenes,[26] and organic polymers.[27] The azide functionality is activated by photoexcitation that expels nitrogen gas and affords a reactive singlet nitrene that inserts into –NH– and C=C bonds.[28,29] The surface layer of RO membranes is comprised of crosslinked polyamide networks that contain these groups, thus providing a target for modification. Our goal is to develop a dip-coating technique using PFPA derivatives that confers antifouling properties to RO membranes and maintains the roll-to-roll manufacturing process.

Because PFPAs can be prepared with a functional ester group in the *para*-position relative to the azide moiety, PFPAs can be readily coupled to molecules containing free amino or hydroxyl groups to form corresponding amide or ester linkages (Figure 4.1). In this communication, we have synthesized three hydrophilic polyethyleneglycol (PEG) brush polymers of different molecular weights (MW = 550, 1000, 5000 Daltons) with a terminal PFPA group. PFPA-PEG_{550}, PFPA-PEG_{1000}, and PFPA-PEG_{5000} are used to denote the respective PFPA-terminated PEG derivatives according to their molecular weight. The water solubility of the PFPA-PEGs allows the product to be isolated in high purity from the starting material by using an aqueous phase extraction. More importantly, the water solubility enables RO membranes to be dipped in an aqueous solution containing the dissolved PFPA-PEG derivatives. This is attractive commercially, as many common organic solvents dissolve the underlying polysulfone layer supporting the thin-film composite membrane.

4.2 Experimental methods and characterization

4.2.1 Materials

Methoxypolyethylene glycol amine MW = 5000 g/mol was purchased from Sigma Aldrich (Milwaukee, WI), methoxypolyethylene glycol amines MW = 550, 1000 g/mol were purchased from Laysan Bio (Arab, AL), N-hydroxysuccinimidyl 2,3,5,6 tetrafluorobenzoate was prepared according to Keana and Cai.[30] Diethyl ether and methanol were purchased from Fisher Scientific (Pittsburgh, PA). Dow FILMTEC XLE brackish water flat sheet membranes were donated by Dow Water & Processes Solutions (Edina, MN). The membranes were soaked in DI water overnight to remove the shipping preservative and dried. Unless otherwise stated, all materials were used as received.

4.2.2 Instrumentation

^{1}H and ^{19}F-NMR spectroscopy was conducted on a Bruker AV 300 NMR Spectrometer. Spectra were recorded in a solution of $CDCl_3$ at room temperature, referenced to a residual solvent peak for $CDCl_3$ (^{1}H) and $CFCl_3$ (^{19}F). ATR-IR of PFPA PEG samples was conducted on the products using a JASCO FT/IR-6300 spectrometer with an ATR accessory.

4.2.3 Synthesis of PFPA-PEG$_{5000}$

H_2N-PEG_{5000} (750 mg, 0.15 mmol) was dissolved in 10 mL of $CHCl_3$. *N*-hydroxysuccinimidyl 2,3,5,6-tetrafluorobenzoate (60 mg, 0.18 mmol) was added to solution and the reaction was allowed to stir in the dark overnight at room temperature. The resulting solution was poured into 20 mL of diethyl ether and the product was extracted 3 times with 20 mL DI water. A grey solid product (745 mg, 0.14 mmol, yield: 93%) was obtained via evaporation under reduced pressure and stored in a dessicator in the dark before use. ^{1}H NMR (300 MHz, $CDCl_3$, 25˚C, TMS): δ = 3.63 ppm (m, O-CH_2) ^{19}F NMR (300 MHz, $CDCl_3$, $CFCl_3$): δ = -140.94 (2F;aryl-F), -150.87 ppm (2F;aryl-F); IR: 2876, 2102, 1933, 1460, 1337, 1275, 1233, 1101, 950, 836 cm^{-1}.

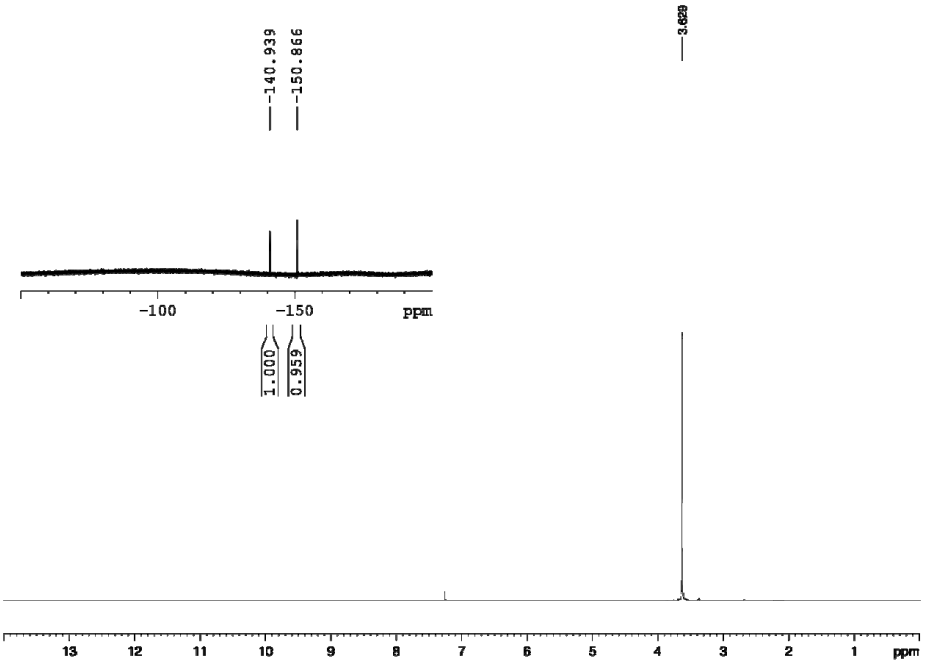

Figure 4.2. ^{1}H NMR spectrum of PFPA-PEG_{5000} (^{19}F NMR inset).

4.2.4 Synthesis of PFPA-PEG$_{1000}$

H_2N-PEG_{1000} (820 mg, 0.82 mmol) was dissolved in 10 mL of $CHCl_3$. *N*-hydroxysuccinimidyl 2,3,5,6-tetrafluorobenzoate (302 mg, 0.91 mmol) was added to the solution and the reaction was allowed to stir in the dark overnight at room temperature. The resulting solution was poured into 20 mL of diethyl ether and the product was extracted 3 times with 20 mL DI water. A white wax (981 mg, 0.8 mmol, yield: 97%) was obtained via evaporation under reduced pressure and stored in a dessicator in the dark before use. ^{1}H NMR (300 MHz, $CDCl_3$, TMS): δ = 3.64 (m, O-CH_2), 3.38 (m, N-CH2), 2.72 ppm (s, O-CH_3) ^{19}F NMR (300 MHz, $CDCl_3$, $CFCl_3$): δ = -140.94 (2F, aryl-F), -150.87 ppm (2F, aryl-F); IR: 2860, 2120, 1714, 1484, 1342, 1276, 1210, 1090, 990, 940, 839 cm^{-1}.

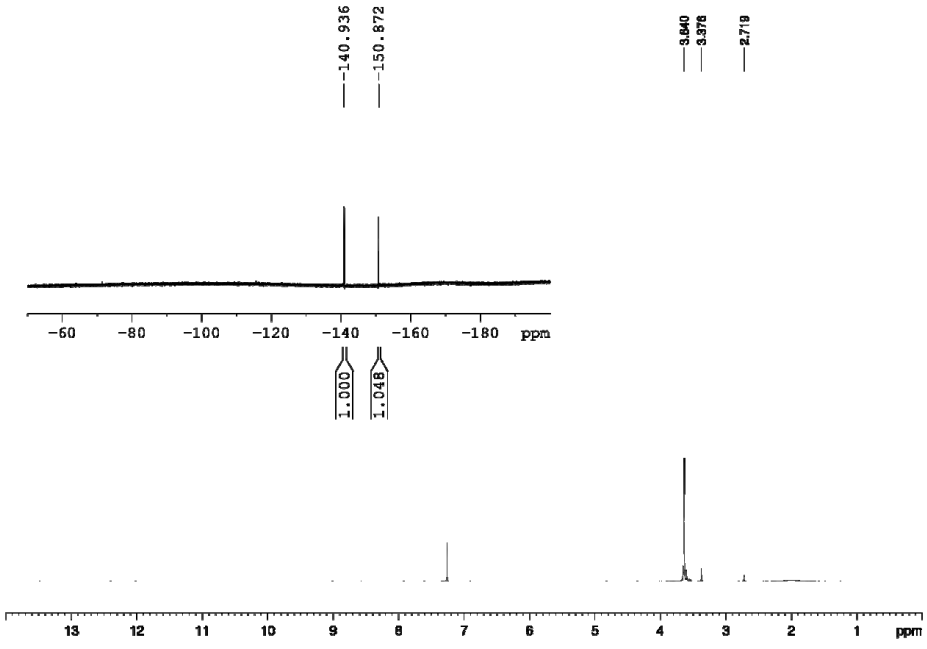

Figure 4.3. ^{1}H NMR spectrum of PFPA-PEG_{1000} (^{19}F NMR inset).

4.2.5 Synthesis of PFPA-PEG$_{550}$

H_2N-PEG_{550} (270 mg, 0.5 mmol) was dissolved in 5 mL of $CHCl_3$. *N*-hydroxysuccinimidyl 2,3,5,6-tetrafluorobenzoate (180 mg, 0.54 mmol) was added to the solution and the reaction was allowed to stir in the dark overnight at room temperature. The resulting solution was poured into 20 mL of diethyl ether and the product was extracted 3 times with 20 mL DI water. A light yellow oil (373 mg, 0.47 mmol, yield: 94%) was obtained via evaporation under reduced pressure and stored in a dessicator in the dark before use. ^{1}H NMR (300 MHz, $CDCl_3$, TMS): δ = 3.68 (m, O CH_2), 3.42 (m, N-CH_2), 2.77 ppm (s, O-CH_3) ^{19}F NMR (300 MHz, $CDCl_3$, $CFCl_3$): δ = 140.92 (2F;aryl-F), -150.79 ppm (2F;aryl-F); IR: 2861, 2122, 1771, 1482, 1316, 1254, 1205, 1085, 988, 821 cm^{-1}.

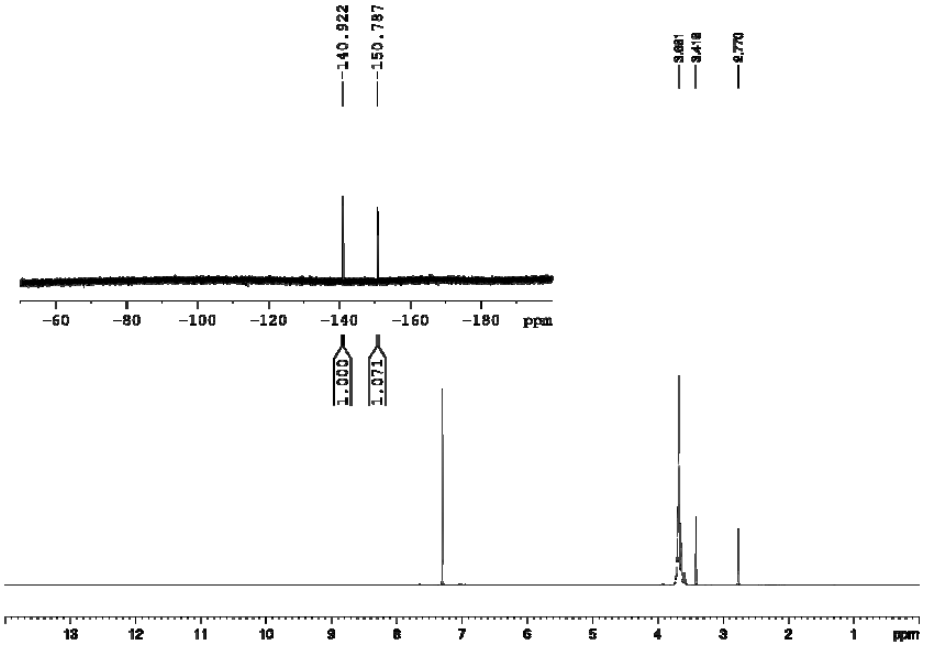

Figure 4.4. ^{1}H NMR spectrum of PFPA-PEG_{550} (^{19}F NMR inset).

4.2.6 Membrane characterization

3 x 1 cm membrane coupons used for FT-IR, contact angle measurements, and XPS were dried before use overnight in a dessicator. The modified and unmodified membranes were characterized with ATR-IR on a JASCO FT/IR-6300 spectrometer with an ATR accessory. An analytical sample used for XPS was dipped in a 2 mM solution containing 4-azido-2,3,5,6,-tetrafluorobenzoic acid[1] in methanol and allowed to air dry. After exposure to UV light for 3 min, the sample was rinsed in a methanol bath, stored in a water bath and dried in a dessicator before use. XPS studies were carried out on a Kratos AXIS Ultra DLD with a monochromatic Al Kα x-ray source operating at 10 mA and 15 kV. Survey spectra and individual high-resolution spectra were collected using pass energies of 160 eV and 10 eV, respectively. Data processing were performed using CasaXPS 2.3 software, and spectral binding energies were calibrated by assigning the hydrocarbon peak in the C 1s high-resolution spectra to 284.6 eV. Sessile drop contact angle measurements were observed using a First 10 Ångstroms Contact Angle Goniometer.

4.2.7 Surface modification procedure

2×10^{-3} M PFPA-PEG_n solution was prepared by dissolving PFPA-PEG_n in 18 MΩ water and shaking vigorously until the PFPA-PEG was fully dissolved. All dip-coating solutions were used the same day as prepared. The commercial reverse osmosis membrane coupons (2×2 cm^2) were dipped into the solutions for ~5 s

and allowed to air dry on a flat surface. Larger 110 cm^2 samples were used for performance testing. Once dried, the coupons were placed under a 6 W Spectroline ENF-260C handheld UV lamp using a 254 nm wavelength for 3 min. The lamp was held 5 inches above the surface of the membrane using a ring stand. The average UV intensity was determined using a UV-C light meter (Sper Scientific). After UV exposure, the membrane cutouts were placed in a 10% ethanol/water bath stream to remove by-products and any unreacted azide. The ethanolic solution also helped to restore permeability to the membranes that was lost during the drying step.[31] The membrane coupons were then placed in a DI water bath overnight. Membrane coupons used for ATR-IR and contact angle measurements were stored in a dessicator.

4.2.8 Water permeability and rejection

Performance testing on the RO membranes was conducted in a stainless-steel dead-end filtration stirred cell (Sterlitech Corp., Kent, WA) with an active membrane area of approximately 110 cm^2. The stirred cell was filled with Milli-Q water, and pressurized until water flow through the membrane was first observed. The water flow rate was then recorded using a digital flow meter (FlowCal 5000, Tovatech LLC, South Orange, NJ). The system was continually pressurized at increments of 50 psi (689 kPa) up to 400 psi (2758 kPa) while measuring the water flow rate at each increment. The membrane was then allowed to compact at 400 psi until the flow rate stabilized, which took

approximately 3 hours for each membrane. The salt rejection of each membrane was characterized by filling the stirred cell with a 2 g/L NaCl solution and pressurizing the cell to 225, 300 and 400 psi. Approximately 10 mL of the permeate solution was collected at each pressure and the conductivity was measured using a calibrated conductivity meter (Accumet XL30, Fisher Scientific). The salt rejection, R, was calculated by $R = 1 - c_p/c_b$, where c_p is the permeate concentration and c_b is the bulk feed solution concentration. The pure water permeability was determined from the slope of the linear regression line on the plot of membrane water flux (flow rate normalized by membrane area) against the pressure up to 400 psi after compaction.

4.2.9 Cell adhesion tests

Adhesion tests were performed for the membranes following a modified procedure reported by Gleason and co-workers.[19] *Escherichia coli* was used as the model bacteria for this test. Pure bacterial cell cultures were suspended in Luria-Bertani (LB) broth and grown at 35 °C while being shaken at 150 rpm and incubated until a mid-exponential phase was reached, at which time the cells were harvested by centrifugation at 3800×g for 8 min. The cells were then re-suspended with fresh LB medium to a concentration of 4×10^7 cells/mL. Membrane coupons, of approximately 1 cm^2, were incubated in this bacterial suspension for 24 hr at 25 rpm and 35 °C. The coupons were then removed from the suspension and gently rinsed with fresh LB broth using a Pasteur pipette.

Once rinsed, the coupons were immersed in a dye solution (SYTO 9 live/dead Baclight Bacterial Viability Kit L13152, Molecular Probes) for 15 min. The SYTO 9 solution was prepared by dissolving the contents of component A of the kit in 30 mL of sterile distillated water. After the staining was complete, the coupons were gently rinsed with fresh LB broth and imaged using a microscope (Olympus BX51 microscope) equipped with a fluorescent lamp, green/red fluorescence filters, and a 4x CCD camera attachment (FVIEW-II, Soft Imaging System, USA). Surface coverage estimates were calculated using ImageJ software.[32]

4.3 Results and discussion

To test if PFPA photochemical reactions can covalently modify RO membranes, commercial PA membrane cutouts were dipped into aqueous solutions containing PFPA-PEG_{550}, PFPA-PEG_{1000}, and PFPA-PEG_{5000} and allowed to air dry under ambient conditions. Once dried, the coupons were irradiated with low-power UV light (254 nm, 585 μW cm^{-2} average intensity) from a handheld UV lamp. The cutouts were rinsed in a water bath to remove any unreacted azide and dimerized byproducts from the surface and dried before surface analysis (Figure 4.5).

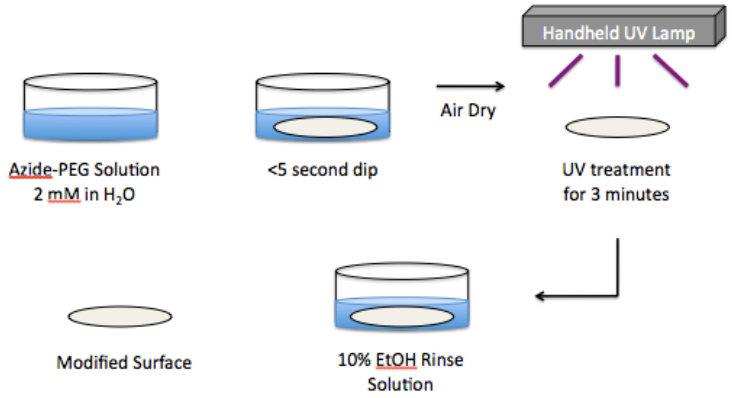

Figure 4.5. Dip-coating and modification of commercial membrane coupons with UV light.

The membranes were then characterized with attenuated total reflectance infrared (ATR-IR) spectroscopy. The presence of alkane groups within the PEG polymer brushes is discernible in the ATR-IR spectrum when compared with a bare PA membrane (Figure 4.6). A broad C–H stretch is observed at 2860 cm^{-1} and becomes stronger when PFPA-PEG of higher molecular weight is used for the modification.

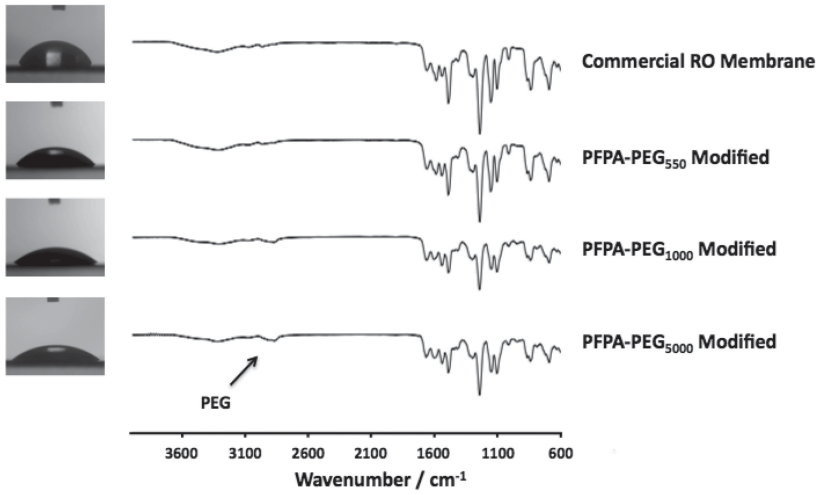

Figure 4.6. ATR-IR spectroscopy of the commercial polyamide RO membrane and modified membranes. Apparent contact angle images are shown in the photos on the left.

The modification is further manifested through contact angle measurements shown in the photos in Figure 4.7. The introduction of hydrophilic brush polymers to the surface of the membrane reduces the liquid/solid interfacial energy between a drop of water and the top PA layer. The hydrophilic surface has a stronger interaction with water than the bare membrane, resulting in a decreased contact angle. A bare commercial membrane was also dried and exposed to UV light (no dip-coating) to confirm that the decreased contact angle was not caused by UV irradiation.

The contact angle was also measured as a function of UV exposure time to investigate modification completion. Several 4 cm^2 membrane cutouts were dip coated in PFPA-PEG_{5000}, exposed to UV light for different lengths of time, and rinsed. The results, shown in Figure 4.7, indicate that the modification is complete after ~60 s of UV exposure time.

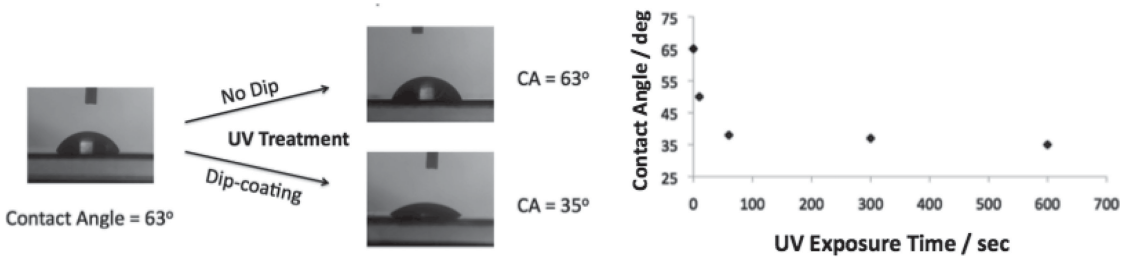

Figure 4.7. Effect of UV exposure on a bare membrane and PFPA-PEG_{5000}-coated membrane (left) and contact angle versus UV exposure time for a PFPA-PEG_{5000}-coated membrane (right).

It is also important to note that with zero UV exposure time, the contact angle of the bare commercial membrane is restored at 63°. This indicates that the wash step removes essentially all the physically adsorbed PFPA-PEG from the surface

of the membrane. Thus, UV exposure is necessary to generate covalent interactions between the RO membrane surface and the PFPA functionality.

X-ray photoelectron spectroscopy (XPS) was employed to further elucidate the nature of the covalent attachment of PFPA to the surface of the RO membrane. Because the long-PEG polymer chains dominate the XPS spectra, the small molecule 4-azidotetrafluorobenzoic acid (PFPACOOH) was prepared and used to modify analytical samples (Figure 4.5) for XPS measurements, as shown in Figure 4.8. When compared with the unmodified membrane, the N 1s spectrum for the modified membrane exhibits an additional peak at 402.2 eV, attributed to the newly formed aziridine linkage between the PFPA and the aromatic rings on the membrane surface.[24] Furthermore, the absence of signal above 403 eV indicates that N_2 is expelled from Ar–N=N$^+$=N$^-$ during irradiation, as Ar–N=N$^+$=N$^-$ exhibits a distinct peak at 406.5 eV. Additionally, the modified membrane survey spectrum reveals the presence of fluorine at 687.6 eV.

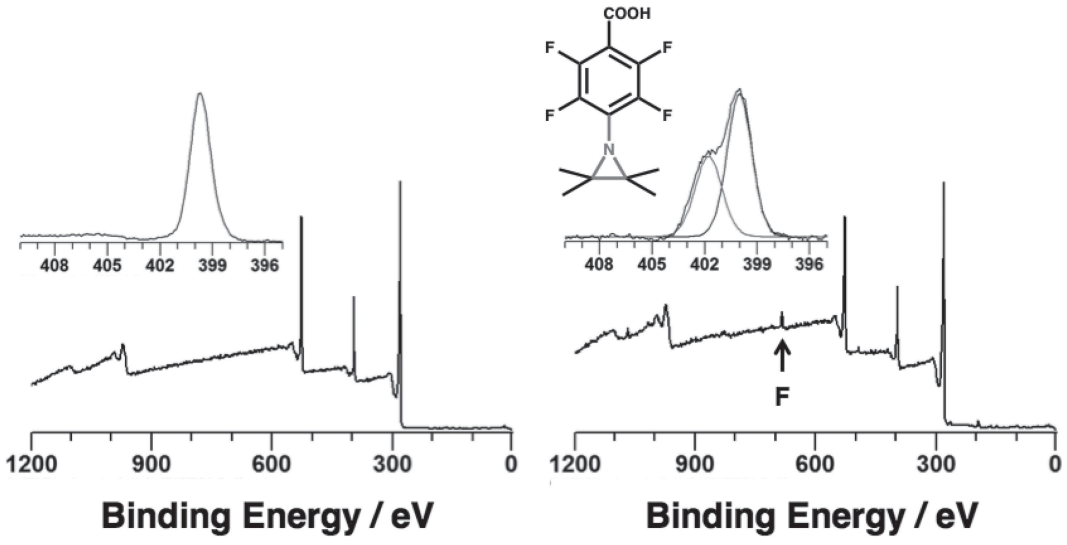

Figure 4.8. XPS survey spectra and N 1s spectra (inset) of the unmodified (left) and modified (right) RO membrane surfaces.

To determine the effect of the surface modification on the performance of commercial RO membranes, pure water permeability tests and NaCl rejection tests of the modified membranes were conducted. As shown in Figure 4.9A, the addition of hydrophilic polymers to the membrane surface reduces the pure water permeability and increases NaCl rejection due to steric hindrance.[33] Moreover, systematically increasing the molecular weight of the brush polymer has a greater effect on the permeability and rejection, presumably caused by larger flexible polymer chains. Although the initial permeability is reduced by the attachment of hydrophilic polymers, the PFPA-PEG-modified membranes exhibit higher fluxes than many commercially available RO membranes with comparable monovalent salt rejection.[34]

The ability of the modified membrane to resist cell adhesion was challenged using *Escherichia coli*, a gram-negative bacterium that is commonly used in antifouling experiments.[19,35-37] Because initial attachment of bacteria is crucial in biofilm formation, inhibiting bacterial adhesion prevents the growth and spreads of bacteria across a surface. In this study, we measured *E. coli* adhesion on the modified and unmodified RO membranes by fluorescent microscopy, following a modified procedure described by Rong and Gleason.[19] Using ImageJ software,[38] we estimated the surface coverage percentage of the adhered bacteria and compared these values to the unmodified RO membrane.

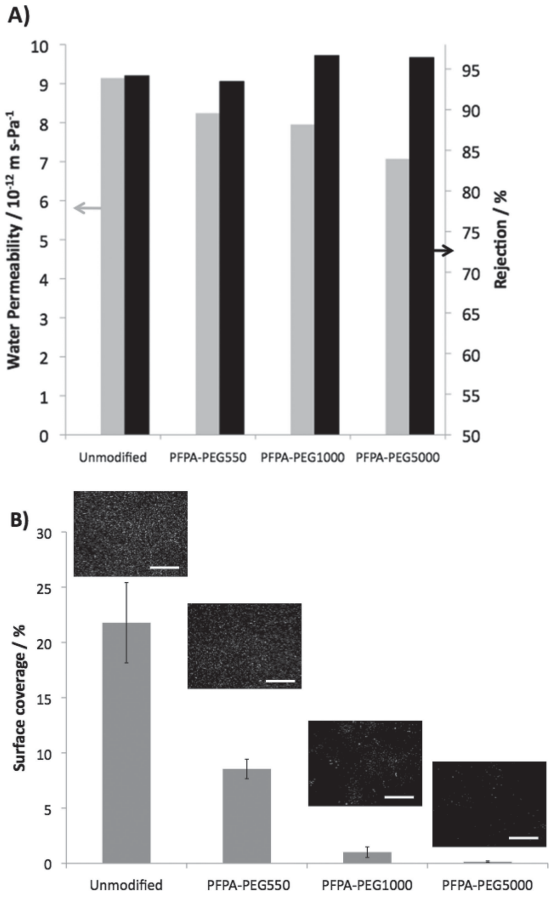

Figure 4.9. A) Pure water permeability (left axis) and rejection of NaCl (right axis). B) Observed adhesion of *E. coli* onto PFPA-PEG-modified membranes. Scale bar = 50 μm.

Figure 4.9B presents the surface coverage analysis and fluorescent microscopy images (inset). Regarding the unmodified RO membrane, ~22% of the membrane surface is covered with irreversibly attached *E. coli*. When modified with PFPA-PEG_n derivatives, notably less attachment is observed for the membranes. The membranes modified with PFPA-PEG_{550} and PFPA-PEG_{1000} showed less adhered bacteria and <1% of the surface is covered with *E. coli* on the membranes modified with PFPA-PEG_{5000}. Clearly, increased PEG molecular weight

(chain length) is directly related to the antifouling ability of the modified membrane.

4.4 Conclusions

Here, we have demonstrated the scalable surface modification of a commercial RO membrane consistent with the roll-to-roll processing of RO membranes. Utilizing the photochemistry of PFPAs as a platform, our system modifies RO membranes under ambient conditions, with minute modification times, using a dip-coating technique in environmentally benign solvents. By modifying a commercial RO membrane with our method, we prevent initial bacterial adhesion that leads to biofilm formation. We believe that the production of antifouling RO membranes will reduce or eliminate biofouling on RO membranes, thus reducing the high maintenance and energy costs associated with current RO desalination. In the future, we will examine the modification of RO membranes with PFPAs bearing small molecule functionalities with our process.

4.5 Acknowledgments

This work was supported by the NSF SUSchem grant CBET 1337065 (E.M.V and R.B.K.). The authors would also like to thank Dow Water Process and Solutions for their generous donation of RO XLE flat sheet membranes.

References

(1) World Health Organization, Progress on Sanitation and Drinking-Water, WHO Press, Geneva **2013**.

(2) Shannon, M. A.; Bohn, P. W.; Elimelech, M.; Georgiadis, J. G.; Marinas, B. J.; Mayes, A. M. Science and technology for water purification in the coming decades. *Nature* **2008**, 452, 301–310.

(3) Elimelech, M.; Phillip, W. A. The future of seawater desalination: Energy, technology, and the environment. *Science* **2011**, 333, 712–717.

(4) Service, R. F. Desalination freshens up. *Science* **2006**, 313, 1088–1090.

(5) Lee, K. P.; Arnot, T. C.; Mattia, D. A review of reverse osmosis membrane materials for desalination—Development to date and future potential. *J. Memb. Sci.* **2011**, 370, 1–22.

(6) Herzberg, M.; Elimelech, M. Biofouling of reverse osmosis membranes: Role of biofilm-enhanced osmotic pressure. *J. Memb. Sci.* **2007**, 295, 11–20.

(7) Glater, J.; Hong, S.; Elimelech, M. The search for a chlorine-resistant reverse osmosis membrane. *Desalination* **1994**, 95, 325–345.

(8) Kawaguchi, T.; Tamura, H. Chlorine-resistant membrane for reverse osmosis. I. Correlation between chemical structures and chlorine resistance of polyamides. *J. Appl. Polym. Sci.* **1984**, 29, 3359–3367.

(9) Isaias, N. P. Experience in reverse osmosis pretreatment. *Desalination* **2001**, 139, 57–64.

(10) Redondo, J. A. Brackish-, sea- and wastewater desalination. *Desalination* **2001**, 138, 29–40.

(11) Kang, G.-D.; Gao, C.-J.; Chen, W.-D.; Jie, X.-M.; Cao, Y.-M.; Yuan, Q. Study on hypochlorite degradation of aromatic polyamide reverse osmosis membrane. *J. Memb. Sci.* **2007**, 300, 165–171.

(12) Rana, D.; Matsuura, T. Surface modifications for antifouling membranes. *Chem. Rev.* **2010**, 110, 2448–2471.

(13) Kang, G.; Cao, Y. Development of antifouling reverse osmosis membranes for water treatment: A review. *Water Res.* **2012**, 46, 584–600.

(14) Belfer, S.; Purinson, Y.; Fainshtein, R.; Radchenko, Y.; Kedem, O. Surface modification of commercial composite polyamide reverse osmosis membranes. *J. Memb. Sci.* **1998**, 139, 175–181.

(15) Van Wagner, E. M.; Sagle, A. C.; Sharma, M. M.; La, Y.-H.; Freeman, B. D. Surface

modification of commercial polyamide desalination membranes using poly(ethyleneglycol) diglycidyl ether to enhance membrane fouling resistance. *J. Memb. Sci.* **2011**, 367, 273–287.

(16) Kang, G.; Yu, H.; Liu, Z.; Cao, Y. Surface modification of a commercial thin film composite polyamide reverse osmosis membrane by carbodiimide-induced grafting with poly(ethylene glycol) derivatives. *Desalination* **2011**, 275, 252–259.

(17) Zou, L.; Vidalis, I.; Steele, D.; Michelmore, A.; Low, S. P.; Verberk, J. Q. J. C. Surface hydrophilic modification of RO membranes by plasma polymerization for low organic fouling. *J. Memb. Sci.* **2011**, 369, 420–428.

(18) Lin, N. H.; Kim, M.; Lewis, G. T.; Cohen, Y. Polymer surface nano-structuring of reverse osmosis membranes for fouling resistance and improved flux performance. *J. Mater. Chem.* **2010**, 20, 4642.

(19) Yang, R.; Xu, J.; Ozaydin-Ince, G.; Wong, S. Y.; Gleason, K. K. Surface-tethered zwitterionic ultrathin antifouling coatings on reverse osmosis membranes by initiated chemical vapor deposition. *Chem. Mater.* **2011**, 23, 1263–1272.

(20) Banerjee, I.; Pangule, R. C.; Kane, R. S. Antifouling coatings: Recent developments in the design of surfaces that prevent fouling by proteins, bacteria, and marine organisms. *Adv. Mater.* **2011**, 23, 690–718.

(21) Leyva, E.; Young, M. J. T.; Platz, M. S. High yields of formal CH insertion products in the reactions of polyfluorinated aromatic nitrenes. *J. Am. Chem. Soc.* **1986**, 108, 8307–8309.

(22) Liu, L.-H.; Yan, M. Perfluorophenyl azides: New applications in surface functionalization and nanomaterial synthesis. *Acc. Chem. Res.* **2010**, 43, 1434–1443.

(23) Liu, L.-H.; Yan, M. Simple method for the covalent immobilization of graphene. *Nano Lett.* **2009**, 9, 3375–3378.

(24) Liu, L.-H.; Zorn, G.; Castner, D. G.; Solanki, R.; Lerner, M. M.; Yan., M. A simple and scalable route to wafer-size patterned graphene. *J. Mater. Chem.* **2010**, 20, 5041–5046.

(25) Pastine, S. J.; Okawa, D.; Kessler, B.; Rolandi, M.; Llorente, M.; Zettl, A.; Fréchet, J. M. J. A facile and patternable method for the surface modification of carbon nanotube forests using perfluoroarylazides. *J. Am. Chem. Soc.* **2008**, 130, 4238–4239.

(26) Yan, M.; Cai, S. X.; Keana, J. F. W. Photochemical and thermal reactions of C60 with N-succinimidyl 4-azido-2,3,5,6-tetrafluorobenzoate: A new method for functionalization of C60. *J. Org. Chem.* **1994**, 59, 5951–5954.

(27) Bartlett, M. A.; Yan, M. Fabrication of polymer thin films and arrays with spatial and topographical controls. *Adv. Mater.* **2001**, 13, 1449–1451.

(28) Morawietz, J.; Sander, W. Photochemistry of fluorinated phenyl nitrenes: Matrix isolation of fluorinated azirines. *J. Org. Chem.* **1996**, 61, 4351–4354.

(29) Poe, R.; Schnapp, K.; Young, M. J. T.; Grayzar, J.; Platz, M. S. Chemistry and kinetics of singlet pentafluorophenylnitrene. *J. Am. Chem. Soc.* **1992**, 114, 5054–5067.

(30) Keana, J. F. W.; Cai, S. X. New reagents for photoaffinity labeling: Synthesis and photolysis of functionalized perfluorophenyl azides. *J. Org. Chem.* **1990**, 55(11), 3640–3647.

(31) Louie, J. S.; Pinnau, I.; Reinhard, M. Effects of surface coating process conditions on the water permeation and salt rejection properties of composite polyamide reverse osmosis membranes. *J. Memb. Sci.* **2011**, 367, 249–255.

(32) Abramoff, M. D.; Magalhaes, P. J.; Ram, S. J. Image processing with ImageJ. *Biophotonics Int.* **200**4, 11, 36.

(33) Cohen, Y.; Lin, N.; Varin, K. J.; Chien, D.; Hicks, R. F. Membrane surface nanostructuring with terminally anchored polymer chains, in *Functional Nanostructured Materials and Membranes for Water Treatment* (Eds: Duke, M.; Zhao, D.; Semiat, R.), Wiley-VCH Verlag GmbH & Co. KGaA, Weinheim, Germany **2013**, p. 85.

(34) Jeong, B.-H.; Hoek, E. M. V; Yan, Y.; Subramani, A.; Huang, X.; Hurwitz, G.; Ghosh, A. K.; Jawor, A. Interfacial polymerization of thin film nanocomposites: A new concept for reverse osmosis membranes. *J. Memb. Sci.* **2007**, 294, 1–7.

(35) Adout, A.; Kang, S.; Asatekin, A.; Mayes, A. M.; Elimelech, M. Ultrafiltration membranes incorporating amphiphilic comb copolymer additives prevent irreversible adhesion of bacteria. *Environ. Sci. Technol.* **2010**, 44, 2406–2411.

(36) Kim, S. H.; Kwak, S.-Y.; Sohn, B.-H.; Park, T. H. Design of TiO_2 nanoparticle self-assembled aromatic polyamide thin-film-composite (TFC) membrane as an approach to solve biofouling problem. *J. Memb. Sci.* **2003**, 211, 157–165.

(37) Tan, K.; Obendorf, S. K. Fabrication and evaluation of electrospun nanofibrous antimicrobial nylon 6 membranes. *J. Memb. Sci.* **2007**, 305, 287–298.

(38) Yan, M. Covalent functionalization of natural rubber latex. *React. Funct. Polym.* **2000**, 45, 137–144.

CHAPTER 5

Low-Fouling Antibacterial Reverse Osmosis Membranes via Surface Grafting of Graphene Oxide

5.1 Background

The dwindling of reliable freshwater supplies is one of our most severe problems exacerbated by rising population and source contamination.[1–3] Although there have been improved efforts in water conservation, infrastructure repair, and allocation, these approaches are only effective in making better use of existing resources.[2] With the increasing need for more freshwater, it is imperative to find alternative sources to meet future demand. Membrane desalination can produce a sustainable supply of freshwater from both seawater and brackish water utilizing reverse osmosis (RO) membranes. The thin-film membranes reject salts from the feed solution and continuously produce a freshwater effluent for use. State-of-the-art, interfacially polymerized RO membranes provide high permeability and high rejection with relatively low manufacturing costs.[2,3] Despite their outstanding transport and selectivity, their susceptibility to fouling remains one of the most problematic issues causing reduced performance and increased energy consumption.[4,5] Fouling occurs when proteins, microorganisms, and inorganic materials accumulate on the membrane surface and increase its resistance to water permeation.[6,7] Of these, biofouling caused by the deposition and growth of microorganisms, is the most difficult to prevent.[5,7–9] Once microorganisms irreversibly attach to the surface of a membrane, they can proliferate rapidly in the presence of nutrients, creating microcolonies that produce extracellular polymeric substances (EPS) that eventually lead to the formation of biofilms on the membrane surface. Unfortunately, chlorine-based disinfecting agents that are generally used to

control biofouling are not suitable for cleaning RO membranes due to chlorine degradation of polyamide-based polymers.[10]

Methods that have been investigated to introduce anti-adhesion/antimicrobial properties to polyamide RO membranes include the surface coating of hydrophilic functional materials[11–16] and the incorporation of biocidal materials[8,19,20,22] directly onto the polymer surfaces. A hydrophilic surface will form a hydration layer that hinders the hydrophobic interactions between the membrane surfaces and the foulants, preventing the initial attachment of foulants on the membranes.[19] However, most of the modification methods are not practical or scalable and therefore are unlikely to be of commercial importance.

Physically applied coatings, for example, can be easily removed during membrane operation and only produce short-term antifouling effects.[7] Layer-by-layer (LBL) coatings of oppositely charged materials tend to disintegrate under high/low pH and/or high ionic strength[20] which are environments often encountered during RO applications. Covalent tethering of hydrophilic materials maintains the stability of the modification layer; however, these modifications typically require exotic synthetic conditions such as radical-initiated polymerization,[19] plasma,[15] or carbodiimide activation,[8,11,12] which have only been demonstrated on a laboratory scale. Such processes tend not to be amenable to the high-rate roll-to-roll manufacturing processes used for commercial RO membranes.[23] Furthermore, the grafting layer often reduces the permeability of

the membranes by adding resistance to the passage of water through the membrane.[12,13,15,21] The modification of RO membranes with biocidal materials can increase their antimicrobial properties and biofouling resistance. However, commonly used materials such as silver nanoparticles will slowly leach out of the membrane, spreading toxic nanoparticles into the environment, while losing antimicrobial activity over time.[8] Therefore, a facile, scalable process is needed to produce antifouling RO membranes which in turn will improve the productivity of membrane-based desalination.

In this chapter, we investigate grafting graphene oxide (GO) onto commercial polyamide RO membranes to promote antifouling and antiadhesion properties. GO is a hydrophilic, one-atom-thick, two-dimensional structure[11,22] that possesses antimicrobial properties.[8,22] Previous research has examined applying the outstanding properties of GO in the RO membrane field through the incorporation of GO into the polyamide active layer,[17,18] LBL coating of GO dispersions,[11] and covalent surface bonding of GO using carbodiimide activation.[8,16,22] The covalent surface bonding method appears to be the best method because it allows full utilization of GO material[18] and is more environmentally stable.[20]

5.2 Results and Discussion

5.2.1 Synthesis of azide-functionalized GO

Azide-functionalized GO (AGO) was employed to modify commercial RO membranes due to the unique photochemistry of azide groups. Upon photoactivation, AGO produces a highly reactive singlet nitrene intermediate that reacts with the abundant aromatic rings found within the polyamide membrane active layer.[25,26] The full reaction scheme is outlined in Figure 5.1. AGO was synthesized according to the route developed by Eigler *et al.*[24] Sodium azide was added into an aqueous dispersion of GO followed by freeze-drying. The solid-state azidation reaction takes place during the drying in which azide groups substitute for the sulfonate and epoxide groups (Figure 5.2). The as-synthesized product was purified by centrifugation in water. The final product was then freeze-dried and redispersed in water to make a 10 mg/L AGO dispersion. Atomic force microscopy (AFM) analysis (Figure 5.3) showed that the as-synthesized AGO nanosheets have sizes ranging from several hundred nanometers to several micrometers with an average thickness of 1.15 nm. This is comparable to previously reported values.[29] Commercial RO polyamide membranes (Dow FILMTEC XLE brackish water flat sheet membranes) were dipped into the AGO dispersion and air-dried overnight under ambient conditions. The RO membranes were then placed under UV irradiation (254 nm, 620 $\mu W/cm^2$ average intensity) for 1 minute before sonication in DI water, removing any remaining non-bonded AGO.

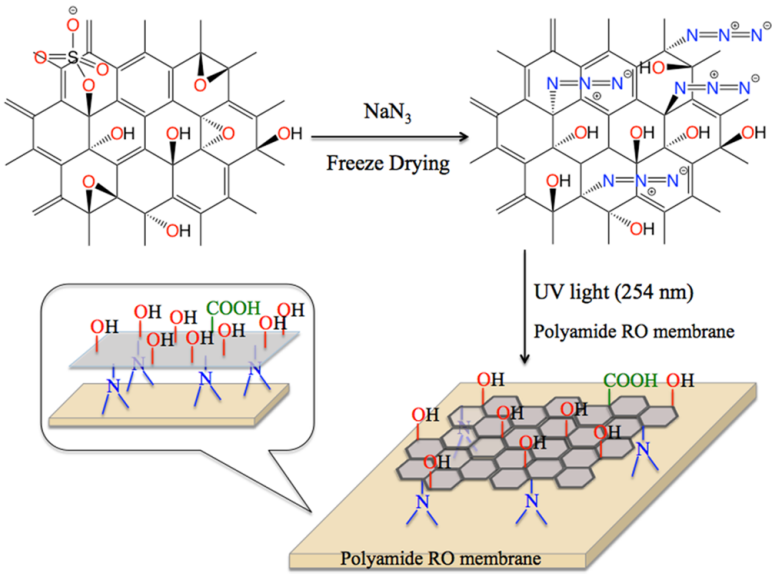

Figure 5.1. Synthesis of azide functionalized graphene oxide (AGO) and its attachment onto a polyamide RO membrane surface via UV activation of azide functional groups.

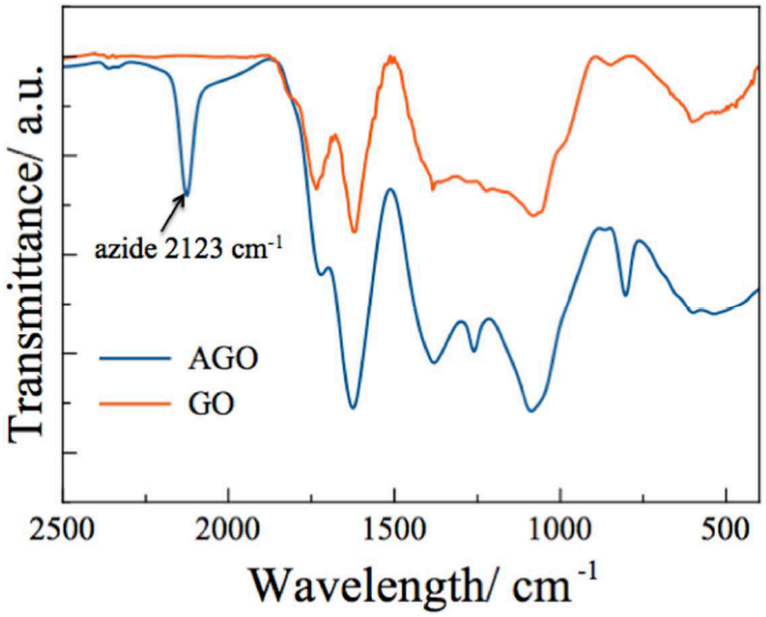

Figure 5.2. FT-IR spectra of GO and AGO show that after the azidation reaction, a new azide peak (2123 cm^{-1}) is observed in the AGO spectrum. This provides evidence for the successful bonding of azide groups onto the GO backbone.

Contact angle measurements were conducted to confirm the completion of the modification (Figure 5.4a). Once commercial RO membranes were modified, the apparent pure water contact angle decreased from 85° ± 4° (comparable to previously reported values for polyamide RO membranes[11,17]) to 45° ± 2°, indicating a much higher affinity between water and the membrane surface due to the hydrophilic oxygen-containing functional groups within the AGO structure. The enhanced hydrophilicity induces a thin hydration layer on the membrane surfaces which repels foulant adsorption.[5,7]

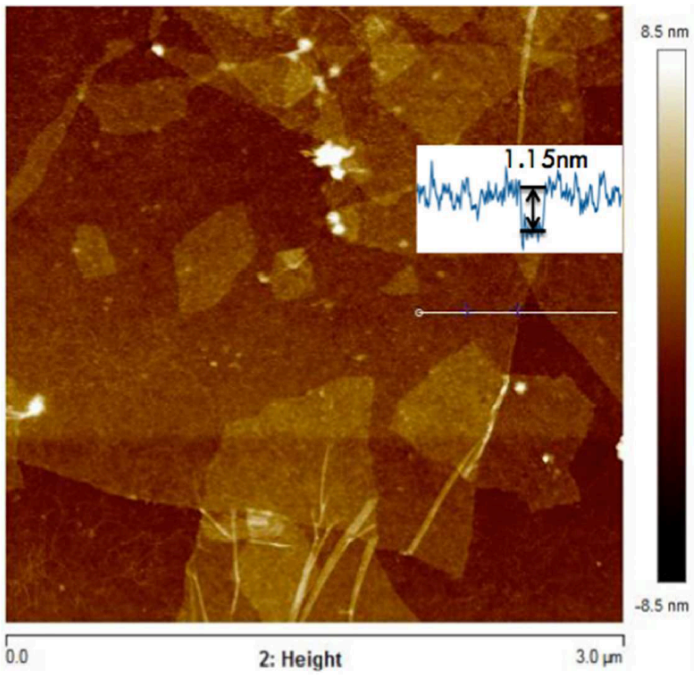

Figure 5.3. AFM height analysis of AGO shows that AGO exhibits a planar morphology with an average thickness of 1.15 nm (inset).

Commercial RO membranes were also dried and exposed to UV light without the dip-coating step. Their contact angles did not change compared to a bare RO

membrane, indicating that UV light exposure plays little role in the contact angle of the polyamide layer, as previously demonstrated.[23] As another control experiment, an AGO-coated RO membrane was dried and sonicated in DI water without UV exposure. Its contact angle showed no apparent change compared to a bare RO membrane. This proves that the sonication/rinsing step was effective in removing essentially all the non-bonded AGO.

5.2.2 X-ray photoelectron spectroscopy

X-ray photoelectron spectroscopy (XPS) analysis of the membrane surface further confirmed successful modification. Following the modification, the chemical composition of the modified membrane surface contained high carbon and oxygen content, similar to the precursor AGO powder (Table 5.1), suggesting that the modified surface was predominantly covered in GO sheets.

	% C 1s	% O 1s	% N 1s
AGO Powder	67.8	30.0	2.2
Control RO Membrane	74.6	14.5	10.9
AGO-RO Membrane	68.4	28.5	3.0

Table 5.1. XPS surface atomic composition for AGO powder and RO membranes.

The oxygen content of the modified membrane approximately doubled (from 14.5% to 28.6%) after the grafting of GO compared to the pristine membrane, a result of the various oxygen-containing functional groups in AGO. Additionally, the nitrogen content from the polyamide active layer was reduced from 10.9% to 3.0%, as GO sheets on the surface of the membrane material dominate the spectrum.

5.2.3 Atomic force microscopy

To investigate changes to the surface topography, AFM was conducted on the modified and unmodified membranes. The microscopy revealed that the GO-RO membrane had a much smoother surface compared to the unmodified RO membrane. Polyamide RO membranes are manufactured using interfacial polymerization that typically gives a rough ridge-and-valley[11,23] surface morphology, as shown in Figure 5.4b (left). After the RO membrane surface was modified with GO, the membrane surface became smoother with an arithmetic average (R_a) roughness of 29.0 nm compared to a R_a of 44.3 nm for the unmodified RO membrane. This can be attributed to the planar GO sheets (Figure 5.3) covering the valley regions of the membrane surfaces. A rough surface, like the pristine RO membrane, tends to trap foulants due to the preferential accumulation of foulants in the valleys of the membrane surface.[7] Therefore, a smooth, hydrophilic membrane surface is expected to have higher resistance to fouling compared to an unmodified RO membrane.

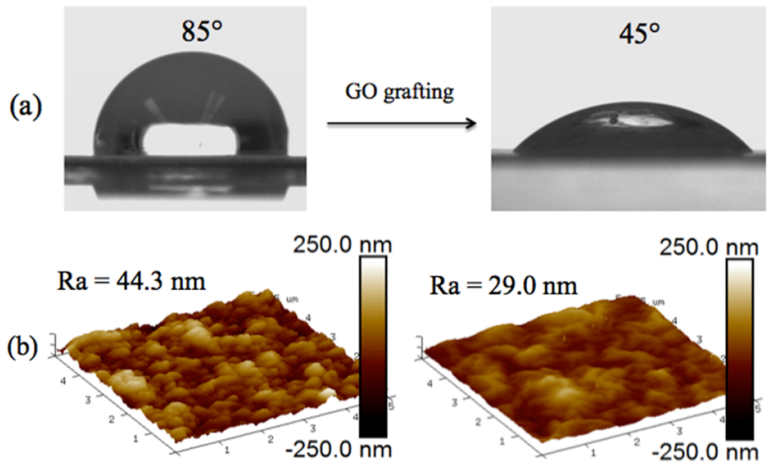

Figure 5.4. After GO grafting on the polyamide RO membrane surface, (a) the water contact angle decreased from 85° to 45° and (b) the average surface roughness decreased from 44.3 nm to 29.0 nm based on a 5 μm × 5 μm analyzed area.

5.2.4 Membrane permeability and rejection

Membrane permeability and rejection were tested with a 2 g/L NaCl aqueous solution under 15.5 bar operating pressure using a cross-flow system with an effective membrane area of 19 cm^2. After 2 h of compaction, the commercial RO membrane exhibited a stable flux of 37.8 Lmh with a NaCl rejection of 94.1%. The AGO-RO membrane maintained a comparable flux of 36.3 Lmh and NaCl rejection of 95.3%. Prior attempts to increase the hydrophilicity and fouling resistance of polyamide RO membranes via surface tethering of hydrophilic materials often resulted in significant drops in permeability.[12,13,15,21] With the AGO modification, only negligible changes to the membrane performance properties occurred.

Once the pure water permeability and rejection was established in the cross-flow system, the fouling propensity of the membranes were evaluated by

adding foulant to the feed solution. A feed solution consisting of 0.2 g/L BSA and 2 g/L NaCl was used and the flux was monitored for 7 days. The operating pressure was maintained at 15.5 bar over the course of the test. During the experiment, the flux of the unmodified RO membrane decreased rapidly, with a total of 70% flux reduction after 7 days (Figure 5.5a). In contrast, the flux of the modified membrane was consistently higher than the blank RO membrane after 5 h and demonstrated only a 40% flux reduction after 7 days. The cross-flow test was then stopped and the unmodified and modified membranes were taken out for visual comparison. After 1 week of fouling, a thick layer of yellow BSA covered the entire surface of the pristine RO membrane (Figure 3a inset), increasing the thickness of the membrane and lowering its flux.

For the modified membrane, the yellow BSA on the surface was greatly reduced and only covered the side edges of modified membrane. The much-improved hydrophilicity significantly increased the membrane's affinity for water and leads to a thin layer water barrier that is effective in resisting the irreversible fouling caused by the attachment of proteins onto the membrane surfaces. The smoother surfaces of the modified membranes further contribute to its low-fouling properties because it becomes more difficult for protein particles to anchor onto the membrane surfaces without the valleys and ridges of a rough surface that protect the protein particles from being flushed away. It is evident that after the grafting of GO the modified polyamide membrane was able to mitigate the long-term gel layer formation from the accumulation of foulant. Due to its enhanced hydrophilicity and smoothness, the GO-RO

membrane can effectively resist the attachment of foulant molecules and provide less accessible sites for foulant deposition.

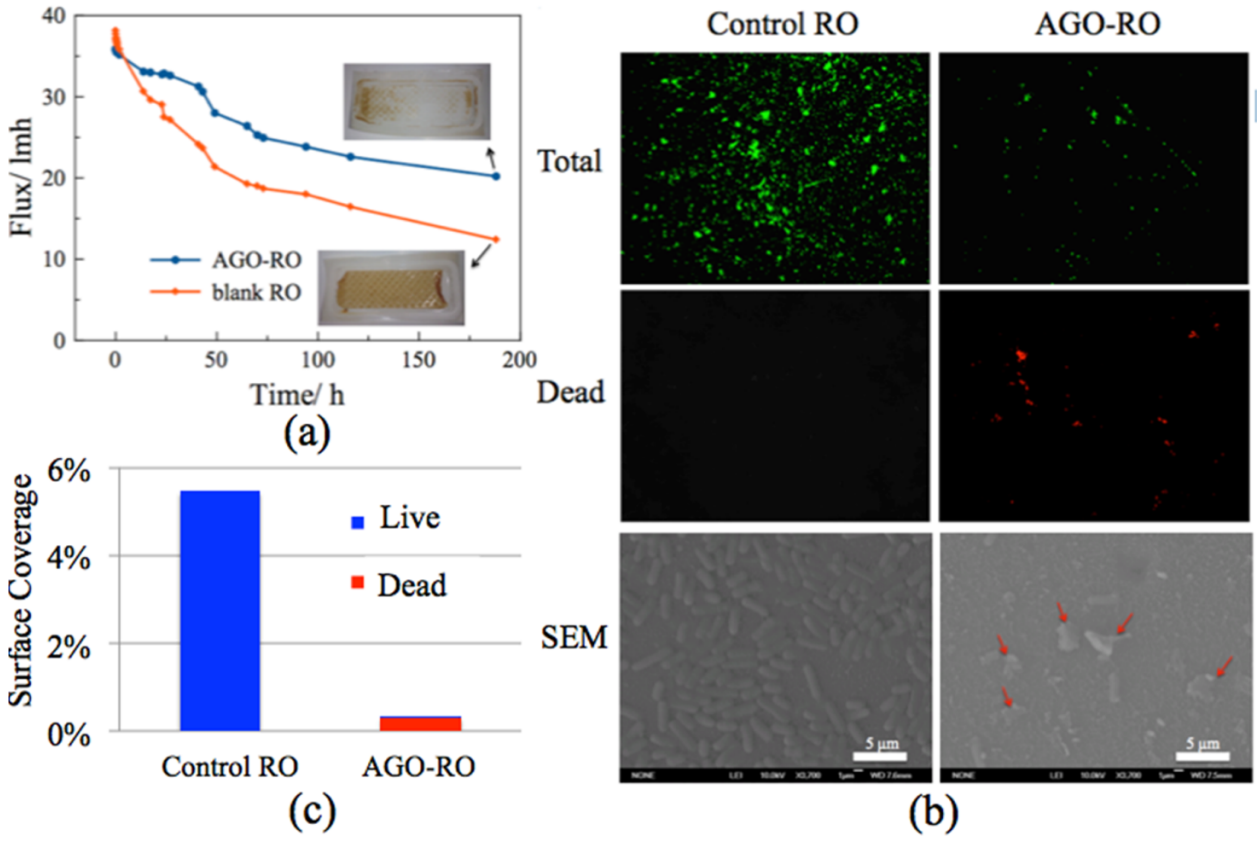

Figure 5.5. (a) Long-term BSA fouling test on the control and modified membranes showing the differences in flux decline; (b) Fluorescence and SEM images showing the percentages and condition of *Escherichia coli* cells on membrane surfaces after contact for 24 h; (c) Quantitative analysis of live (green) and dead (red) cell percentages on both membrane surfaces.

5.2.5 Bacterial adhesion

The antifouling property of GO-RO was investigated further by a static bacterial adhesion experiment using *E. coli* as a model microorganism. Modified and unmodified membrane cut-outs (1 × 1 cm^2) were soaked in an *E. coli* suspension for 24 h at room temperature before being rinsed with a 0.9% saline

solution and stained in a SYTO 9 or propidium iodide (PI) solution for fluorescence imaging. SYTO 9 labels both live and dead bacteria cells by binding to their cell membranes, whereas PI labels only the dead cells because it can only penetrate damaged cell membranes. Using ImageJ software, the surface coverage of total attached cells and dead attached cells can be quantified by dividing the number of colored pixels by the total amount of pixels in the image. Afterward, the surface coverage of live attached cells can be calculated by subtracting the percentage of dead attached cells from that of total attached cells. Figure 5.5c illustrates the surface coverage of live (blue) and dead (red) *E. coli* on both unmodified and modified membranes. 5.46% of the surface of the control RO membrane was covered by *E. coli* cells with no deactivation. In comparison, only 0.32% of the GO-RO membrane surface was fouled by *E. coli* (both live and dead species), representing a 17-fold reduction in cell adhesion compared to the unmodified RO membrane. This shows that the GO-RO membrane can effectively inhibit the initial attachment of bacteria, which is crucial in preventing the growth and spreading of bacteria. Furthermore, among the attached *E. coli* cells, nearly 90% were deactivated owing to the antibacterial properties of GO molecules.[8,22]

The bacteria-fouled membranes were also observed with scanning electron microscopy (SEM) to confirm further the condition of the *E. coli* cells on the membrane surfaces. In the SEM images, the pristine RO membrane surfaces were largely covered by intact *E. coli* cells, whereas that of the AGO-RO membrane had a much lower surface coverage of *E. coli* cells. Many of the *E. coli* cells on the AGO-

RO membrane surfaces appeared to be lysed, indicating cell damage induced by the GO molecules, as GO is known to inactivate bacteria through physical disruption,[27] formation of reactive oxygen species,[27] and extraction of lipids from cell membranes.[28]

5.3 Conclusion

By anchoring GO molecules onto the polyamide RO membrane surfaces, we have successfully altered the surface properties of a commercial polyamide RO membrane, making it more hydrophilic, smooth, and antibacterial with considerable resistance to protein fouling and biofouling.

5.4 Acknowledgments

This work was supported by the NSF SUSchem grant CBET 1337065 (E.M.V and R.B.K.). The authors thank Professor Shaily Mahendra for supplying the incubator for cultivating *E. coli* cells.

References

(1) Crittenden, J. C.; Trussell, R. R.; Hand, D. W.; Howe, K. J.; Tchobanoglous, G. *Water Treatment: Principles and Design*, 2nd ed.; John Wiley & Sons, Inc.: Hoboken, NJ, **2005**.

(2) Elimelech, M.; Phillip, W. A. The future of seawater desalination: Energy, technology, and the environment. *Science* **2011**, 333, 712–717.

(3) Service, R. F. Desalination freshens up. *Science* **2006**, 313, 1088–1090.

(4) Gao, K.; Kearney, L. T.; Wang, R.; Howarter, J. A. Enhanced wettability and transport control of ultrafiltration and reverse osmosis membranes with grafted polyelectrolytes. *ACS Appl. Mater. Interfaces* **2015**, 7, 24839–24847.

(5) Mansouri, J.; Harrisson, S.; Chen, V. Strategies for controlling biofouling in membrane filtration systems: Challenges and opportunities. *J. Mater. Chem.* **2010**, 20, 4567–4586.

(6) Huang, X.; McVerry, B. T.; Marambio-Jones, C.; Wong, M. C. Y.; Hoek, E. M. V.; Kaner, R. B. Novel chlorine resistant low-fouling ultrafiltration membrane based on a hydrophilic polyaniline derivative. *J. Mater. Chem.* A **2015**, 3, 8725–8733.

(7) Rana, D.; Matsuura, T. Surface modifications for antifouling membranes. *Chem. Rev.* **2010**, 110, 2448–2471.

(8) Perreault, F.; Tousley, M. E.; Elimelech, M. Thin-film composite polyamide membranes functionalized with biocidal graphene oxide nanosheets. *Environ. Sci. Technol. Lett.* **2014**, 1, 71–76.

(9) Khan, M. T.; de O. Manes, C.-L.; Aubry, C.; Gutierrez, L.; Croue, J. P. Kinetic study of seawater reverse osmosis membrane fouling. *Environ. Sci. Technol.* **2013**, 47, 10884–10894.

(10) Glater, J.; Hong, N.; Elimelech, M. The search for a chlorine-resistant reverse osmosis membrane. *Desalination* **1994**, 95, 325– 345.

(11) Choi, W.; Choi, J.; Bang, J.; Lee, J.-H. Layer-by-layer assembly of graphene oxide nanosheets on polyamide membranes for durable reverse-osmosis applications. *ACS Appl. Mater. Interfaces* **2013**, 5, 12510–12519.

(12) McVerry, B. T.; Wong, M. C. Y.; Marsh, K. L.; Temple, J. A. T.; Marambio-Jones, C.; Hoek, E. M. V.; Kaner, R. B. Scalable antifouling reverse osmosis membranes utilizing perfluorophenyl azide photochemistry. *Macromol. Rapid Commun.* **2014**, 35, 1528–1533.

(13) Nikkola, J.; Sievänen, J.; Raulio, M.; Wei, J.; Vuorinen, J.; Tang, C. Y. Surface modification of thin film composite polyamide membrane using atomic layer deposition method. *J. Membr. Sci.* **2014**, 450, 174–180.

(14) Lin, N. H.; Kim, M.; Lewis, G. T.; Cohen, Y. Polymer surface nano-structuring of reverse osmosis membranes for fouling resistance and improved flux performance. *J. Mater. Chem.* **2010**, 20, 4642–4652.

(15) Belfer, S.; Purinson, Y.; Fainshtein, R.; Radchenko, Y.; Kedem, O. Surface modification of commercial composite polyamide reverse osmosis membranes. *J. Membr. Sci.* **1998**, 139, 175–181.

(16) Hegab, H. M.; ElMekawy, A.; Barclay, T. G.; Michelmore, A.; Zou, L.; Saint, C. P.; Ginic-Markovic, M. Fine-tuning the surface of forward osmosis membranes via grafting graphene oxide: Performance patterns and biofouling propensity. *ACS Appl. Mater. Interfaces* **2015**, 7, 18004–18016.

(17) He, L.; Dumée, L. F.; Feng, C.; Velleman, L.; Reis, R.; She, F.; Gao, W.; Kong, L. Promoted water transport across graphene oxide-poly(amide) thin film composite membranes and their antibacterial activity. *Desalination* **2015**, 365, 126–135.

(18) Xia, S.; Yao, L.; Zhao, Y.; Li, N.; Zheng, Y. Preparation of graphene oxide modified polyamide thin film composite membranes with improved hydrophilicity for natural organic matter removal. *Chem. Eng. J.* **2015**, 280, 720–727.

(19) Banerjee, I.; Pangule, R. C.; Kane, R. S. Antifouling coatings: Recent developments in the design of surfaces that prevent fouling by proteins, bacteria, and marine organisms. *Adv. Mater.* **2011**, 23, 690–718.

(20) Ren, P.; Yang, H.; Liang, H.; Xu, X.; Wan, L.; Xu, Z. Highly stable, protein-resistant surfaces via the layer-by-layer assembly of poly(sulfobetaine methacrylate) and tannic acid. *Langmuir* **2015**, 31, 5851–5858.

(21) Faibish, R. S.; Yoshida, W.; Cohen, Y. Contact angle study on polymer-grafted silicon wafers. *J. Colloid Interface Sci.* **2002**, 256, 341–350.

(22) Ray, J. R.; Tadepalli, S.; Nergiz, S. Z.; Liu, K.; You, L.; Tang, Y.; Singamaneni, S.; Jun, Y. Hydrophilic, bactericidal nanoheater-enabled reverse osmosis membranes to improve fouling resistance. *ACS Appl. Mater. Interfaces* **2015**, 7, 11117–11126.

(23) Ghosh, A. K.; Jeong, B.; Huang, X.; Hoek, E. M. V. Impacts of reaction and curing conditions on polyamide composite reverse osmosis membrane properties. *J. Membr. Sci.* **2008**, 311, 34–45.

(24) Eigler, S.; Hu, Y.; Ishii, Y.; Hirsch, A. Controlled functionalization of graphene oxide with sodium azide. *Nanoscale* **2013**, 5, 12136–12139.

(25) Bräse, S.; Gil, C.; Knepper, K.; Zimmermann, V. Organic azides: An exploding diversity of a unique class of compounds. *Angew. Chem., Int. Ed.* **2005**, 44, 5188–5240.

(26) Liu, L.; Yan, M. Perfluorophenyl azides: New applications in surface functionalization and nanomaterial synthesis. *Acc. Chem. Res.* **2010**, 43, 1434–1443.

(27) Liu, S.; Zeng, T. H.; Hofmann, M.; Burcombe, E.; Wei, J.; Jiang, R.; Kong, J.; Chen, Y. Antibacterial activity of graphite, graphite oxide, graphene oxide, and reduced graphene oxide: Membrane and oxidative stress. *ACS Nano* **2011**, 5, 6971–6880.

(28) Tu, Y.; Lv, M.; Xiu, P.; Huynh, T.; Zhang, M.; Castelli, M.; Liu, Z.; Huang, Q.; Fan, C.; Fang, H.; Zhou, R. Destructive extraction of phospholipids from *Escherichia coli* membranes by graphene nanosheets. *Nat. Nanotechnol.* **2013**, 8, 594–601.

(29) Yin, J.; Zhu, G.; Deng, B. Graphene oxide (GO) enhanced polyamide (PA) thin-film nanocomposite (TFN) membrane for water purification. *Desalination* **2016**, 379, 93–101.

CHAPTER 6

Conclusions and Summary

Although the fields of research discussed within the chapters of this dissertation are wide-ranging, the central theme of surface modification and analysis highlights the important role that surface and interfacial science plays in materials chemistry. Each chapter covered how an important aspect of surface chemistry influenced the research:

- Chapter 2 investigated how a mixture of different solvents can relieve the interfacial energy between sheets of hexagonal boron nitride (h-BN), thereby making it easier to exfoliate the stacked sheets into single- or fewer-layered sheets of h-BN.
- Chapter 3 showed how the photothermal reduction of graphite oxide can lead to high-surface area graphene. This prevents the graphene sheets from restacking and allows for the fabrication of ultra-high power supercapacitors for energy storage.
- Chapter 4 discussed how the simple, scalable modification of reverse osmosis (RO) membrane surfaces with perfluorophenyl azide molecules can prevent initial bacterial adhesion, thus creating antifouling RO membranes that will last much longer than their conventional commercial counterparts.
- Chapter 5 looked at how anchoring graphene oxide onto polyamide RO membrane surfaces can render them more hydrophilic, smooth, and ultimately antimicrobial, with considerable resistance to protein fouling and biofouling.

The thoughtful researcher will be careful to consider not only a material's bulk properties, but as well its surface chemical and physical properties. In taking both the bulk and surface chemistries into account, materials with unique and curious properties can be synthesized and studied throughout a wide range of research areas.